Università degli Studi Roma Tre

Dipartimento di Matematica e Fisica
Doctoral program in Physics – XXXIV cycle

PH.D. THESIS

Study of devices based on Josephson junctions for galactic axion search

Author:
Alessio Rettaroli

Supervisor:
Dr. **Claudio Gatti**

Doctoral Program Coordinator:
Prof. **Giuseppe Degrassi**

November 2021

The most beautiful thing we can experience
is the mysterious.
It is the source of all true art and science.

– Albert Einstein

Through the door a harvest feast is lit by candlelight
It's the bottom of a staircase that spirals out of sight
The carpet crawlers heed their callers:
We've got to get in to get out

– Genesis

Abstract

The axion is a hypothetical particle that was first introduced by Weinberg and Wilczek as a consequence of the Peccei-Quinn mechanism to solve the strong CP problem of QCD. The axion is a pseudo-Goldstone boson associated with an additional symmetry of the Standard Model Lagrangian, which is spontaneously broken at an extremely high energy scale f_a. Axions, with mass $m_a \propto 1/f_a$, may constitute the dark matter content in our Galaxy.

Within the QUAX-aγ experiment, we demonstrate the advantage of exploiting a Josephson parametric amplifier, whose noise is at the standard quantum limit. A galactic axion search with mass $m_a \simeq 43$ μeV is carried out by putting an oxygen-free high conductivity copper resonant cavity inside an 8.1 T magnetic field, in an environment cooled to about 200 mK. The total noise temperature is about 1 K, with the contribution of 0.5 K coming from the Josephson parametric amplifier at the cavity resonance frequency of about 10.4 GHz. This allows us to reach the sensitivity necessary to the detection of QCD axions, setting an upper limit to the axion-photon coupling constant of $g_{a\gamma\gamma} < 0.766 \times 10^{-13}$ GeV^{-1} at the 90% confidence level.

At frequencies as high as 10 GHz, linear amplifiers become a limitation, even if quantum devices are involved. Reaching sensitivities necessary to the detection of QCD axions at high frequencies, therefore, requires the use of single-photon sensors. The detection of single microwave photons with good efficiency and low dark counts is a hard challenge, but Josephson systems are proved to be particularly suitable for this task. A simple strategy consists in the use of a current-biased Josephson junction as a switching detector.

Within the SIMP project, we are testing Al/AlO$_x$/Al Josephson junctions to implement this technology, and here several characterizations are presented. As a first step, we gain confidence with the simulation framework to optimize the design parameters of future single-photon detectors. Then, the first characterization of two junctions through escape rate measurements is carried out. Combining their results with simulations, we estimate an optimal working point for a Josephson junction-based photon counter, consisting in a current bias of $I_b = 0.65\, I_0$. In this bias condition, the dark count rate would be as low as 1 mHz, taking contributions only from macroscopic quantum tunneling.

Next, the characterization of a Josephson junction integrated in a single chip with a coplanar waveguide, constituting the simplest prototype of photon detector, is presented. The study is based on the switching behavior in the presence of microwaves. When the junction is stressed with continuous microwaves, switching events occur with only one or few photons, thanks to an enhancement mechanism which increases the probability of switching. When pulsed microwaves are applied, we observe that the number of photons required for the junction activation is approximately equal to the number of levels in its potential well, as expected from the simulations. In our experimental conditions, this number is few tens of photons.

Publication list

Some of the contents of this thesis may also be found in the following publications:

[1] **A. Rettaroli**, D. Alesini, D. Babusci, C. Barone, B. Buonomo, M. M. Beretta, G. Castellano, F. Chiarello, D. Di Gioacchino, G. Felici, G. Filatrella, L. G. Foggetta, A. Gallo, C. Gatti, C. Ligi, G. Maccarrone, F. Mattioli, S. Pagano, S. Tocci and G. Torrioli.

Josephson junctions as single microwave photon counters: simulation and characterization. (2021)

Instruments **5**(3), 25 (2021)

DOI: 10.3390/instruments5030025

[2] D. Alesini, C. Braggio, G. Carugno, N. Crescini, D. D'Agostino, D. Di Gioacchino, R. Di Vora, P. Falferi, U. Gambardella, C. Gatti, G. Iannone, C. Ligi, A. Lombardi, G. Maccarrone, A. Ortolan, R. Pengo, **A. Rettaroli**, G. Ruoso, L. Taffarello and S. Tocci.

Search for invisible axion dark matter of mass $m_a = 43$ *μeV with the QUAX–aγ experiment.*

Phys. Rev. D **103**, 102004 (2021)

DOI: 10.1103/PhysRevD.103.102004

[3] C. Guarcello, A. S. Piedjou Komnang, C. Barone, **A. Rettaroli**, C. Gatti, S. Pagano, G. Filatrella.

Josephson-based scheme for the detection of microwave photons.

Phys. Rev. Appl. **16**, 054015 (2021)

DOI: 10.1103/PhysRevApplied.16.054015

Acknowledgments

During these years since I was an undergraduate student, I did not take the opportunity to thank my family. This might be a good opportunity, so here we are. Thank you for your "nonintrusiveness": what I mean is that most of the times a student hears the usual questions like *what about that exam?* or *how many exams to finish?*, with the result of generating constant pressure. But you did not. Nonetheless, I always knew you are all proud of me, and this made me feel good.

Once again, thank you to my lab team: Claudio Gatti, Daniele Di Gioacchino, Carlo Ligi, Giovanni Maccarrone, Simone Tocci and Alessandro D'Elia. COLD lab has been my nest since my Master degree thesis, and like to a little bird at its first try you are teaching me how to fly. Also, thank you Simone and Alessandro for your empathy, I always appreciate.

I also want to mention all the people who provided useful material for the drafting of this thesis, and people who read all or part of the elaborate, so I double thank my lab mates and I add to the list Fabio Chiarello and Francesco Mattioli from IFN-CNR, and Sergio Pagano from the INFN group in Salerno.

Thank you to the occupants of the "Aquarium", my office mates at Roma Tre: Alessio Mattia, Chiara, Simone, Raul, Sacha. Thank you for the endless nonsense, for the memes and for the lunch discussions. I have known some of you for a long time, we used to be classmates and we're now approaching "the grown-up world", and seemingly our routes are dividing. I hope this is not the end of the story, we'll meet again and we'll have new adventures.

And here we come to the final acknowledgments. A special thank goes to all the people that make me laugh. Laughter is a medicine. But I guess that the most important acknowledgements are always left at the end, since they deserve a sort of a climax. So I thank my second family, although not second in importance. Alessandro, Alessio and Riccardo: we'll find the path guys. We'll find it together.

Contents

Introduction

The 21st century is the *new-physics*-century. Apparently, it seems that the more we discover, the less we know about our Universe. In fact, it is well known from the Planck satellite observations [4] that the matter we know accounts for only about 5% of the total amount of energy in the Universe. Or, reversing the point of view, this means we don't know 95% of the place we inhabit, with a decent precision. Actually, the situation is not so "dark" and fearful; two are the main veiled entities hiding to us, the dark matter and the dark energy. While the latter is still inaccessible, dark matter has left understandable traces. Although being elusive, invisible, it pervades the Universe and its gravitational interaction with ordinary matter has a clear effect on our galaxies and is essential for our existence. The efforts of modern science to disclose the dark matter nature will open the portal of a *new* era of particle physics.

Dark energy and dark matter are added to the successful but not yet ultimate Standard Model (SM) of particle physics within the framework of the ΛCDM model. The first letter, Λ, indicates the additional cosmological constant term in the Einstein's equation of general relativity to include the effect of dark energy, while CDM refers to the cold dark matter hypothesis, supported by cosmological observations on cosmic background radiation and simulations of large-scale structures of the Universe.

The connection between particle physics and the puzzle of dark matter, initially born as an astrophysical and cosmological one, shows when physics questions on *what is dark matter made of*. Theoreticians postulate Beyond the Standard Model (BSM) new particles to address the issues of the SM, so we are naturally granted with an enormous proliferation of candidates to study as dark matter. Among nonbaryonic candidates, there are new particles belonging to different categories, all well motivated. The most popular are sterile neutrinos, weakly interacting massive particles (WIMPs), including electroweak-scale or extra-dimensions BSM particles, and weakly interacting sub-eV particles (WISPs), arising as

Nambu-Goldstone bosons from any high-energy global symmetry-breaking theory. Axions and axion-like particles (ALPs) are part of the latter category.

The axion is worth-noting as it offers a non-*ad hoc* solution to the DM problem. In fact, its story began when it was originally introduced as a consequence of the postulated solution to the CP problem of the strong interactions, but since then, it immediately became an interesting DM candidate. Two major problems of modern physics would be solved in a single shot. Now, since an evidence of supersymmetries is missing in the high energy landscape, the axion is at the moment the best motivated candidate [5], it is arousing increasing interest and more and more resources are being invested on experiments to search for this new light boson.

The strong CP problem is born because the complete QCD Lagrangian allowed in the SM is CP-violating, but on the other hand observations show that strong interactions are CP-conserving. In terms of $\bar{\theta}$, the parameter responsible for the violation, experiments constrain it to be as small as 10^{-10} [6, 7], so that it seems to be a fine-tuning problem. Peccei and Quinn came with a solution in 1977 [8, 9], assuming the existence of an additional $U(1)$ global symmetry with characteristics such that, after its spontaneous breaking, the CP-violating phase $\bar{\theta}$ is driven dynamically to zero. Immediately after, in two back-to-back papers, Weinberg and Wilczek [10, 11] realized that associated to the breaking of this new symmetry there has to be a new scalar field, or in other words a new light pseudoscalar: the axion.

Few years later, in 1983 [12], Sikivie conceived the haloscope, a conceptually simple experimental apparatus to detect axions from the galactic halo thanks to their coupling to the electromagnetic field at microwave frequencies. The simplest haloscope is constituted by a microwave resonant cavity in a region of space where an external static magnetic field is applied to cause the conversion into photons (see Chap. 1). All the components, including the devices needed for the amplification process of the generated photons, are put in a cryogenic environment to better the signal-to-noise ratio (SNR). The main sources of noise are in fact coming from thermal excitations of electrons (Johnson noise). The efforts of research and development programs in the field are devoted to the continuous improvements of the haloscopes performance and sensitivity to be able to probe the axion existence in a region as large as possible of their parameter space. Two of the fundamental aspects in the fieldwork are the amplification and detection of the photons from the axion conversion.

Very low noise microwave sensors are a key technological pillar in this research line. Typical microwave detectors are based on linear amplifiers, that however have an irreducible noise level even at zero temperature, coming from quantum fluctuations of the vacuum. This quantum limit is now being reached by the most advanced detectors of this type (e.g. those based on SQUIDs or Josephson Parametric Amplifiers), and the truly frontier at this moment is defining strategies to overcome this limit. An alternative strategy with respect to linear amplifiers and quantum-limited sensors is to use single-photon detectors, that do not suffer from the quantum limit. We can rely on the technological advancements of the last two decades, since attention to single photon detection has grown due to the demanding application in quantum computing. Several techniques have been developed to detect single photons, such as Quantum Non-Demolition measurements [13–18], Switching Detectors [19–21], Hot Electron Detectors [22, 23] and Quantum Dot Detectors [24]. Belonging to Switching Detectors in the microwave range of radiation are Josephson junction-based photon counters [20] and transmon qubits [14, 25].

This thesis explores the possibility of using Josephson junctions as detectors of microwave radiation with the capability of counting single photons. Moreover, parametric amplifiers based on Josephson junctions have been used in the detection process when looking for axion dark matter.

The dissertation is structured as described in the following. In Chap. 1 I give the more concise overview as possible on axion concepts and state of the art experiments, while Chap. 2 is devoted to the fundamental equations governing the behavior of Josephson junctions. In Chap. 3 the last activities of the QUAX experiment are presented, where a JPA has been used in haloscope searches to reach the QCD axion sensitivity. Chap. 4 contains a description and functioning of the new haloscope at the National Laboratories of Frascati (LNF). To reach the sensitivity to DFSZ axions with the setup of the future LNF haloscope, a single photon counter is needed, therefore Chap. 5 and Chap. 6 are concerning, respectively, the dc and rf characterization of two Josephson junctions fabricated to get familiar with the simplest design of a single photon detector.

CHAPTER 1

Axions: theory and experiment

Axions are light pseudoscalar particles appearing as a consequence of the solution that Peccei and Quinn gave to explain the apparently unnatural absence of CP violation in quantum chromodynamics (QCD). This strong CP problem arises because a CP-violating phase $\bar{\theta}$ seems to be fine tuned to an embarrassing small number, where in principle it could take any value from 0 to 2π. In the Peccei-Quinn solution, the parameter $\bar{\theta}$ is promoted to a field which dynamically relaxes to zero after the spontaneous breaking of a new global $U(1)$ symmetry, with the consequent prediction of the existence of a new pseudo-Goldstone boson called axion.

Axions are well-motivated cold dark matter candidates, as they can be abundantly produced in the early stages of the Universe through nonthermal mechanisms. Axions can be mainly detected thanks to their coupling to the electromagnetic field, which allows the conversion into photons. Experiments are categorized depending on the axion sources: helioscopes search for axions coming from the Sun, haloscopes search for galactic axions and light-shining-through-walls experiments are pure laboratory searches.

All these aspects are treated in this Chapter. If the readers are not interested in the axion derivation given in Sec. 1.1, they can directly skip to Sec. 1.2 (axion properties) and Sec. 1.3 (axion detection).

1.1 The physics case

1.1.1 The $U(1)_A$ problem and the strong CP problem

The $U(1)_A$ problem arises when approximate symmetries are considered in QCD in the chiral limit, in which the quark masses are made to tend to zero, $m_q \approx 0$. This might seem a pure mental exercise, since we know that the quark masses are not zero and well measured [26], but it actually brings to predict wrong masses for the particles in the hadron spectrum, in particular the η' meson.

To see how axial and vector symmetries act on QCD, it is useful to write the QCD gauge-invariant Lagrangian density, that for one quark flavor is [27]

$$\mathscr{L}_{\mathrm{QCD}} = \bar{q}_L i\gamma^\mu D_\mu q_L + \bar{q}_R i\gamma^\mu D_\mu q_R - \bar{q}_L m\, q_R - \bar{q}_R m\, q_L - \frac{1}{4} G^a_{\mu\nu} G^{\mu\nu}_a, \tag{1.1}$$

with D_μ the covariant derivative, m the mass of the quark, q_L and q_R are left- and right-handed quark fields, and $G^{\mu\nu}_a$ the gluon field strength tensor:

$$G^{\mu\nu}_a = \partial^\mu A^\nu_a - \partial^\nu A^\mu_a + g_s f_{abc} A^\mu_b A^\nu_c, \tag{1.2}$$

A^μ_a is the gluon vector field, $a, b, c = 1, \ldots, 8$ are indexes for the gauge fields, f_{abc} are the structure constants of $SU(3)_\mathrm{c}$ (the sum over b and c is implicit), and g_s is the coupling constant of strong interactions.

The Standard Model is invariant under $SU(3)_c \times SU(2)_W \times U(1)_Y$ transformations, where the c, W and Y subscripts respectively stand for color, weak isospin and hypercharge. If the chiral limit is introduced in the game, the quark fields exhibit additional symmetries concerning also their flavors. In a 2-flavor model, the mass of the u and d quarks are supposed to be zero, which is a reasonable assumption since $m_u \simeq 2.16$ MeV and $m_d \simeq 4.67$ MeV [26] are small compared to $\Lambda_{\mathrm{QCD}} \approx 200$ MeV. In the chiral limit, the vector $SU(2)_V$ and $U(1)_V$ and the axial $SU(2)_A$ and $U(1)_A$ transformations become symmetries, since the mass terms in Eq. (1.1), which are the only mixing terms between left- and right-handed fields, are dropped to zero. Therefore, QCD acquires a new global $SU(2)_V \times SU(2)_A \times U(1)_V \times U(1)_A$ symmetry. When the masses are restored, these become approximate symmetries.

In a 3-flavor model, the chiral limit is obtained by considering also the s quark with null mass, which is an even more rough approximation than the 2-flavor model. In this case, the new approximate symmetry is $SU(3)_V \times SU(3)_A \times U(1)_V \times U(1)_A$, and must predict a hadron spectrum. Actually, $U(1)_V$ is always an exact symmetry and implies the baryon number conservation [28]. The $SU(3)_V$ symmetry predicts, as an example, triplets of particles degenerate in mass, which can be recognised with the Σ triplet in the observed hadron spectrum. The axial symmetries have to be spontaneously broken, because if they were exact, they would predict a barionic octet with odd parity, which is not observed. As a consequence of the Nambu-Goldstone theorem [29], nine bosons are expected by breaking the $SU(3)_A \times U(1)_A$, now called pseudo-Nambu-Goldstone bosons because they possess a mass. The candidates to be pseudo-Nambu-Goldstone bosons associated to $SU(3)_A$ are the pions (π^+, π^-, π^0), the kaons (K^+, K^-, K^0, $\overline{K}^0$) and the η meson, constituting a pseudoscalar octet, while the η' meson is the candidate boson associated to $U(1)_A$. And that's where this all falls apart. The η' mass is $m_{\eta'} \simeq 958$ MeV, even greater than the proton mass, so the elephant in the room cannot be ignored anymore. Steven Weinberg [30] pointed out that in the 3-flavor model the light pseudo-Nambu-Goldstone boson associated to the $U(1)_A$ broken symmetry should have a mass

$$m_L < \sqrt{3}m_\pi \approx 240\,\text{MeV}, \tag{1.3}$$

quite far from the observed η' mass. Thus, the $U(1)_A$ problem can be formulated with the question: why the η' meson is *so* heavy? In other words, why the real world is so different from the approximated one?

The answer is not so straightforward and involves chiral anomalies and fancy properties of the physics behind the QCD vacuum structure.

A symmetry of a Lagrangian in the classical field theory is said to be anomalous when it is violated in its quantum formulation, and this is exactly what happens when considering the axial current J_5^μ associated to the $U(1)_A$ transformation, even in the chiral limit. From the Noether's theorem we know that a symmetry implies a conservation law, with its associated current satisfying $\partial_\mu J^\mu = 0$. Due to anomalies in one-loop triangular diagrams, the four-divergence acquires an additional term, $\partial_\mu J_5^\mu \neq 0$ [27, 28], therefore the axial current is not conserved and $U(1)_A$ cannot be a symmetry, being explicitly broken. But this is not the whole story. In fact, it can be shown that the four-divergence is proportional to a total derivative, $\partial_\mu J_5^\mu \sim \partial_\mu K^\mu$ (see [31] for the K^μ expression). Then, a new axial current $\hat{J}_5^\mu$ can be defined, incorporating K^μ in J_5^μ, and this satisfies $\partial_\mu \hat{J}_5^\mu = 0$. This means that $\hat{J}_5^\mu$ is a conserved quantity, and as a consequence of the Noether's theorem this implies again a $U(1)$ global symmetry to exist, bringing the problem back to life.

If the problem is addressed from another point of view, it can be said that the effect of the chiral anomaly on the QCD Lagrangian is to add a term $\delta\mathscr{L} \propto \partial_\mu J_5^\mu \propto \partial_\mu K^\mu$ [32], which is a total derivative, as just said. In quantum field theory, if the Lagrangian variation $\delta\mathscr{L}$ is either zero or equal to a four-divergence, the action $S = \int \mathscr{L}\, \mathrm{d}^4x$ is left unchanged, without physical consequences. This seems a stroke of luck!

Nope.

The surface integral of K^μ can be discarded only if the usual hypothesis that the fields are null at spatial infinity is true. And here comes the turning point: this is not true for the gauge fields of QCD appearing in K^μ, which do not all tend to zero simultaneously at infinity, and the surface integral of K^μ does not cancel. The reason stays in the nontrivial topology of the QCD vacuum structure, discovered by 't Hooft [33, 34]. In a very few words, different equivalent configurations of the QCD vacuum exist, and they cannot be reached by infinitesimal gauge transformations starting from identity, implying the presence of an energy barrier between them. However, quantum tunneling between vacua is possible.

As a consequence of the nonvanishing surface integral of K^μ at infinity, the QCD Lagrangian finally takes the additional term

$$\mathscr{L}_\theta = \frac{g_s^2}{32\pi^2}\theta_{QCD}\,\mathrm{Tr}\left(G_{\mu\nu}\tilde{G}^{\mu\nu}\right), \tag{1.4}$$

where θ_{QCD} is a superposition of all the vacuum configurations, the so-called θ-vacuum, which is invariant under gauge transformations. The trace has been defined as

$$\mathrm{Tr}\left(G^{\mu\nu}\tilde{G}^{\mu\nu}\right) = \mathrm{Tr}\left(\lambda_a G_a^{\mu\nu}\lambda_b \tilde{G}^b_{\mu\nu}\right) = \frac{1}{2}G_a^{\mu\nu}\tilde{G}^a_{\mu\nu}, \tag{1.5}$$

where $\lambda_{a,b}$ are the generators of the $SU(3)_c$ group; a, $b = 1, \ldots, 8$, and the sum over a and b is implicit. $\tilde{G}$ is the dual tensor of G:

$$\tilde{G}^{\mu\nu} = \frac{1}{2}\varepsilon^{\mu\nu\rho\sigma}G_{\rho\sigma}, \tag{1.6}$$

and $\varepsilon^{\mu\nu\rho\sigma}$ is the Levi-Civita antisymmetric tensor[1].

The $U(1)_A$ problem is solved in the sense that $U(1)_A$ is *never* a symmetry, neither exact nor approximate, because of the lack of gauge invariance in the QCD vacuum [31]. As a result, the θ-term (1.4) is included in the Lagrangian.

Strong CP problem

The Lagrangian term of equation (1.4) is still Lorentz- and gauge-invariant, but due to the presence of $\varepsilon^{\mu\nu\rho\sigma}$ in the trace, it violates parity and time reversal; hence, as a consequence of the CPT theorem, it also violates the CP symmetry. Before going to the observable effects caused by such a term, I briefly discuss what is the other source of CP violation in the QCD.

Actually, if θ_{QCD} were the only contribution to CP violation, it could be ruled out by an axial transformation. In fact, thanks to the chiral anomaly, an axial transformation applied to $\mathscr{L}_\theta$ causes the phase to shift as

$$\theta_{QCD} \longrightarrow \theta_{QCD} + 2N_f\alpha, \tag{1.7}$$

where N_f is the number of quark flavors to be included and α is the $U(1)_A$ transformation parameter. Then, one could make $\theta_{QCD} = 0$ by a suitable choise of α.

However, when considering the electroweak sector, another θ-term appears. After the

[1] The convention $\varepsilon^{0123} = +1$ is assumed.

electroweak spontaneous symmetry breaking through the Higgs mechanism, the quark mass terms contain the quark fields in the basis in which they are eigenstates of the electroweak interactions, and their mass matrices are neither Hermitian nor diagonal. They can be made real and diagonal matrices by performing unitary transformations on the quark fields, and these also require $U(1)_A$ rotations. The chiral anomaly in $U(1)_A$, again, brings a further term in the QCD Lagrangian, of the same type as Eq. (1.4). Therefore, the total θ-term becomes

$$\overline{\theta} \equiv \theta_{QCD} - \theta_{EW} = \theta_{QCD} - \arg\left(\det M_q\right), \tag{1.8}$$

where the second equality can be seen in [27, 31]. $\det M_q$ is the determinant of the quarks mass matrix M_q. Finally, the CP-violating Lagrangian which has physical observable effects is the one including the θ-term:

$$\mathscr{L}_{\not{CP}} = \mathscr{L}_{QCD} + \frac{g_s^2}{32\pi^2}\overline{\theta}\,\mathrm{Tr}\left(G_{\mu\nu}\tilde{G}^{\mu\nu}\right). \tag{1.9}$$

The strong CP problem resides in the not observed predictions that a θ-term implies, among which the most striking is the neutron electric dipole moment (EDM).

The neutron electric dipole moment

Due to the additional term in the QCD Lagrangian, the neutron should possess an EDM proportional to $\overline{\theta}$ [35]:

$$d_n \simeq e \cdot \overline{\theta}\frac{m_u m_d}{f_\pi^2(m_u + m_d)}\left(\frac{0.9}{4\pi^2}\ln\frac{\Lambda}{m_\pi}\right) \simeq 2.4 \cdot 10^{-16}\,\overline{\theta}\ e\,\mathrm{cm}, \tag{1.10}$$

where e is the electric charge of the electron, $f_\pi = 93\,\mathrm{MeV}$ the pion decay constant, m_u, m_d the up quark and down quark masses, respectively, and Λ is a constant of order the neutron mass m_n. (Natural units $\hbar = c = 1$ are used here, so that $1\,\mathrm{eV} \approx 1\,\mu\mathrm{m}^{-1}$). The neutron EDM has been measured with high accuracy and is compatible with zero. The most recent experiment on neutron EDM [7] reports a limit of

$$|d_n| < 3 \times 10^{-26}\,e\,\mathrm{cm} \quad (90\%\ \mathrm{CL}), \tag{1.11}$$

then giving an estimation of the upper limit that can be put on $\bar{\theta}$ (from Eq. (1.10)):

$$|\bar{\theta}| \lesssim 10^{-10}. \tag{1.12}$$

This looks very much like a fine tuning problem, since there is apparently no reason why θ_{QCD} and θ_{EW} should tune to zero at this level. In fact, any value from 0 to 2π is equally likely, as they come from two independent physics sectors. The strong CP problem can then be stated as: *why $\bar{\theta}$ is so small?*

1.1.2 The Peccei-Quinn mechanism

The solution was proposed by Peccei and Quinn in two papers in 1977 [8, 9]. They suggested to introduce a further exact axial global $U(1)$ symmetry, now called $U(1)_{PQ}$ symmetry, under which the full Standard Model Lagrangian is invariant. The key argument is that if it is spontaneously broken and has a chiral anomaly, as it should, there is an additional $G_{\mu\nu}\tilde{G}^{\mu\nu}$ term in the Lagrangian driving $\bar{\theta}$ dynamically to zero. Then, in 1978, Weinberg [10] and Wilczek [11] realized that the spontaneous breaking of the $U(1)_{PQ}$ symmetry requires a new pseudo-Nambu-Goldstone boson, the axion.

The derivation starts from the Yukawa couplings between the quarks and a new scalar complex field σ, of the type $\sim (\bar{q}_L \sigma q_R + \bar{q}_R \sigma^* q_L)$. Applying an axial transformation to the quarks, they rotate as $q_L \to e^{-i\alpha} q_L$ and $q_R \to e^{i\alpha} q_R$; then, for the Lagrangian to be invariant under these rotations, it is required that σ changes as $\sigma \to e^{-2i\alpha}\sigma$. The quark masses are then generated by the spontaneous symmetry breaking, writing σ as an expansion around its minimum:

$$\sigma(x) = (\rho(x) + f_a)\, e^{ia(x)/f_a}, \tag{1.13}$$

where f_a is the scale associated to the symmetry breaking and $\rho(x)$ and $a(x)$ are real fields, with the former playing the role of the Higgs boson in the minimal formulation of the Standard Model, while $a(x)$ is the axion field, i.e. the $U(1)_{PQ}$ Nambu-Goldstone boson. Under a $U(1)_{PQ}$ phase transformation, the axion field rotates as $a(x) \to a(x) + \alpha\, f_a$ (Eq. (1.13)). The form of the effective Lagrangian is fixed by requiring that the axion has a coupling to $G_{\mu\nu}\tilde{G}^{\mu\nu}$, to guarantee the right chiral anomaly in the current J^{μ}_{PQ} [31]:

$$\mathscr{L}_{\text{eff}} = \mathscr{L}_{\text{SM}} + \frac{\alpha_s}{8\pi}\bar{\theta}\, G^b_{\mu\nu}\tilde{G}^{\mu\nu}_b - \frac{1}{2}\partial_\mu a \partial^\mu a + \mathscr{L}_{\text{int}}\,(\partial^\mu a, q) + \xi \frac{\alpha_s}{8\pi}\frac{a}{f_a} G^b_{\mu\nu}\tilde{G}^{\mu\nu}_b . \tag{1.14}$$

Here, $\mathscr{L}_{\text{int}}$ contains the axion derivative couplings, $\alpha_s \equiv g_s^2/4\pi$, and ξ is a model-dependent parameter associated to the $U(1)_{PQ}$ current anomaly.

The last term of Eq. (1.14) solves the strong CP problem and gives a mass to the axion. In fact, it provides an effective potential for $a(x)$, and Peccei and Quinn [8, 9] showed that when imposing the minimum of the potential, the axion vev is forced to be

$$\langle a \rangle = -\bar{\theta} f_a/\xi\, . \tag{1.15}$$

The axion can thus be thought of as the dynamical version of the $\bar{\theta}$, and the strong CP problem is solved if $\mathscr{L}_{\text{eff}}$ is expressed in terms of the physical axion field $a_{\text{phys}} = a - \langle a \rangle$, which has a null vev. Moreover, if the potential for the scalar field σ is taken into account and imagined as a wine-bottle-shaped potential, when the symmetry breakdown occurs it tilts towards a direction, and the oscillations of the $a(x)$ degree of freedom around the new minimum give it a mass, that can be calculated from its effective potential as $m_a^2 = \langle \partial^2 V_{\text{eff}} / \partial a^2 \rangle_{\langle a \rangle}$.

The effective Lagrangian can be rewritten including also the mass term as [31]

$$\mathscr{L}_{\text{eff}} = \mathscr{L}_{\text{SM}} - \frac{1}{2}\partial_\mu a_{\text{phys}} \partial^\mu a_{\text{phys}} - \frac{1}{2} m_a^2 a_{\text{phys}}^2 + \mathscr{L}_{\text{int}} \left(\partial^\mu a_{\text{phys}}, q\right) + \frac{\alpha_s}{8\pi} \frac{a_{\text{phys}}}{f_a} G^b_{\mu\nu} \tilde{G}^{\mu\nu}_b, \qquad (1.16)$$

where now the term $\mathscr{L}_{agg} \sim a_{\text{phys}}\, G^b_{\mu\nu} \tilde{G}^{\mu\nu}_b$ represents the interaction of axions with gluons, from which all the other interactions useful for their detection can be derived (see Sec. 1.3). $\mathscr{L}_{\text{eff}}$ does not contain dangerous CP-violating terms anymore, because when observable quantities depending on a_{phys}, as the neutron EDM, are considered over a long time interval, they average to zero and the CP violation is not seen[2].

Now that the simple picture has been outlined, by changing how the $U(1)_{PQ}$ symmetry is added to the SM Lagrangian a variety of axion models is obtained. Below you can find a brief discussion of the PQWW model for historical reasons and the KSVZ and DFSZ invisible axion models.

The PQWW model

In the framework of the minimal SM all the fermions acquire a mass thanks to the coupling with the Higgs doublet Φ. When all quark flavors are included in the PQ mechanism, the σ field cannot simply be identified with the Higgs doublet. In fact, in the Higgs model, the down-type quarks couple to Φ in the Yukawa Lagrangian, while up-type quarks couple to $\tilde{\Phi} = i\sigma_2 \Phi^*$, that does not transform in the same way as Φ does under $U(1)_{PQ}$ transformations, which is necessary to make the Lagrangian $U(1)_{PQ}$-invariant. Peccei and Quinn thought of a nonminimal model in which there are two Higgs doublets, Φ_1 and Φ_2, having the right transformations to preserve the $U(1)_{PQ}$ invariance [31]. f_a is a free parameter of the theory, and in the PQWW model it is assumed to be equal to v, the energy scale of electroweak interactions: $f_a = \sqrt{v_1^2 + v_2^2} \equiv v \simeq 246$ GeV, where v_1 and v_2 are the minima of the potentials for Φ_1 and Φ_2.

In this model, ξ has the value $\xi = N_g(x + 1/x)$, where N_g is the number of fermion generations and $x = v_2/v_1$. The axion mass and couplings are calculated with effective Lagrangian techniques [31], where mixing terms with the neutral pion and the η meson arise. These mixings also allow the axion to have interactions with two photons, which are exploited to design axion detectors (Sec. 1.3). The mass and the coupling to photons result in

$$m_a = \frac{m_{\pi^0} f_\pi}{v} \frac{\sqrt{m_u m_d}}{(m_u + m_d)} \simeq 24\,\text{keV}, \qquad (1.17)$$

[2] Note that the CASPEr experiment is trying to detect just the time-varying neutron EDM resulting from the axion-neutron interaction [36].

$$\mathscr{L}_{a\gamma\gamma} = g_\gamma \frac{\alpha_{\rm em}}{4\pi} \frac{a}{f_a} F_{\mu\nu} \tilde{F}^{\mu\nu}, \tag{1.18}$$

with $g_\gamma = \xi m_u/(m_u + m_d)$, $\alpha_{\rm em} = e^2/4\pi$ is the fine structure constant of QED in natural units and $F_{\mu\nu}$ is the electromagnetic field strength tensor.

The PQWW model, however, has been ruled out by experiment. In fact, the predicted branching ratio of the decay $K^+ \to (\pi^+ + a)$ [37] has been excluded by the measured branching ratio of the process $K^+ \to (\pi^+ + \text{nothing})$ [38]. Evidences of this type brought to think that theories in which $f_a \gg v$ are more reliable, and since the axion mass and the coupling constants are inversely proportional to f_a, this leads to theories with light axions very weakly coupled to SM particles. These are called *invisible* axion models.

Invisible axion models

The two most cited models of invisible axions are the KSVZ model, from Kim [39] and Shifman, Vainshtein, Zakharov [40] and the DFSZ model, due to Zhitnitsky [41] and Dine, Fischler, Srednicki [42]. In the KSVZ model, only a complex scalar field σ and a single heavy quark are added to the SM, with the energy breaking scale $f_a \gg v$. The quark is extremely massive because it acquires a mass $M_Q \propto f_a$. The axion appears in the phase of the σ field, and its mass has the same form as in the PQWW model, but with f_a instead of v:

$$m_a = \frac{m_{\pi^0} f_\pi}{f_a} \frac{\sqrt{m_u m_d}}{(m_u + m_d)}. \tag{1.19}$$

Both the new quark and the scalar field are $SU(2)_W \times U(1)_Y$ scalars, and all the SM particles are $U(1)_{PQ}$ scalars, so the axion has not interactions with leptons.

The DFSZ model is an extension of the PQWW one. Here, besides the Higgs doublets Φ_1 and Φ_2, also a complex scalar field σ is added. As in the PQWW model, all quarks and leptons possess PQ charges, and σ is an $SU(2)_W \times U(1)_Y$ scalar. The axion mass has the same expression as in eq. (1.19), but in the DFSZ model the energy scale parameter f_a is rescaled to $\tilde{f}_a = f_a/2N_g$, and is $\tilde{f}_a = \langle \sigma \rangle$. In both models, though, the couplings are different from the PQWW case, since g_γ and ξ are model-dependent.

1.2 Axion properties

Now that the axion has been introduced as a pseudo-Nambu-Goldstone boson in a natural extension of the Standard Model, the remaining sections are dedicated to the definition of its properties and how they determine possible detection scenarios. They are going to be the properties of a light pseudoscalar boson electrically neutral and very weakly coupled to Standard Model particles.

In the models described in Sec. 1.1.2, essentially the only free parameter encountered for the axion is f_a, the energy scale of the PQ transition. Then, model-dependent parameters are defined as a function of f_a, including the axion mass m_a. Its expression has been already given in Eq. (1.17):

$$m_a = \frac{m_{\pi^0} f_\pi}{f_a} \frac{\sqrt{m_u m_d}}{(m_u + m_d)} \simeq 5.86\ \mu\text{eV} \times \left(\frac{10^{12}\ \text{GeV}}{f_a} \right). \tag{1.20}$$

Although its value depends on the assumption made on f_a by the specific model, the form of eq. (1.20) is model-independent.

The axion-photon Lagrangian explaining the axion coupling to two photons has been introduced in Eq. (1.18):

$$\mathscr{L}_{a\gamma\gamma} = g_\gamma \frac{\alpha_{\text{em}}}{4\pi} \frac{a}{f_a} F_{\mu\nu} \tilde{F}^{\mu\nu} = \frac{1}{4} g_{a\gamma\gamma} a F_{\mu\nu} \tilde{F}^{\mu\nu}. \tag{1.21}$$

Here, in the second equality, the dimensionful coupling constant $g_{a\gamma\gamma}$ is introduced, which is defined as

$$g_{a\gamma\gamma} = \frac{\alpha_{\text{em}}}{\pi} \frac{g_\gamma}{f_a}. \tag{1.22}$$

It is usually reported with dimension in GeV^{-1} and is model-dependent. Being $g_{a\gamma\gamma}$ inversely proportional to f_a, it gives rise to very small electromagnetic couplings. When expressed in terms of the electric and magnetic fields (components of the $F_{\mu\nu}$ tensor), the Lagrangian (1.21) becomes

$$\mathscr{L}_{a\gamma\gamma} = -g_{a\gamma\gamma} a\, \boldsymbol{E} \cdot \boldsymbol{B}\,. \tag{1.23}$$

A nice derivation can be found in Appendix A of [43]. This expression is particularly useful when dealing with the axion conversion into photons in detectors, such as microwave cavities (Sec. 1.3).

Equation (1.23) has exactly the same form as the Primakoff process [44], which accounts for the π^0 production through a two-photon interaction. The inverse process, i.e. the π^0 decay into two photons, is called inverse Primakoff effect. The Primakoff processes can happen through a triangle diagram with a virtual fermion in the loop and are valid for any pseudoscalar meson decaying into two photons. Therefore, the axion is subject to the same interaction, since it inherits the electromagnetic interactions from the mixing with the pion and the η meson. The two diagrams representing the direct and inverse Primakoff processes are drawn in Fig. 1.1. While in the pion case the decay takes a contribution only from the chiral anomaly with QED, the axion diagrams receive contributions from both chiral anomalies with QED and with QCD.

Although axions can also have interactions with matter fields, the Primakoff effect is the main process in experimental searches for axions, since it provides both a production mechanism and a detection technique. The Primakoff effect of Fig. 1.1(right) is responsible for an

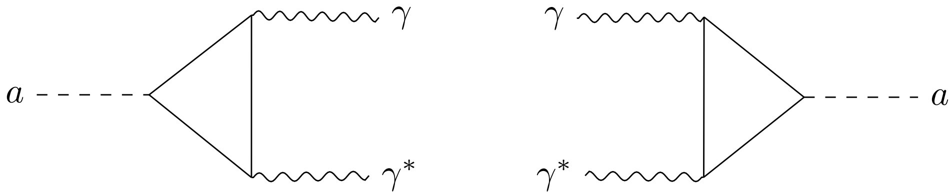

Figure 1.1: *Left*) Axion decay into one real photon and one virtual photon via the inverse Primakoff effect through a fermion loop. *Right*) Axion production via the Primakoff effect in vacuum, from one real and one virtual photon.

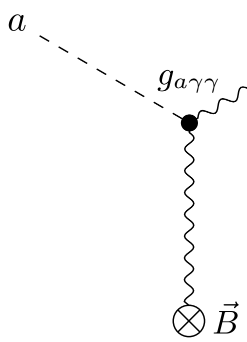

Figure 1.2: Conversion of an axion into a photon through the inverse Primakoff effect. The conversion is stimulated by a static magnetic field.

axion flux from stars, since in their cores many photons are produced via nuclear fusions. As we will see in Section 1.2.1, axion fluxes from stars can be used to obtain bounds on the $g_{a\gamma\gamma}$ coupling. On the contrary, the inverse Primakoff effect of Fig. 1.1(left) is the paradigm of axion detection. This can be exploited if in the diagram one real outgoing photon is substituted with an external static magnetic field, which continuously provides virtual photons and is treated as a classical electromagnetic field. This situation is depicted in Fig. 1.2. Also, if in the latter diagram the ingoing axion line and the outgoing photon line are exchanged, this would account for a production mechanism in some regions of the Universe where high magnetic fields are reached, such as pulsar magnetospheres or AGNs.

Coming to the interaction between axions and fermions, from Eq. (1.16) we saw that it must be a derivative coupling. A derivation is given in [45], but the following is written with the same notation as in [5]:

$$\mathscr{L}_{aff} = \frac{\partial_\mu a}{2f_a} \sum_f C_{aff} \left(\overline{\Psi}_f \gamma^\mu \gamma_5 \Psi_f \right), \tag{1.24}$$

where Ψ_f are fermion Dirac fields and C_{aff} are model-dependent dimensionless coupling constants. The interaction can be equivalently written as an effective CP-conserving La-

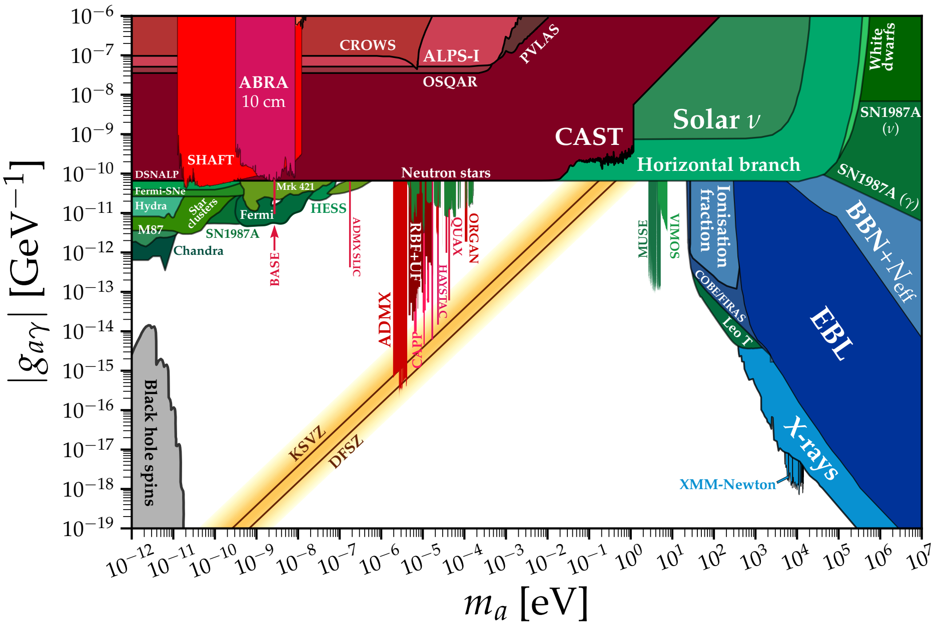

Figure 1.3: Parameter space ($g_{a\gamma\gamma}$ vs. m_a), with exclusion plots by experiments (red), astrophysical bounds (green) and cosmological bounds (blue). In yellow the QCD model band is shown, with the KSVZ and the DFSZ models marked. Source: https://cajohare.github.io/AxionLimits/ [46]. Similar plots exist for other axion couplings (see [5]).

grangian term:

$$\mathscr{L}_{aff} = -i\, g_{aff}\, a\, \left(\overline{\Psi}_f \gamma_5 \Psi_f\right), \tag{1.25}$$

having defined the dimensionless coupling constant g_{aff} as

$$g_{aff} \equiv \frac{C_{aff}\, m_f}{f_a}, \tag{1.26}$$

with m_f the mass of the fermion entering the interaction. The expression for the axion-fermion coupling is useful to discuss astrophysical bounds (Sec. 1.2.1) and the axion search with the QUAX-ae experiment (Chap. 3).

1.2.1 Axion parameter space

From the definition of the axion mass (1.20) and the axion coupling to photons (1.22), we see that both are inversely proportional to the scale constant f_a, therefore being $g_{a\gamma\gamma} \propto m_a$. The axion predicted from the models since now discussed, for which this proportionality relationship holds, is referred to as "QCD axion". The parameter space of the axion-photon coupling is the ($g_{a\gamma\gamma}$ vs. m_a) plane shown in Fig. 1.3. The plot shows the predicted **model band** in yellow and several bounds on the $g_{a\gamma\gamma}$ constant: in red dedicated axion experiments are shown, including haloscopes, helioscopes and light-shining-through-walls experiments;

the green areas indicate bounds from astrophysical observations; and blue refers to limits put by cosmology.

To understand why the yellow model band–which accounts for QCD axion models such as the KSVZ and DFSZ models–is indeed a band, the mass can be written as the following:

$$m_a = \frac{m_{\pi^0} f_\pi}{f_a} \frac{\sqrt{z}}{1+z}, \tag{1.27}$$

where $z = m_u/m_d$ is the light quarks mass ratio. From [26], its central value is $z = 0.47$, but it can take any value in the interval $0.40 < z < 0.53$, resulting in a range of possible values for the mass. Moreover, $g_{a\gamma\gamma}$ depends on the values that g_γ can take. In general, the dimensionless coupling g_γ for the invisible axion models has the form [47]:

$$g_\gamma = \frac{1}{2}\left(\frac{E}{N} - \frac{2}{3}\frac{4+z}{1+z}\right), \tag{1.28}$$

where E and N are, respectively, the electromagnetic and color anomaly coefficients. For instance, $E \neq 0$ when the theory possesses at least one quark charged under both $U(1)_{PQ}$ and $U(1)_{EM}$, so that it can have an axion-quark vertex and a quark-photon vertex, necessary to the diagrams of Fig. 1.1 to exist. For the KSVZ model the new quark does not possess $U(1)_{EM}$ charge, therefore $E = 0$.

For a fixed value of z, there will be different straight lines in the plot, corresponding to different models having distinct values of the ratio E/N. In Fig. 1.3 two lines are shown: one for the KSVZ model, for which $E/N = 0$, and one for the DFSZ model, having $E/N = 8/3$. However, the ratio E/N is not known *a priori*, and this allows to define a band of values for $g_{a\gamma\gamma}$ as a function of the mass m_a.

The region below the model band in the parameter space accounts for other QCD axion models [48], while all the other regions account for Axion-like Particles (ALPs). These are a generalization of the QCD axion, pseudo-Nambu-Goldstone bosons originating outside the Peccei-Quinn solution. The ALPs share the axion phenomenology, but since their coupling constant $g_{A\gamma\gamma}$ is not necessarily proportional to their mass, they cover an extremely wide range of couplings and masses.

Astrophysical and cosmological bounds

Constraints on axion (or more generally ALPs) mass and couplings are obtained from astrophysical and cosmological observations. In fact, if axions exist, they could be produced in astrophysical objects and affect their evolution. The production mechanisms mainly rely on the Primakoff effect: in a star, axions can be generated in their core if a photon interacts with the Coulomb field of the plasma, $\gamma + Ze \to Ze + a$. Then, since axions are expected to interact very weakly with SM particles, they can escape the core and then the surface, providing a nonstandard energy loss mechanism for stars. If the data from measurements on stellar evolution match the predicted rate of standard energy loss, a stringent bound on the axion coupling $g_{a\gamma\gamma}$ can be extracted. In the following, the main bounds present in Fig. 1.3 are briefly described. The informations are grasped from [5], [26] and [49] (for details on data and constraints see references therein).

- **Sun**: Due to the Primakoff effect, axions can be produced in the core and emitted as a flux, whose luminosity L_a is proportional to $g^2_{a\gamma\gamma}$ and the Sun luminosity $L_\odot$. From observations of solar luminosity, neutrino solar flux and helioseismology, it turns out that $L_a \lesssim 0.1 L_\odot$, giving the constraint of $|g_{a\gamma\gamma}| \lesssim 4.1 \cdot 10^{-10}$ GeV^{-1}. The attempt of direct detection of solar axions is discussed in Sec 1.3.

- **Globular Clusters**: Stars in the "horizontal branch" (HB) of a Globular Cluster colour-magnitude diagram have the same age, so their different stage of evolution is due to their mass. If they are in the HB branch, they have entered the helium-burning phase; axions or ALPs production would shorten the time spent in the HB branch. Comparing the number count of HB stars with the number count of "red giant branch" stars places an upper bound on $g_{a\gamma\gamma}$ (and then f_a and m_a).

- **Supernovae**: if axions and ALPs are produced in supernovae cores via the Primakoff process, they could then reconvert into γ-rays in the intergalactic magnetic field or in the Milky Way magnetic field. The lack of a γ-ray peak in correspondence with the neutrino pulse from the 1987 supernova in the Large Magellanic Cloud (SN1987A) allows to constraint $|g_{a\gamma\gamma}| \lesssim 5.3 \times 10^{-12}$ GeV^{-1} for masses $m_a \lesssim 4.4 \times 10^{-10}$ eV. Additionally, the existence of ALPs would affect the neutrino burst measured on Earth, but this puts a bound on the axion coupling to protons.

- **Cosmology**: In the early Universe, CMB photons could produce axions if they interact with intergalactic magnetic fields or with electric fields in the intracluster plasma. On the other hand, axions could decay before recombination. All these effects would cause a spectral distortion to the CMB. Another possibility is given by the redshift-broadened peak of photons from axion decay, generating a diffuse extragalactic background light, which is not observed from microwaves to γ-rays. Or axions can decay to photons up to x-ray energies, but these are constrained by the sensitive x-ray telescopes as Chandra, XMM-Newton etc.

There are also other axion production processes, of which I won't talk, that allow to put constraints on the couplings g_{aee} and g_{aNN}, like the nucleon bremsstrahlung $N + N \to N + N + a$ (a typical ALP production in neutron stars and Supernovae) and the electron bremsstrahlung.

The experimental upper limits in Fig. 1.3 will be discussed in Sec. 1.3.

1.2.2 Axion cosmology

As we said before, axions are also good candidates of cold dark matter. To account for CDM, they must satisfy some conditions, namely: axions have to be neutral, have very small couplings with ordinary matter, be stable within the Universe lifetime, be nonrelativistic and have the right relic density. The nature of a pseudo-Nambu-Goldstone boson makes the first two conditions already true, being the axion a real scalar field and having couplings inversely proportional to a high energy scale f_a. The other conditions are verified when the Peccei-Quinn mechanism is considered as a cosmological process, called *misalignment mechanism* or *vacuum realignment mechanism*, discussed here.

The axion field is generated during the PQ phase transition, in which the $U(1)_{PQ}$ symmetry gets spontaneously broken. This happens at a high temperature, $T \sim f_a \gg \Lambda_{QCD}$, when the QCD has not yet condensed, so that the axion is massless. Then, when the temperature of the Universe cools down to $T \sim \Lambda_{QCD}$, quark condensates form and the axion acquires a mass. This QCD phase transition corresponds to a tilt in the potential.

The evolution of the axion field in an expanding Universe is [50]

$$\left(\partial_t^2 + 3\frac{\dot{\mathcal{R}}}{\mathcal{R}}\partial_t - \frac{1}{\mathcal{R}^2}\nabla_x^2\right) a(x) + m_a^2(t) f_a \sin\left(\frac{a(x)}{f_a}\right) = 0\,, \tag{1.29}$$

where $\mathcal{R}(t)$ is the Universe scale factor of the Friedmann-Robertson-Walker metric and $\dot{\mathcal{R}}/\mathcal{R}$ is the Hubble parameter $H(t)$. The sinusoidal term in the equation comes from the derivative of the periodic axion potential. The axion evolution with time is shown in Fig. 1.4. When the mass is suppressed at high temperatures, $H(t) \gg m_a(t)$, it can be neglected and the solution to Eq. (1.29) is a constant, homogeneous field a_i. Since $a_i = \theta_i f_a$, this corresponds to a random θ_i value in the interval $[-\pi, \pi]$, and it is called initial misalignment angle. Two scenarios can occur: the *pre-inflation* scenario and the *post-inflation* scenario. In the former, the PQ phase transition happens before or during the inflationary era, so that all the regions of the Universe are causally connected after inflation and θ_i is unique. In the second case, the $U(1)_{PQ}$ symmetry gets broken after inflation, and many causally disconnected regions exist, giving rise to different θ_i values. However, if it is assumed that many patches exist, a unique mediated angle can be considered, being $\langle\theta_i^2\rangle = \pi^2/3$ [5].

Then, in the axion evolution, there is a critical time t_1 for which $m_a(t_1)t_1 = 1$. The axion field starts oscillating and the mass effectively turns on. This time is indicated as a dashed line in Fig. 1.4. Finally, when $H(t) \ll m_a(t)$, the amplitude slowly decays and the oscillations are almost sinusoidal, and this corresponds to the moment when the QCD color anomaly becomes effective and the $U(1)_{PQ}$ symmetry is also explicitly broken.

The zero-momentum solution of Eq. (1.29) describes coherent axions produced at rest, with energy density $\varrho_a = (1/2)m_a^2\mathcal{A}^2$ and number density $n_a = (1/2)m_a\mathcal{A}^2$, where $\mathcal{A}$ is the axion field amplitude. It turns out that the energy density has a dependence $\varrho_a \propto \mathcal{R}(t)^{-3}$ [50],

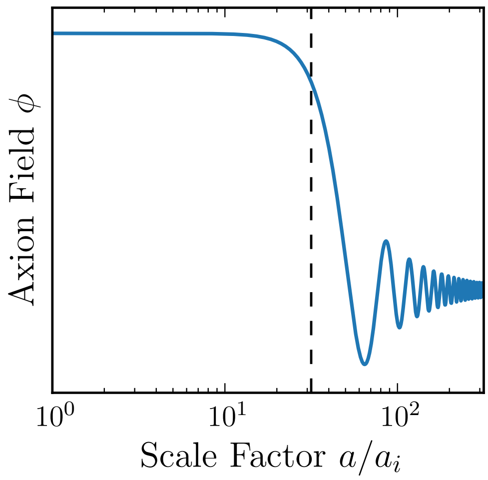

Figure 1.4: Evolution of the axion field with the scale factor of the Universe. The dashed line indicates the time t_1 at which the axion starts oscillating and its mass turns on. Taken from [51]. The notation here is different from the text: the axion field is expressed as ϕ (y-axis) and the scale factor as a (x-axis).

even in the nonzero-momentum solutions of the post-inflation scenario. This means that the number of axions in a comoving volume is conserved while the Universe expands and that dependence on $\mathcal{R}(t)$ is typical of nonrelativistic fluids. This means that axions are produced by a nonthermal mechanism and behave as nonrelativistic matter.

At this point the normalized relic energy density $\Omega_a = \varrho_a/\varrho_c$ can be estimated, where $\varrho_c = 3H_0^2/(8\pi G)$ is the critical density of the Universe, with H_0 the Hubble constant today and G the gravitational constant. In the pre-inflation scenario Ω_a takes only the contribution from the zero-momentum mode of the axion field, while in the post-inflation scenario contributions come also from nonzero-momentum modes and topological defects, like string decays and domain walls decays [5, 50]. In the two cases Ω_a is [50]

$$\begin{aligned} \Omega_a &\sim 0.15 \left(\frac{f_a}{10^{12}\,\mathrm{GeV}}\right)^{7/6} \left(\frac{0.7}{h}\right)^2 \theta_i^2 \qquad \text{pre-inflation} \\ &\sim 0.7 \left(\frac{f_a}{10^{12}\,\mathrm{GeV}}\right)^{7/6} \left(\frac{0.7}{h}\right)^2 \qquad \text{post-inflation,} \end{aligned} \tag{1.30}$$

where h is defined by $H_0 = h \times 100\,\mathrm{km\,s^{-1}\,Mpc^{-1}}$. Remarkably, when imposing that the predicted relic density do not exceed the measured dark matter energy density, an "overclosure" bound is put on f_a and m_a. The axion energy density must satisfy the observational constraint on the DM density of $\Omega_{DM}h^2 \simeq 0.12$ [4]. When turned into the condition $\Omega_a h^2 \lesssim 0.12$, it gives a lower bound to the mass and an upper bound to the energy scale:

$$\begin{aligned} m_a &\gtrsim 10^{-6}\,\text{eV}\,, \\ f_a &\lesssim 10^{12}\,\text{GeV}\,. \end{aligned} \tag{1.31}$$

Putting together astrophysical bounds and axion cosmology arguments, the preferred axion mass window is approximately

$$m_a \in (10^{-6} \div 10^{-3})\,\text{eV}. \tag{1.32}$$

However, lower mass values are still viable if the assumption that $\theta_i \sim \mathcal{O}(1)$ is dropped in favor of small θ_i values; these ranges fall in the so-called *anthropic axion window* [5].

Finally, the lifetime of an axion decaying into two photons is

$$\tau_a = \frac{64\pi}{m_a^3 f_a^2}\,, \tag{1.33}$$

and taking the age of the Universe as $t_{\text{Univ.}} \approx 10^{10}$ years, the axion is a stable particle for $f_a \gtrsim 10^6$ GeV [51]. This confirms that the QCD axion is a good DM candidate, as f_a is in the allowed range of values if it is considered stable on the Universe timescale.

1.2.3 Galactic DM properties

When performing experimental searches, assumptions are made on the dark matter density distribution and velocity distribution in our Galaxy. Without entering in the detail of the structure of the galactic halo, we assume a local energy density value. This is estimated to lie in the range $(0.2 \lesssim \rho_{\text{dm}} \lesssim 0.56)$ GeV cm^{-3} [52], but the canonical value assumed by haloscope searches is $\rho_a = 0.45$ GeV cm^{-3}. Furthermore, virialization of the halo is assumed, so that velocities in the galactic frame follow a Maxwell-Boltzmann distribution.

The halo is considered at rest in the galactic frame, and the Maxwell-Boltzmann distribution of axion velocities is [53]

$$f(\nu) = \frac{2}{\sqrt{\pi}}\sqrt{\nu - \nu_a}\left(\frac{3}{\nu_a\langle\beta^2\rangle}\right)^{3/2} e^{-\frac{3(\nu-\nu_a)}{\nu_a\langle\beta^2\rangle}}\,. \tag{1.34}$$

This is the same as in [54], but expressed as a function of the measured signal frequency $\nu \geq \nu_a$. The rms velocity of the halo $\bar{v} = \langle v^2\rangle^{1/2}$ is about 270 km s^{-1} and $\langle\beta^2\rangle = \langle v^2\rangle/c^2$ is of order 10^{-3}. In a terrestrial laboratory, moving with respect to the galactic frame, the axion velocity becomes $\boldsymbol{v}_a = \boldsymbol{v} - \boldsymbol{v}_E$, where $\boldsymbol{v}_E$ is the Earth velocity with respect to the frame of the Galaxy. The main contribution to $\boldsymbol{v}_E$ is the velocity of the Sun in the Galaxy, with modulus

$v_s \simeq 230$ km s^{-1}. Consequently, in the lab frame the velocity distribution is modified in

$$f'(\nu) = \frac{2}{\sqrt{\pi}} \left(\sqrt{\frac{3}{2}} \frac{1}{r\nu_a \langle \beta^2 \rangle} \right) \sinh \left(3r \sqrt{\frac{2(\nu - \nu_a)}{\nu_a \langle \beta^2 \rangle}} \right) \exp \left(-\frac{3(\nu - \nu_a)}{\nu_a \langle \beta^2 \rangle} - \frac{3r^2}{2} \right), \tag{1.35}$$

where $r = v_s/\bar{v} \approx \sqrt{2/3}$. In Fig. 1.5 a comparison between the two distributions is shown. In the Earth frame, the velocity dispersion is increased.

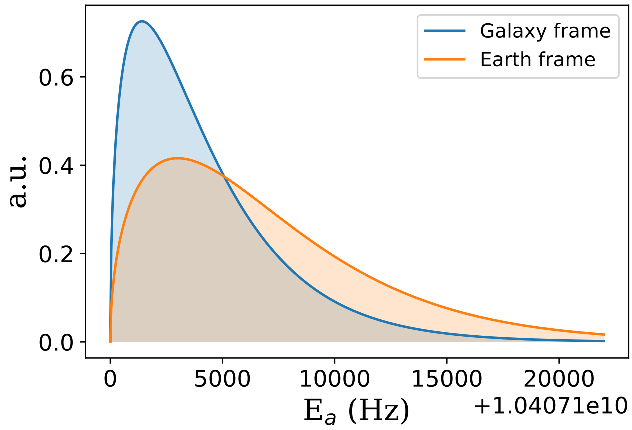

Figure 1.5: Maxwell-Boltzmann distribution of the halo in the galactic rest frame (blue) and modified distribution in the laboratory frame on Earth (orange). The distributions are the same as in [54], but expressed in frequency units.

The velocity distribution also defines the energy dispersion of halo axions. The axion energy is the sum of its rest mass and its kinetic energy, resulting in

$$E_a = m_a c^2 + \frac{1}{2} m_a \bar{v}_a^2 \simeq m_a c^2 \left[1 + \mathcal{O}(10^{-6}) \right], \tag{1.36}$$

thus the axion linewidth is very narrow. This can be also expressed as an axion quality factor, $Q_a = \Delta\nu_a/\nu_a \sim 10^6$.

Two other features of interest are the coherence length and the coherence time. The former is almost coincident with the De Broglie wavelength of the axion:

$$\lambda_a = \frac{2\pi}{m_a \bar{v}_a} \simeq 6.9 \left(\frac{200\,\mu\text{eV}}{m_a} \right) \text{ m}, \tag{1.37}$$

Qualitatively, it represents the region of space within which the axion field can be considered spatially homogeneous and constant. The coherence time is defined as

$$\tau_a \simeq \frac{2\pi}{m_a} Q_a, \tag{1.38}$$

and approximately indicates the time after which two points within the coherence length

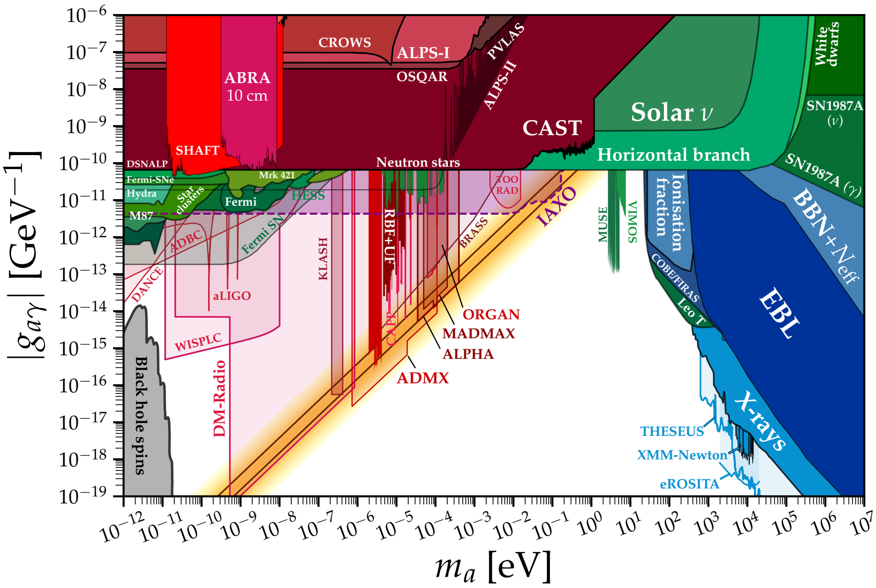

Figure 1.6: Parameter space $(g_{a\gamma\gamma}$ vs. $m_a)$, where all the experiments' sensitivity projections for the next future are shown. Source: https://cajohare.github.io/AxionLimits/ [46].

will dephase, as an effect of the axion linewidth in the frequency spectrum, albeit narrow.

1.3 Axion detection

In what follows, only detection techniques searching for the axion-photon interaction are taken into account. These exploit the fact that if the Maxwell equations in the presence of the axion field are written, the axion results as a source for electromagnetic fields, and vice versa. The three main categories of such experiments are light-shining-through-walls (LSW), haloscopes and helioscopes. A complete review on detection techniques is given in [5].

Fig. 1.6 is again a $(g_{a\gamma\gamma}$ vs. $m_a)$ parameter space, but with experiments' sensitivity projections for the next years, in addition to the measured upper bounds shown in Fig. 1.3. All the future experiments to which I refer in the following are present in this plot.

1.3.1 Laboratory experiments

Light-shining-through-walls experiments are pure laboratory searches and are very simple to understand. They exploit the Primakoff process of Fig. 1.2 to produce axion-like particles (ALPs) and then the inverse process to reconvert them into photons. The scheme is shown in Fig. 1.7. These experiments use laser beams injected in an optical cavity, where a static magnetic field is put. If an ALP is produced, it will pass through the opaque wall without interacting with it and will reach the second cavity. Here, another magnetic field is applied to stimulate the conversion of the ALP into a standard photon. The probability of the transition

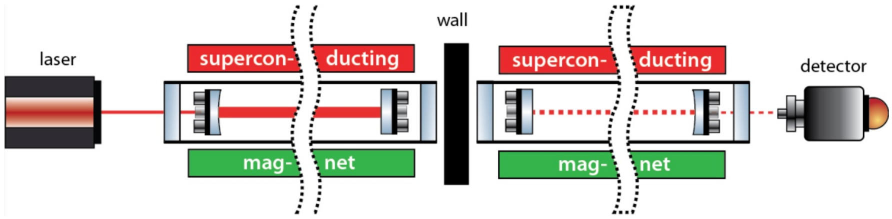

Figure 1.7: Sketch of an LSW experiment. Source: ALPS experiment website, https://alps.desy.de/.

$\gamma \to a \to \gamma$ is [49]:

$$P(\gamma \to a \to \gamma) = 16\frac{(g_{a\gamma\gamma}B\omega\cos\theta)^4}{m_a^8}\sin^2\left(\frac{l_1 m_a^2}{4\omega}\right)\sin^2\left(\frac{l_2 m_a^2}{4\omega}\right), \tag{1.39}$$

where θ is the angle between the laser polarization and the magnetic field, ω the laser frequency, B the static magnetic field and l_1, l_2 the lengths of the production and reconversion regions, respectively. This type of experiment is then sensitive to different mass values if the ratios l_i/ω are tuned opportunely. The probability can be enhanced if optical resonant cavities (Fabry-Perot) are employed in the production and regeneration regions.

Two experiments are currently using LSW techniques, ALPS (Any Light Particle Search) at DESY and OSQAR (Optical Search for QED vacuum bifringence, Axions and photon Regeneration) at CERN. They use dipole accelerator magnets: ALPS-I employed HERA magnets providing a 5 T field [55] and OSQAR employs CERN magnets up to 9.5 T [56]. ALPS-II will be the second phase of the ALPS experiment, with an enhancement in the sensitivity due to the installation of two straight strings with 12 HERA dipole magnets each, while a TES optical system will be exploited as the photon detector [57].

1.3.2 Haloscopes

The search for axion cold dark matter has some advantages over other axion searches: the large local axion number density, the coherence of the axion field oscillations and the application of a large external magnetic field.

The haloscope concept, along with the helioscope described in the next subsection, were proposed by Sikivie in 1983 [12] and further elaborated in 1985 by Sikivie [58] and Krauss, Moody, Wilczek, Morris [59]. Haloscopes are intended to detect axions constituting the galactic DM halo, in the hypothesis that all or part of the measured DM density is explained by axions. The detection technique relies on the inverse Primakoff interaction $a + \gamma^* \to \gamma$, where the virtual photon is provided by a static magnetic field. In this case, the emitted photon is collected in a microwave cavity and then the signal is read by some electronics (Fig. 1.8). Due to the small halo velocity dispersion, the axion power in a haloscope is enhanced when the cavity mode frequency matches the axion mass, $\nu_{\text{res}} = m_a c^2$. To scan over an as wide as possible range of axion masses, microwave cavities require the possibility to

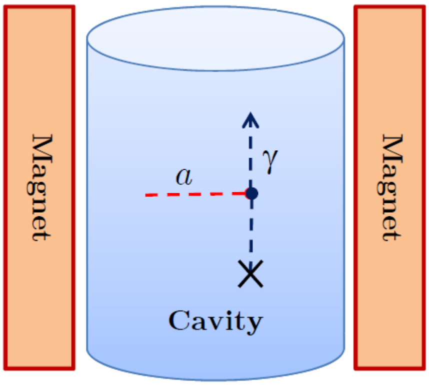

Figure 1.8: Sketch of a microwave cavity in which an axion-photon conversion occurs. Taken from [5].

fine tune their frequencies.

ADMX (Axion Dark Matter eXperiment) has become the paradigm of axion searches with haloscopes. It is the first experiment to reach the KSVZ line in the parameter space and, at present, the only one to reach the sensitivity down to the DFSZ line [60, 61]. The ADMX program also includes a plan to scan higher frequencies, covering a wide region of the parameter space with sensitivity to the DFSZ line and below (see Fig. 1.6).

Among other haloscopes are HAYSTAC [62], RADES [63], ABRACADABRA [64], ORGAN [65] and QUAX, to which Chap 3 is dedicated. The CAPP (Center for Axion and Precision Physics) in South Korea is active in overtaking all the technological challenges behind the improvements of a haloscope search and owns the two experiments CAPP-8T [66] and CAPP-9T [67].

In the category of dielectric haloscopes, two experiments have been proposed: BRASS [68] and MADMAX [69, 70]. As dielectric haloscopes do not rely on resonant conversion, in principle they are broadband axion receivers. In particular, MADMAX (Magnetized Disc and Mirror Axion Experiment) plans to use 80 dielectric disks, having a boost factor in the signal power of $\sim N_d^2$, where N_d is the number of disks. Adjusting the distance between disks, MADMAX should cover an exceptionally wide mass range, from 40 to 400 μeV, with sensitivity to DFSZ axions.

1.3.3 Helioscopes

The source helioscopes try to detect is the axion flux from the Sun. The photon regeneration takes place in a telescope-like structure pointed towards the Sun, where a high static magnetic field is applied. A scheme of the setup is shown in Fig. 1.9. Sikivie pointed out [12, 58] that the magnetic field has to be applied in an orthogonal direction with respect to the axion flux, in which case the polarization of the generated photon is parallel to the magnetic field, necessary to the electromagnetic interaction to take place.

The temperatures in the core of the Sun are around the keV, so axions with energies in the

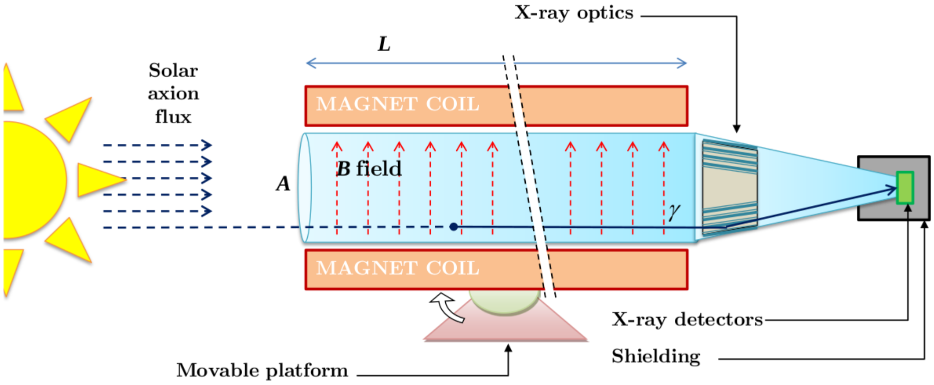

Figure 1.9: Conceptual scheme of a helioscope pointing towards the Sun. A high magnetic field is applied. Taken from [5].

keV range are produced herein. Subsequently, axions convert into x-ray photons, so modern helioscopes are equipped with x-ray focusing optics and x-ray detectors. The differential flux of ALPs at Earth in the 1–11 keV range, due only to the Primakoff process, is [5]:

$$\frac{d\Phi_a}{dE} = 6.02 \times 10^{10} \left(\frac{g_{a\gamma\gamma}}{10^{-10}\ \text{GeV}^{-1}} \right)^2 E^{2.481} e^{-E/1.205} \frac{1}{\text{cm}^2\,\text{s}\,\text{keV}}, \tag{1.40}$$

with the peak being at about 3 keV. In the equation, E is the ALP energy in keV units.

The reference helioscope experiment is CAST (CERN Axion Solar Telescope), which employs a powerful dipole magnet designed by INFN for LHC, up to 9 T over a length of 9.3 m, and the structure is able to track the Sun for some hours. It is also equipped with x-ray optics to focus the photons on the detector. CAST was able to give an upper limit on $g_{a\gamma\gamma}$ comparable to astrophysical bounds [71].

The improvements planned for CAST will converge in a new generation helioscope, the IAXO (International AXion Observatory) [72]. To achieve better sensitivity and signal-to-noise ratio, IAXO will improve the magnetic field strength, the dimensions of the conversion region and x-ray optics and detectors performances. The expected sensitivity on $g_{a\gamma\gamma}$ will be in the 10^{-12} GeV^{-1} region, an order of magnitude better than CAST (Fig. 1.6). Recently, an intermediate experiment to be sited at DESY has also been proposed, the BabyIAXO [73].

CHAPTER 2

Josephson junction devices

Josephson junctions (JJs) offer a testbed to observe the quantum mechanical behavior of a single macroscopic degree of freedom, the phase difference φ across two superconductors. JJs are fabricated as superconductor-insulator-superconductor (S-I-S) junctions, where tunneling processes of electrons or, more interestingly, electron pairs occur. Here it is assumed that the two superconductors are identical and the junctions are of the *weak-link* type, meaning that the thickness of the insulator barrier is enough to make sure that the superconductors are weakly coupled and electron pairs can tunnel.

In this Chapter, the basic principles governing Josephson junctions are presented, allowing the understanding of their use as single photon counters. In Section 2.5 I also give some insight into parametric amplification with a single Josephson junction. Section 2.6 finally contains a brief summary of the manufacturing processes for the realization of a JJ.

2.1 Josephson effect

Between the electrodes of an S-I-S junction, tunneling processes involving single excited electrons, called *quasiparticles*, lead to observable current flows. But in 1962 Josephson [74, 75] predicted an effect consisting in the tunneling of Cooper pairs across the two superconductors of an S-I-S junction without applying any potential. Therefore, current can flow through the junction in the absence of an applied electric or magnetic field, thanks to Cooper pairs of electrons carrying charge.

The Josephson equations can be derived from the Ginzburg-Landau theory of superconductors, as first Josephson did, or a classic approach due to Feynman [76] can be followed.

Here, the Schrödinger equations for the macroscopic wavefunctions $\Psi_{1,2} = (n_{1,2})^{1/2} e^{i\varphi_{1,2}}$ of the two superconductors are written, where $n_{1,2}$ are the densities of superelectrons and $\varphi_{1,2}$ their phases. Considering a bias voltage V between the two superconductors and assuming a coupling to account for the tunneling process, the Hamiltonians are manipulated to obtain the two Josephson equations:

$$\frac{\mathrm{d}\varphi}{\mathrm{d}t} = \frac{2e}{\hbar} V, \tag{2.1}$$

$$I = I_c \sin\varphi. \tag{2.2}$$

$\varphi = \varphi_2 - \varphi_1$ is the phase difference across the barrier, $I = JA$ is the current flowing through the barrier (with J the current density and A the junction area), and I_c is the *critical current*, a temperature-dependent parameter measuring how strongly the phases of the two electrodes are coupled through the weak link. Its temperature dependence is given analytically by the Ambegaokar-Baratoff formula [77]

$$I_c(T)R_n = \frac{\pi\Delta(T)}{2e} \tanh\left(\frac{\Delta(T)}{2k_B T}\right), \tag{2.3}$$

where $\Delta(T)$ is the superconductors' gap and R_n, the normal tunneling resistance, will be better explained later on.

From equations (2.1) and (2.2), four effects due to pair tunneling can be predicted: the dc and ac Josephson effects, described in the following, the inverse ac Josephson effect and the macroscopic quantum interference effect. The last two are mentioned shortly in Sec. 2.4.

dc Josephson effect. The dc Josephson effect is already explicit in equations (2.1) and (2.2). When no voltage V is applied, Eq. (2.1) results in $\varphi = \text{const}$, meaning that at zero voltage a dc current flows spontaneously only thanks to a phase difference. From Eq. (2.2), the current I is given by the value of the phase φ, while I_c represents the maximum current allowed.

ac Josephson effect. Considering a constant applied voltage V, Eq. (2.1) can be integrated to give $\varphi(t) = \varphi_0 + (2e/\hbar)Vt$, which gives a phase varying from 0 to 2π with the Josephson frequency $\omega_J/2\pi = 2eV/h$. The flowing current is then

$$I = I_c \sin\left(\omega_J t + \varphi_0\right), \tag{2.4}$$

being an alternating current with maximum amplitude I_c and frequency $\omega_J/2\pi$.

2.1.1 Ideal I-V characteristic

Before describing the processes that explain a Josephson junction I-V characteristic, it is useful to visualize the energy levels representation of a superconductor. This is sketched in

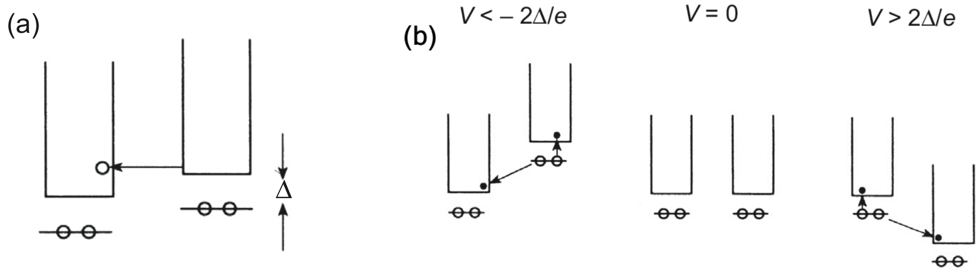

Figure 2.1: **(a)** Superconductor-to-superconductor tunneling in the Bose condensation representation at finite temperature, $T > 0$. **(b)** Tunneling in a biased S-I-S junction in the Bose condensation representation at zero temperature.

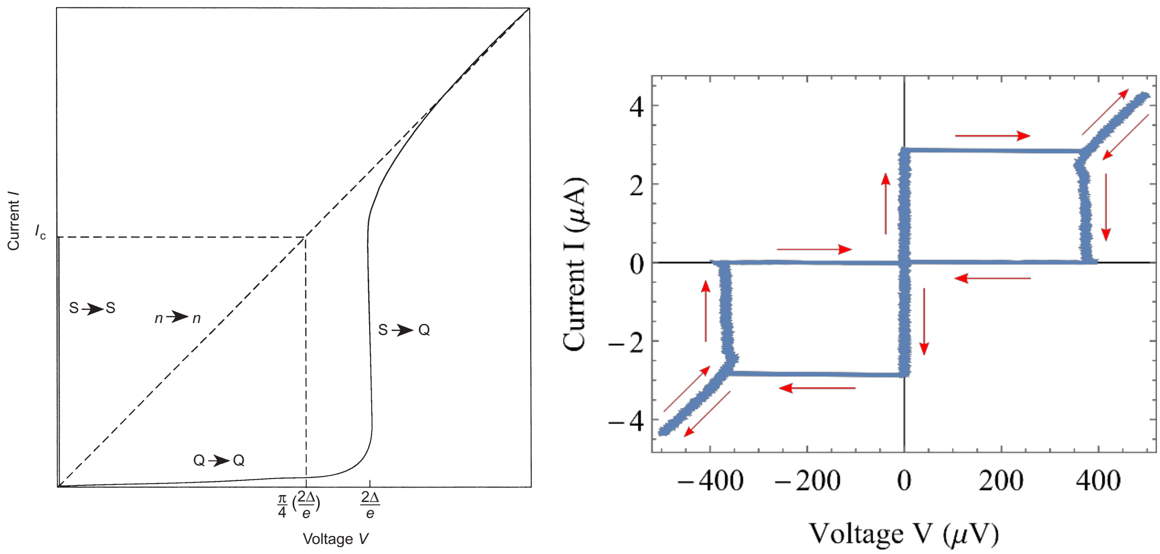

Figure 2.2: *Left*) I-V characteristic of an ideal Josephson junction, including tunneling of both Cooper pairs and quasiparticles. The image is taken from [78]. *Right*) I-V characteristic of a real Josephson junction, also showing the subgap branch. The red arrows indicate the succession of the I-V branches inspected during a current sweep.

Fig. 2.1, with all the tunneling processes described below. In the so-called Bose condensation representation, instead of a conduction band, superelectrons are placed in a single energy level, and this is possible because Cooper pairs are bosons. The conduction band, also called *quasiparticle state*, is placed at a distance Δ above the Cooper-pair level, and the binding energy E_g is shared by the two electrons, so that a single electron will have a binding energy $(1/2)E_g = \Delta$. At zero temperature, superelectrons only occupy the Cooper-pair level and are condensed, while above absolute zero some pairs break up and individual electrons are excited to the conduction band, populating it in a small fraction.

The I-V characteristic of an ideal JJ is shown in Fig. 2.2(left) and is antisymmetric with respect to the origin. The branches are due to different tunneling processes and are qualitatively described hereafter:

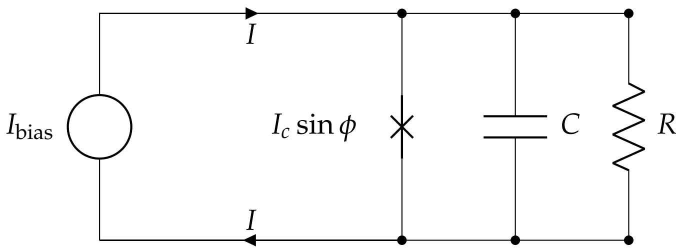

Figure 2.3: RCSJ model showing a dc source I_{bias} and the parallel of a pure JJ, its capacitance and its resistance.

- when the applied voltage is $V < 2\Delta/e$ or null, the only effect is described by the vertical branch on the y axis. This corresponds to the pure Josephson effect described by equations (2.1) and (2.2) and explains both the dc and ac Josephson effects, representing the tunneling of Cooper pairs through the barrier without destruction. This branch of the I-V curve is often called the *zero voltage state*.

- The $Q \to Q$ branch is due to the fact that at nonzero temperatures some individual electrons already occupy the conduction band (quasiparticle state), thus the tunneling takes place from the quasiparticle state of one superconductor to the quasiparticle state of the other (Fig. 2.1(a)).

- When the applied voltage is $V > 2\Delta/e$, there is the condition to break Cooper pairs of the superelectron band, with subsequent tunneling of a single electron from the Cooper-pair level of one superconductor to the quasiparticle state of the other (Fig. 2.1(b)). This is represented by the $S \to Q$ branch, showing a high tunneling resistance.

- When $V \gg 2\Delta/e$, the junction behaves as a N-I-N junction (N standing for normal metal), where the current I is proportional to the bias V, because the number of empty levels is proportional to V. This is represented by the linear branch on the top right of Fig. 2.2 (left) and (right). The resulting resistance is called *normal resistance* R_n.

2.1.2 RCSJ model

Since now, ideal Josephson junctions were described, but in general there can be other processes that cause current to flow in a junction. In this respect, the Resistively and Capacitively Shunted Junction (RCSJ) model, schematized by the equivalent circuit of Fig. 2.3, takes into account displacement currents (modeled by the capacitance C), conduction currents and quasiparticle tunneling currents (modeled by the resistance R). Therefore, C is the geometric capacity between the two electrodes and R takes into account dissipations in the junction[1]. The cross symbol represents the ideal junction and I_{bias} is a dc current driving the circuit.

[1] Actually, R is both voltage- and temperature-dependent, but here for simplicity it is considered constant to solve the RCSJ equations.

A Josephson inductance is also associated to the junction, that can be extracted by the two Josephson equations. It reads

$$L_J = \frac{\Phi_0}{2\pi I_c}\frac{1}{\cos\varphi}, \tag{2.5}$$

and is related to the kinetic energy of Cooper pairs. $\Phi_0 = h/2e \simeq 2.068 \times 10^{-15}$ Wb is the magnetic flux quantum.

The relation between the phase φ and the bias current is obtained by writing the circuit differential equation of the parallel channels:

$$I = I_c \sin\varphi + \frac{V}{R} + C\frac{\mathrm{d}V}{\mathrm{d}t}. \tag{2.6}$$

Eliminating V by the use of Eq. (2.1), with some manipulation the relation becomes

$$\frac{I}{I_c} = \frac{\mathrm{d}^2\varphi}{\mathrm{d}\tau^2} + Q^{-1}\frac{\mathrm{d}\varphi}{\mathrm{d}\tau} + \sin\varphi, \tag{2.7}$$

where the dimensionless parameter $\tau = \omega_{p0}t$ has been introduced, with ω_{p0} the *plasma frequency* of the Josephson junction with $I = 0$:

$$\omega_{p0} = \sqrt{\frac{2eI_c}{\hbar C}}. \tag{2.8}$$

$Q = \omega_{p0}RC$ is the *quality factor* of the junction and gives a quantitative indication of the dissipation. Note that the parameters R and C, and thus Q, can also account for external elements, so that Q includes the net dissipation processes in the junction.

Whatever value Q takes, two particular solutions to equation (2.7) always exist. When $I \leq I_c$ and $\mathrm{d}\varphi/\mathrm{d}t = 0$, we are left with the zero voltage solution $I = I_c \sin\varphi$, whereas for $I \gg I_c$ the solution is $I = V/R$, with $\mathrm{d}\varphi/\mathrm{d}t = \text{const}$, describing the resistive branch of Fig. 2.2. The intermediate solutions in which I is near the critical current depend on the Q value, which defines different regimes. For $Q \ll 1$, or small capacitance, the junction is said to be overdamped. In this case the first term on the right hand side of Eq. (2.7) is negligible, and the overdamped solution is[2]

$$V = R\left(I^2 - I_c^2\right)^{1/2} \qquad \text{for } I > I_c\,, \tag{2.9}$$

and is shown in Fig. 2.4a. The I-V curve smoothly interpolates between $V = 0$ and the resistive state $I = VR$.

When $Q > 1$ the junction is said to be underdamped (moderately damped if $Q \sim \mathcal{O}(1)$), and the I-V characteristic becomes hysteretic (see Fig. 2.4b). In fact, increasing I from 0, the junction stays in the zero voltage state until I_c; then, it suddenly jumps to the finite-voltage

[2]The voltage in these solutions is actually a time average of a series of periodic pulses, because φ slips by 2π.

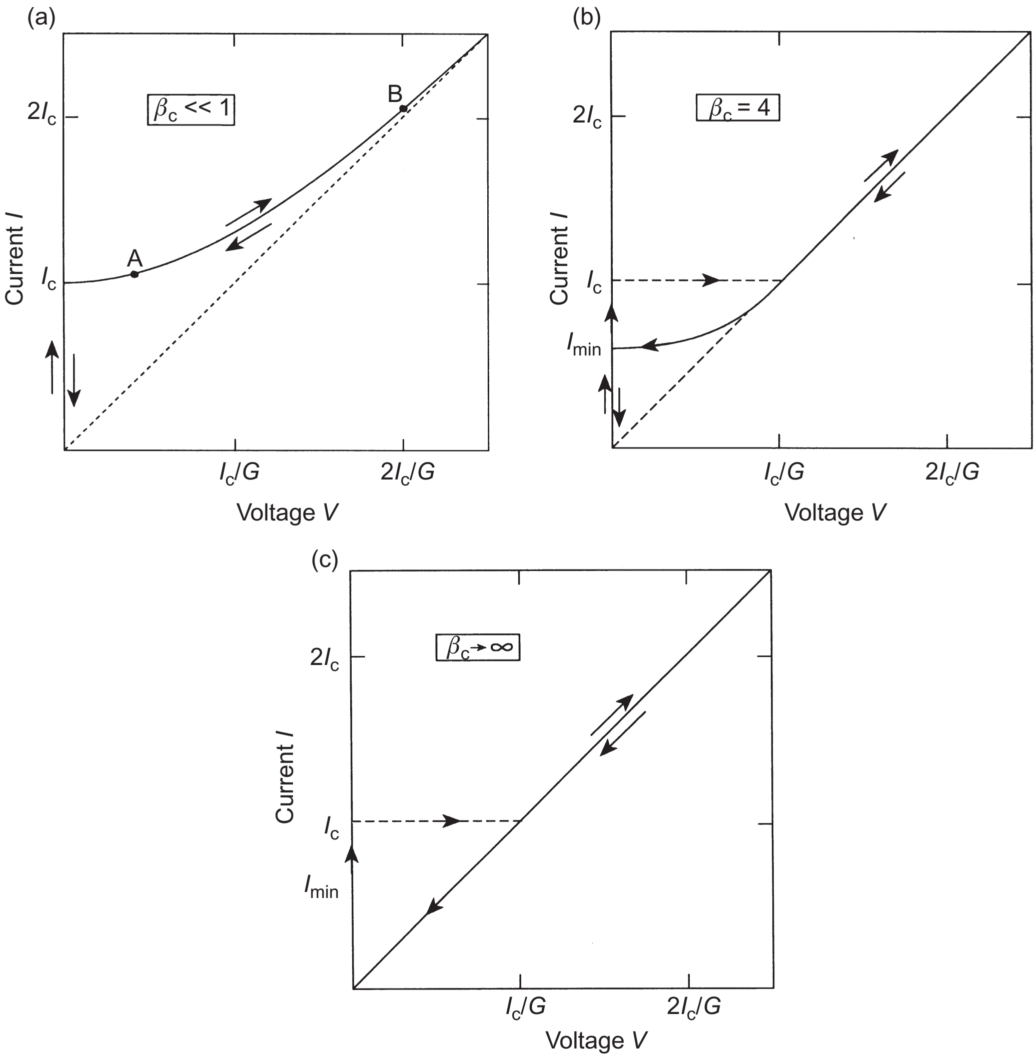

Figure 2.4: I-V solutions for **a)** overdamped junctions ($Q \ll 1$), **b)** moderately damped junctions ($Q > 1$) and **c)** underdamped junctions ($Q \gg 1$). In the figures, β_c is the Stewart-McCumber parameter, equal to Q^2. Images taken from [78].

state. If now the current is decreased, V does not jump back to zero, but rather remains finite until a *retrapping current* is reached:

$$I_r \approx \frac{4I_c}{\pi Q}. \tag{2.10}$$

More insight on the retrapping current is given in [79] and [80].

When $Q \gg 1$ (Fig. 2.4c), the underdamped solution presents maximum hysteresis, where the reduction of the voltage when decreasing the current from the voltage state follows a diagonal line into the origin.

Note that if R is considered constant, the subgap solution is not reproduced in the RCSJ model, and in fact the $S \rightarrow Q$ branch of Fig. 2.2 is not visible in Fig. 2.4. Actually, when $V < 2\Delta/e$, the resistance passes from its normal value R_n to a subgap resistance of order few thousand Ohms. This is because when $T \ll T_c$ the quasiparticle state is not populated and there is no quasiparticle tunneling.

2.2 Washboard potential

The *tilted-washboard model* is a mechanical analogue of the Josephson junction, useful to better understand the junction behavior and mechanisms. It gives a qualitative description of all the solutions to the dynamics of the junction (Eq. (2.7)), and will be helpful to visualize the escape processes described in Sec. 2.3 and the use of a JJ as a single photon counter (Chapters 5 and 6).

The model is based on the fact that the dynamics equation (2.7) is identical in form to the equation of motion of a mass particle moving along the φ axis subject to an effective potential

$$U(I,\varphi) = -E_J\left(\cos\varphi + \frac{I}{I_c}\varphi\right), \tag{2.11}$$

$$E_J = \frac{\hbar I_c}{2e} = \frac{\Phi_0 I_c}{2\pi},$$

and dragged by a viscous force, as schematized in Fig. 2.5a. The mass of the particle is related to the junction capacitance and is $(\hbar/2e)^2C$, while the drag force is inversely proportional to the resistance, $(\hbar/2e)^2(1/R)\mathrm{d}\varphi/\mathrm{d}t$. E_J is the Josephson coupling energy and gives the characteristic energy scale in equation (2.11).

The washboard potential, also shown in Fig. 2.5b for different biases, is a cosinusoidal tilted by the effect of the bias current I. When $I = I_c$, as in the green curve of Fig. 2.5b, the local minima become horizontal inflection points and when $I > I_c$ no stable points exist. The latter is the *running state*, corresponding to the finite voltage state described earlier where the phase varies continuously and slips by 2π, causing periodic voltage pulses. For $I < I_c$, ignoring thermal fluctuations, the particle mass is trapped within a local minimum, where the potential is approximately harmonic for small biases. Thus, the plasma frequency, which

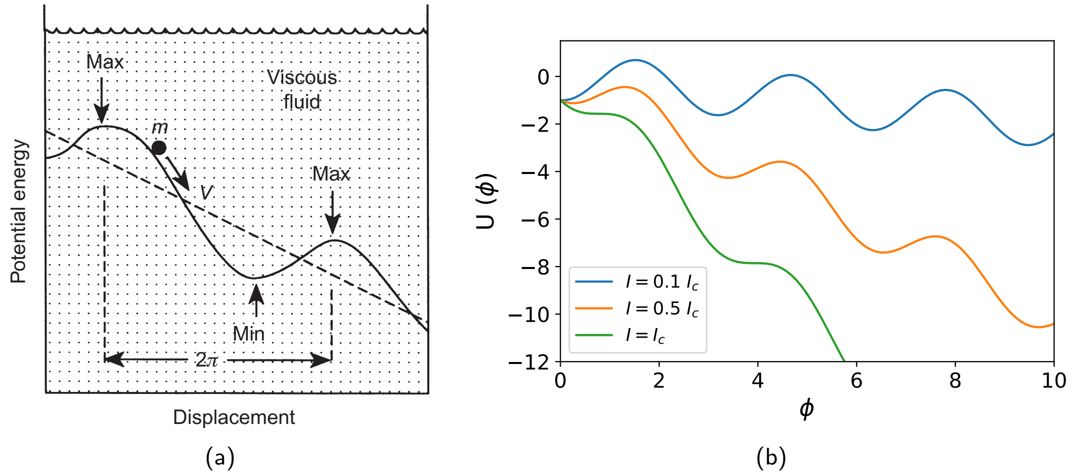

Figure 2.5: **a)** Washboard model representation of a Josephson junction. The particle mass moves along the φ coordinate in the washboard potential subject to a viscous force. The image is taken from [78]. **b)** Washboard potential (2.11) for different current biases.

for $I = 0$ is ω_{p0} (2.8), takes the meaning of the frequency of small oscillations around a minimum. For $I \neq 0$, the I-dependent plasma frequency for small oscillations is

$$\omega_p(I) = \omega_{p0}\left(1 - (I/I_c)^2\right)^{1/4}. \tag{2.12}$$

When the bias approaches I_c, the potential is heavily modified and the oscillations become anharmonic, so that the approximation (2.12) is no more valid.

The qualitative description of the solutions of the RCSJ equation (2.7) for $I > I_c$ in the picture of the washboard model is as follows. In the overdamped regime, the heavy damping ($Q \ll 1$) implies that the viscous drag dominates the inertia of the particle, so that the mass alternates slow slidings near the almost horizontal inflection points of the potential to subsequent quick drops down to the next inflection point. In the underdamped regime ($Q > 1$), when $I > I_c$, the running state corresponds to a steady sliding of the mass point down the inclined washboard. If I is decreased to zero, we have seen that V does not reaches zero until the retrapping current (2.10) is reached. This hysteresis is explained by the light damping: when sliding from one maximum to the next one while lowering the potential inclination, the energy supplied by the bias current is not fast enough dissipated by the mass point, so that it can overtake a barrier which otherwise, with heavy damping, would have stopped the mass point. Therefore, I_r is a direct probe of the damping.

2.3 Escape mechanisms

Escape mechanisms in a Josephson junction are well described by considering the tilted-washboard model just introduced. An escape or switching event is the passage from the

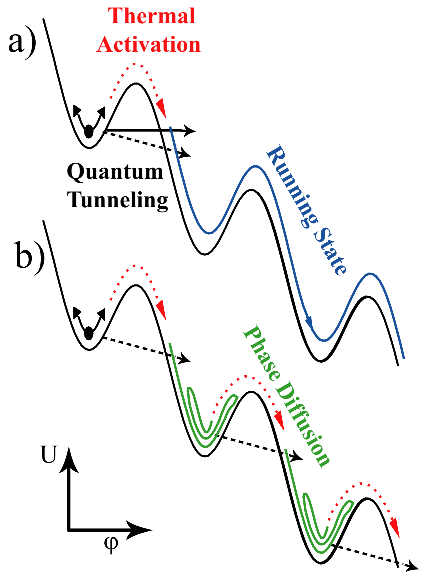

Figure 2.6: **a)** Thermal and quantum escapes representations in the tilted-washboard potential; the phase ends running down the potential after escape (voltage state). **b)** Diffusive motion of the phase, due to multiple retrappings after escapes. Taken from [81].

superconducting to the running state of a junction, and this can happen either by a thermal activation (TA) process or macroscopic quantum tunneling (MQT) through the potential barrier. Fig. 2.6 summarizes all the escape processes described in this Section. The energy scale to deal with in escape processes is the barrier height ΔU of the potential, between a minimum and the subsequent maximum:

$$\Delta U(I) = 2E_J\left(\sqrt{1-(I/I_c)^2} - (I/I_c)\arccos\left(I/I_c\right)\right), \tag{2.13}$$

that for low currents is approximated by $\Delta U \approx 2E_J\left(1 - I/I_c\right)^{3/2}$.

2.3.1 Thermal activation

The I-V curve of JJs is significantly affected by the presence of thermal fluctuations in the thermal bath. The effect of fluctuations on the phase particle in the potential is to raise and lower its energy by an amount k_BT. Therefore, when the energies are such that $k_BT \sim E_J$, the phase particle energy can overcome the barrier and, if the junction is in the underdamped regime, it accelerates down the washboard and will never retrap in an energy minimum. The probability per unit time of an escape due to thermal fluctuations has an exponential behavior $e^{-\Delta U/k_BT}$. The "attempt frequency" is the plasma frequency $\omega_p/2\pi$ (2.12), since it represents the characteristic frequency at which the mass particle oscillates back and forth in a potential well. Thus, the thermal escape rate ranges from low values proportional to e^{-2E_J/k_BT}, at small bias currents, to large values $\omega_p/2\pi \sim 10$ GHz near the critical current.

For a more precise quantification, we refer to the Kramers rate [82] for the thermal escape rate:

$$\Gamma_{TA} = a_t \frac{\omega_p}{2\pi} \exp\left(-\frac{\Delta U}{k_B T}\right), \tag{2.14}$$

where $a_t = 4/[(1 + Qk_BT/1.8\Delta U)^{1/2} + 1]^2$ is a damping-dependent prefactor valid for moderately underdamped junctions. Büttiker et al. [83] investigated the prefactor also in other regimes, giving the expressions for each one:

$$\begin{aligned}
a_t &= \sqrt{\left(\frac{1}{2Q}\right)^2 + 1} - \frac{1}{2Q} && \text{High-intermediate damping} \\
a_t &= \frac{4}{\left(\sqrt{1 + \frac{Qk_BT}{1.8\Delta U}} + 1\right)^2} && \text{Intermediate-low damping} \\
a_t &= Q && \text{High damping} \\
a_t &= 1 && \text{Intermediate damping} \\
a_t &= \frac{36}{5}\frac{\Delta U}{Qk_BT} && \text{Low damping.}
\end{aligned} \tag{2.15}$$

Operationally, upward current sweeps are performed to search for the value I_{sw} at which the junction switches to the running state. Since thermal escape is a stochastic process, I_{sw} follows a distribution with a mean value depressed with respect to I_c, because of the premature switching due to fluctuations; an approximated expression is [79]

$$\langle I_{sw} \rangle = I_c \left\{ 1 - \left[\left(\frac{k_B T}{2E_J}\right) \ln\left(\frac{\omega_p \Delta t}{2\pi}\right)\right]^{2/3} \right\}, \tag{2.16}$$

where Δt is the bias current sweep time. For a fully quantitative result, numerical calculations [84] are required. Note that the depression of I_{sw} is more and more evident with increasing temperature, being proportional to $-T^{2/3}$. The widths δI_{sw} of the distributions become smaller when decreasing temperature, since at low temperatures thermal fluctuations become unimportant.

Another method to treat thermal noise in a Josephson junction is to include a noise current source in the equation (2.7) describing the RCSJ model. An even more general approach is to write a Langevin equation and characterize fluctuations with the fluctuation-dissipation theorem, as done in Chap. 5.

2.3.2 Quantum tunneling

When $k_BT \ll E_J$, thermal fluctuations become irrelevant since the thermal escape probability is exponentially suppressed; therefore, this regime is dominated by quantum fluctuations. In this case, the potential wells are atom-like and energy levels are quantized, with the energy scale now being $\hbar\omega_p$. A quantum escape thus consists in the quantum tunneling of the phase particle through the barrier between two successive wells rather than hopping over it. The escape rate of the macroscopic quantum tunneling, due to [85], is

$$\Gamma_q = a_q \frac{\omega_p}{2\pi} \exp\left[-\frac{36}{5}\frac{\Delta U}{\hbar\omega_p}\left(1+\frac{0.87}{Q}\right)\right], \quad \text{with} \quad a_q = \sqrt{120\pi\left(\frac{36}{5}\frac{\Delta U}{\hbar\omega_p}\right)}\left(1+\frac{1.43}{Q}\right). \tag{2.17}$$

At first sight, Γ_q is temperature-independent. Actually, temperature plays a role, albeit minimal, since the critical current I_c present in ΔU, Q and ω_p modifies with temperature (see Eq. (2.3)). Therefore, the mean switching current and the width of the distributions is approximately constant with temperature.

The separation between the thermal and quantum regimes is expressed by the so-called crossover temperature [86]

$$T_{\rm cr} = \left(\frac{\hbar\omega_p}{2\pi k_B}\right)\left[\left(1+\frac{1}{4Q^2}\right)^{1/2} - \frac{1}{2Q}\right], \tag{2.18}$$

which is simplified to $T_{\rm cr} \approx \hbar\omega_p/2\pi k_B$ in underdamped junctions ($Q \gg 1$).

The thermal activation Γ_{TA} (2.14) and quantum tunneling Γ_q (2.17) escape rates look similar, so it is convenient to define a general escape rate $\Gamma_{\rm esc}$ and an escape temperature $T_{\rm esc}$ as follows [87]:

$$\begin{aligned} \Gamma_{\rm esc} &= \frac{\omega_p}{2\pi}\exp\left(-\frac{\Delta U}{k_B T_{\rm esc}}\right), \\ T_{{\rm esc},t} &= \frac{T}{(1-p_t)} \qquad \text{for } k_B T \gg \hbar\omega_p, \\ T_{{\rm esc},q} &= \frac{\hbar\omega_p}{7.2k_B}\frac{1}{1+0.87/Q}\frac{1}{1-p_q} \qquad \text{for } T=0, \end{aligned} \tag{2.19}$$

with $T_{{\rm esc},t}$ and $T_{{\rm esc},q}$ the escape temperatures in the thermal and quantum regimes, respectively. The factors p_t and p_q are

$$\begin{aligned} p_t &= \frac{\ln a_t}{\Delta U/k_B T}, \\ p_q &= \frac{\ln a_q}{(7.2\Delta U/\hbar\omega_p)\,(1+0.87/Q)}. \end{aligned} \tag{2.20}$$

In the thermal regime, T_{esc} is approximately equal to T, since a_t is of order 1 and then $|p_t| \ll 1$. Γ_{esc} is used when experimentally measured escape rates are compared with the predicted ones, since T_{esc} is nearly independent of the bias current.

Escape distributions are experimentally measured ramping several times the bias current from zero at a constant sweep rate $\mathrm{d}I/\mathrm{d}t$. The relation between the switching distribution and the escape rate is contained in the following equations: the probability that the junction switches in a current interval $I + \mathrm{d}I$ is $p(I)\mathrm{d}I$, with $p(I)$ given by [84]

$$p(I) = \frac{\Gamma(I)}{\mathrm{d}I/\mathrm{d}t}\left(1 - \int_0^I p(I')\mathrm{d}I'\right). \tag{2.21}$$

With measured values of $p(I)$, obtained by collecting the acquired switching currents in a histogram, it is possible to calculate an experimental escape rate:

$$\Gamma(I) = \frac{1}{\Delta I}\frac{\mathrm{d}I}{\mathrm{d}t}\ln\left(\frac{\sum_{i\geq I} p(i)}{\sum_{i\geq I+\Delta I} p(i)}\right), \tag{2.22}$$

where ΔI is the channel width of the analog-to-digital converter.

When performing data analysis, the comparison of the measured distributions $p(I)$ with theoretical models allows to extract many parameters of a junction, as the critical current I_c, its capacity C, its resistance R_n and the temperature T.

Phase diffusion Besides the thermal activation and the quantum tunneling mechanisms, a third regime can show up in the dynamics of Josephson junctions, the *phase diffusion* (PD) regime, and is typical of overdamped junctions. After escaping from one barrier, the phase is retrapped in an equilibrium state in the next minimum because of the heavy damping, rather than sliding down the potential in the running state. If this happens many times, the junction undergoes multiple retrappings and the phase performs a diffusive motion, generating small voltage pulses $V \ll 2\Delta/e$, making the detection difficult.

However, Kivioja et al. [88] showed that a phase diffusion regime is also present in underdamped junctions. The dynamics obey macroscopic quantum tunneling at low temperatures, $T < T_{\text{cr}}$, and thermal activation above the critical temperature, with the distribution widths following the Kramers behavior $\delta I_{\text{sw}} \propto T^{2/3}$. Suddenly, at higher temperatures, δI_{sw} sharply falls down and the mean switching currents $\langle I_{\text{sw}}\rangle$ saturate, so that the diffusive motion suppresses thermal escapes. This behavior is attributed to a frequency-dependent quality factor $Q(\omega)$, that changes the dynamics of the junction due to different dampings.

In other cases, as in [81], there is a direct transition from the MQT to the phase diffusion regime of underdamped junctions. If, in fact, a *turn-over* temperature T^* is defined as the temperature at which the derivative of δI_{sw} changes from positive (for TA events) to negative (for PD events), the thermal activation is suppressed when it happens that T^* is smaller than the crossover temperature between quantum and thermal escapes, $T^* < T_{\text{cr}}$.

A retrapping rate is often reported when treating retrapping processes [89], only valid for strongly underdamped junctions:

$$\Gamma_R = \omega_p \frac{I - I_r}{I_c} \sqrt{\frac{E_J}{2\pi k_B T}} \exp\left[-\frac{E_J Q^2}{2k_B T} \left(\frac{I - I_r}{I_c} \right)^2 \right], \tag{2.23}$$

where I_r is the retrapping current of equation (2.10).

All the three escape processes described above are summarized in Fig. 2.6.

2.4 Other effects

In Sec. 2.1 I described the dc and ac Josephson effects caused by constant biases. Here, two other predicted effects are briefly introduced, the inverse ac Josephson effect and the macroscopic quantum interference effect.

2.4.1 Inverse ac Josephson effect

In this case, dc voltages are induced in the junction by applying an rf current to it. The two consequences are the appearance of *Shapiro steps* and the so-called *photon-assisted tunneling* effect in the I-V characteristic of the junction.

The rf radiation source is incorporated in the RCSJ electrical circuit as a current generator $I_s \cos \omega_s t$, in parallel to the dc bias current I. The solution to the Josephson equations in this configuration contains Bessel functions and the I-V curve takes a staircase-like pattern, where the Shapiro steps occur at constant-voltage values proportional to the rf radiation frequency:

$$V_n = n\hbar\omega_s / 2e, \tag{2.24}$$

where n is an integer number. At this voltage values, Shapiro steps show as spikes, where the current can take any value along the spike itself.

In the photon-assisted tunneling, the rf current has an effect on the quasiparticle tunneling across the junction. Again, the solution for the quasiparticle tunneling current depends on Bessel functions, and in the I-V curve shifted images of the energy gap structure appear with a displacement

$$\Delta V_n = n\hbar\omega_s / e\,. \tag{2.25}$$

These current jumps look similar to the Shapiro steps, but their separation is twice as great and their amplitude is different.

2.4.2 Interference effects in presence of a magnetic field

Although magnetic fields applied to Josephson junctions are not treated in this thesis, the argument is worth of a mention since this constitutes, as an example, the basis for the functioning of superconducting quantum interference devices (SQUIDs), used as extremely sensitive magnetometers in many applications, including axion searches.

When a magnetic field is applied to a short Josephson junction[3], the phase difference across the barrier is affected, and the current flow is modulated by the magnetic flux:

$$I = I_c \sin\varphi_0 \frac{\sin(\pi\Phi/\Phi_0)}{\pi\Phi/\Phi_0}, \tag{2.26}$$

where Φ is the magnetic flux and φ_0 is the phase value at a reference point x_0 on the insulating barrier. This is called Josephson diffraction equation and has the same modulation pattern as the single-slit Fraunhofer diffraction experiment.

In the case of a superconducting loop made of two short junctions in parallel, the magnetic flux concatenated with the loop modulates the total current. Each obeys its own Josephson equation and their individual currents sum together. Thus, if for simplicity the junctions are considered identical (with the same critical currents), the maximum current through the edges of the loop is

$$I_{\text{max}} = 2I_c|\cos(\pi\Phi/\Phi_0)|, \tag{2.27}$$

which is the Josephson loop interference equation and has its analogue in the two-slit Young's experiment in optics. Note that a junction loop can be thought of as a single junction with tunable critical current, being it flux-dependent.

The dc SQUID is a practical circuit made of a two-junction loop which measures the small changes in magnetic flux thanks to the variations in the current, having sensitivity up to small fractions of the flux quantum, 10^{-6} or 10^{-7} $\Phi_0/\sqrt{\text{Hz}}$. The current variations are detected as a voltage change across the pair of junctions, making the SQUID a flux-to-voltage transducer. The relation between the voltage and the flux can be found by considering the I-V curve of the two-junction loop in the overdamped regime (2.9) (in fact, usually, a resistance is added to avoid hysteresis in SQUIDs):

$$V = \frac{R}{2}\sqrt{I^2 - [2I_c\cos(\pi\Phi/\Phi_0)]^2}, \tag{2.28}$$

where equation (2.27) has been used. This I-V curve shows that V is periodic in Φ with period Φ_0.

[3]Here the attention is limited to junctions with size such that the magnetic field generated by supercurrents is negligible with respect to the external one.

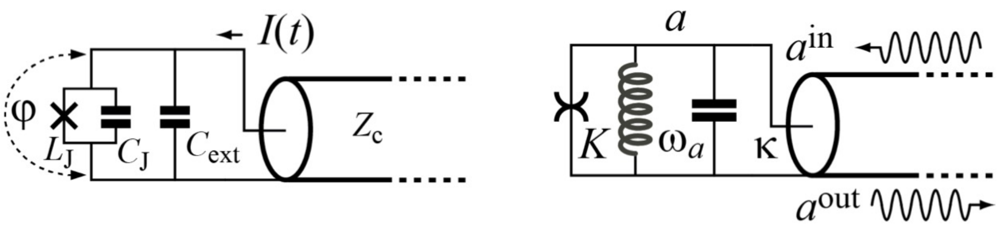

Figure 2.7: *Left*) Josephson junction amplifier schematic showing the JJ components L_J and C_J and an external capacity in parallel with C_J. *Right*) The JJ amplifier schematized as an oscillator at frequency ω_a shifted by a Kerr term K. κ is the coupling coefficient to the port, a is the photon ladder operator and a^{in} (a^{out}) the incoming (outgoing) waves.

2.5 Parametric amplification

When driven with microwave tones, called pumps here, the nonlinear inductance of Josephson junctions makes them behave as parametric amplifiers. The brief introduction to the argument is based on the review of Ref. [90]. We consider only the case of a one-mode one-port degenerate parametric amplifier involving a single Josephson junction, as in Fig. 2.7. The Hamiltonian of such a system is

$$\begin{aligned} H &= H_{\text{circ}} - \frac{\hbar}{2e}\varphi \cdot I + H_{\text{env}}\,, \\ H_{\text{circ}} &= -E_J \cos\varphi + \frac{Q^2}{2C_\Sigma}\,, \end{aligned} \tag{2.29}$$

where $C_\Sigma = C_J + C_{\text{ext}}$, the charge Q is the conjugate variable of the phase φ, with commutation relation $[\varphi, Q] = 2ei$, and H_{env} is the Hamiltonian describing the transmission line to which the junction is coupled. The term in $\varphi \cdot I$ is the interaction term. The cosine term is expanded to the fourth order and the φ^4 term is treated as a perturbation. φ is written with ladder bosonic operators, $\varphi = \varphi^{\text{ZPF}}(a + a^\dagger)$, where $\varphi^{\text{ZPF}} = (2e^2/\hbar)^{1/2}(L_J/C_\Sigma)^{1/4}$. In the Markov and rotating wave approximations, the circuit Hamiltonian then can be written as

$$\frac{H_{\text{circ}}}{\hbar} = \tilde{\omega}_a a^\dagger a + \frac{K}{2} a^\dagger a (a^\dagger a - 1), \tag{2.30}$$

where $K = -e^2/(2\hbar C_\Sigma)$ is the Kerr term which shifts the oscillator frequency: $\tilde{\omega}_a = 1/\sqrt{L_J C_\Sigma} + K$. The solution for the operator a is found by writing the quantum Langevin equation:

$$\frac{\mathrm{d}}{\mathrm{d}t} a = -i\left(\tilde{\omega}_a + K a^\dagger a\right) a - \frac{\kappa}{2} a + \sqrt{\kappa} a^{\text{in}}(t)\,, \tag{2.31}$$

where $a^{\text{in}}(t)$ is an input field and κ is the rate of excitation decay of the mode through the port. Input and output fields satisfy the boundary condition $a^{\text{out}} = -a^{\text{in}} + \sqrt{\kappa} a$.

For a^{in} a pump tone with amplitude α^{in} and frequency Ω is considered. Writing a as $a(t) = \alpha e^{-i\Omega t} + \delta a(t)$, where δa is the signal field, the solution for α is found from Eq. (2.31) in terms of α^{in}. Then, the effective Hamiltonian for the degenerate parametric amplifier becomes

$$\frac{H}{\hbar} = \omega_a \delta a^\dagger \delta a + \left(g_{aa} e^{i(\Omega_{aa}t+\theta)} (\delta a)^2 + \text{h.c.} \right), \tag{2.32}$$

with $\omega_a = \tilde{\omega_a} + 2K|\alpha|^2$, $g_{aa}e^{i\theta} = K\alpha^{*2}/2$ and $\Omega_{aa} = 2\Omega$. Note that the parametric oscillation term with Ω_{aa} is at twice the pump frequency Ω, which in our case is in the vicinity of the JJ frequency, being the relation $\omega_s + \omega_i = 2\Omega$ valid, where ω_s is the frequency of the amplified signal and ω_i its image (or *idler*) frequency.

The solution of the a field, expressed with its in-phase and quadrature components, is:

$$\begin{aligned} a_\parallel^{\text{out}}[\delta\omega] &= \frac{|\chi_a^{-1}(\omega_S)|^2 + 2\rho_{aa} + \rho_{aa}^2}{D} a_\parallel^{\text{in}}[\delta\omega] \equiv \Lambda_\parallel(\delta\omega)\, a_\parallel^{\text{in}}[\delta\omega] \\ a_\perp^{\text{out}}[\delta\omega] &= \frac{|\chi_a^{-1}(\omega_S)|^2 - 2\rho_{aa} + \rho_{aa}^2}{D} a_\perp^{\text{in}}[\delta\omega] \equiv \Lambda_\perp(\delta\omega)\, a_\perp^{\text{in}}[\delta\omega], \end{aligned} \tag{2.33}$$

where $D = \chi_a^{-2} - \rho_{aa}^2$, $\rho_{aa} = 4g_{aa}/\kappa$ and $\chi_a^{-1}(\omega_s)$ is the inverse of

$$\chi_a(\omega_s) = \frac{1}{1 - 2i(\omega_s - \omega_a)/\kappa}. \tag{2.34}$$

The gain of the two quadratures finally is $G_{\parallel,\perp} = |\Lambda_{\parallel,\perp}(\delta\omega)|^2$. They must obey the unitarity relation $G_\parallel G_\perp = 1$, with the consequence that in the degenerate parametric amplifier one quadrature of the signal is amplified while the other is deamplified.

2.6 Fabrication of Josephson junctions

The processes involved in the fabrication of a Josephson junction strongly depend on the available machines and on the required construction parameters of a junction, so that every fabrication has a different recipe. Therefore, in what comes I will only concentrate on the fundamental passages followed for the fabrication of our Josephson junction characterized in Chap. 6, without entering in many recipe details.

The junction is an $Al/AlO_x/Al$ one, manufactured at IFN-CNR with a two-angle shadow mask evaporation technique. The fundamental processes are summarized in Fig. 2.8 and are an electron-beam lithographic etching (1), development (2), aluminum evaporations (3 and 5) with an oxidation in between (4), lift off (6).

The starting point is to prepare the silicon chip substrate; sometimes gold leads are first fabricated and then the junction is deposited in a second step. In our case, we skipped the first step and directly deposited the junction on the chip. The preparation of the wafer consists in spinning the two resist layers that will constitute the mask which is needed to perform the undercut for the later two-angle shadow evaporation. To do this, the wafer is put on a hot plate and the two layers are spun one at the time. The first layer is a copolymer

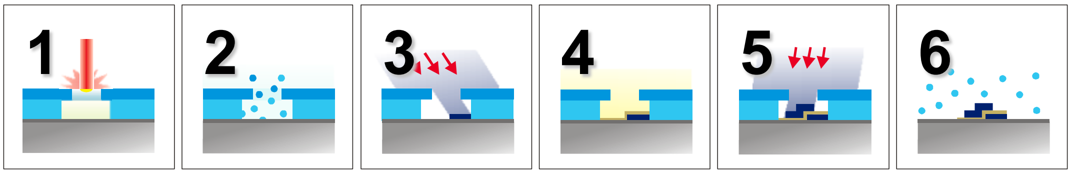

Figure 2.8: Fundamental fabrication processes of a JJ. **1)** Electron beam lithography; **2)** development; **3)** Al evaporation; **4)** oxidation; **5)** Al evaporation; **6)** lift off.

of thickness of about 1 μm and the second is a PMMA resist with thickness of about 1 μm.

Then, the processes from 1 to 6 of Fig. 2.8 are executed. **1)** As a first step, the structure to be written by the electron beam has to be designed with a software and the file loaded to the machine. Then, the bilayer on the chip is etched by electron beam lithography (EBL). We use a Raith Voyager EBL machine, with maximum accelerating voltage of 50 kV. The exposure is performed automatically, as the file contains informations on the geometry, exposure parameters (as current, dose etc.) and type and thicknesses of the resist materials. **2)** The development is done in a mixture of two chemicals, isopropanol and methyl isobutyl ketone (MIBK) in our case, necessary to produce the undercut for the evaporation processes. The chip is then rinsed in isopropanol and dried with a nitrogen gun. **3)** The evaporation is done with an electron gun evaporator. The Al source is prepared and the evaporation chamber is pumped down. Then, the source is evaporated at an angle of 155° relative to an axis coplanar to the chip surface, since an Al thickness of about 30 nm is reached on the chip. **4)** Thanks to a load lock, the oxidation can be performed immediately after the first evaporation, because the evaporation chamber remains in vacuum. Oxygen is injected at a pressure of 3 mbar for 5 minutes and then evacuated. Note that these are the parameters defining the thickness of the junction barrier and its capacity. **5)** The chip is subsequently rotated to assume an angle of 90° and the second Al layer is deposited with the same evaporation process as point **4**, again with thickness of about 30 nm. **6)** The lift off procedure serves to strip off the resists from the wafer, leaving only the deposited junction. This is done in warm acetone, which is able to dissolve the resists; then, a small pipette is used to blow off the remaining material. In some cases, if the latter technique does not work properly, an ultrasonic bath is also used, but there is the chance to destroy the junction.

Finally, the chip is rinsed into isopropanol, dried with a nitrogen gun, and then an optical microscope is used to check the lift off completion.

CHAPTER 3

Axion searches with the QUAX experiment

QUAX (QUest for AXions) is an experiment whose collaboration involves researchers at the Laboratori Nazionali di Legnaro (LNL) and Laboratori Nazionali di Frascati (LNF) of the Istituto Nazionale di Fisica Nucleare (INFN). The experiment searches for the interaction of the dark matter axions coming from the galactic halo either with electrons, within the so-called QUAX–ae activity, or with photons, within the QUAX–aγ activity. During my time spent at LNF, I joined the QUAX–aγ tasks, thus in this chapter I briefly summarise the QUAX–ae current status (Sec. 3.1) and more thoroughly present the QUAX–aγ latest result (Sec. 3.2), an axion search at $m_a = 43\ \mu$eV involving a Josephson parametric amplifier as the preamplification stage. My contribution consisted in carrying out the analysis procedure and subsequent preparation of the related paper [2].

3.1 QUAX–ae

The QUAX–ae experiment, whose operation is conducted at LNL, exploits a ferromagnetic haloscope, a concept similar to that of the Sikivie haloscope but with some differences in the interaction mechanism used to detect axions. In fact, it is based on the interaction between axions and the spin of electrons, thus inducing magnetization oscillations in the target material which are then converted into photons in a microwave cavity. The original idea of exploiting excitations of a ferromagnet (magnons) for the axion detection came from the authors of Ref. [91] and was then resumed in the QUAX proposal almost thirty years later [92].

As a starting point, they considered the axion-electron interaction Lagrangian (1.25) (the same form is applicable to each fermion)

$$\mathscr{L}_{aee} = -i\, g_{aee}\, a(x)\overline{\psi}(x)\gamma_5\psi(x), \tag{3.1}$$

where $\psi(x)$ is the electron spinor and g_{aee} is a dimensionless coupling constant. The associated diagram is reported in Fig. 3.1.

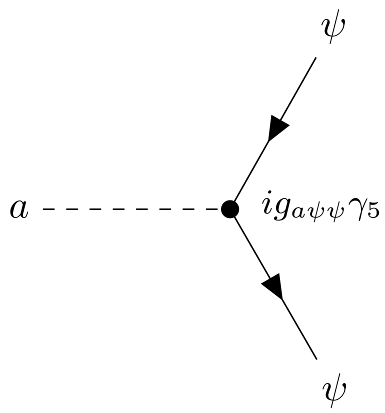

Figure 3.1: Feynman diagram of the generic interaction between the axion and fermions.

Including the interaction (3.1) in the free-electron Lagrangian and taking the nonrelativistic limit of the Euler–Lagrange equation, the evolution of an electron interacting with an axion is given by the Schrödinger equation

$$i\hbar\,\partial_t\varphi = \left(-\frac{\hbar^2}{2m_e}\nabla^2 - \frac{g_{aee}\hbar}{2m_e}\boldsymbol{\sigma}_e\cdot\boldsymbol{\nabla}a\right)\varphi, \tag{3.2}$$

with $\boldsymbol{\sigma}_e$ the vector of the Pauli spin matrices. Besides the kinetic energy, the second term on the rhs has the form of an interaction between the spin magnetic moment and a magnetic field, since it can be noted that

$$-\frac{g_{aee}\hbar}{2m_e}\boldsymbol{\sigma}_e\cdot\boldsymbol{\nabla}a = -2\frac{e\hbar}{2m_e}\boldsymbol{\sigma}_e\cdot\left(\frac{g_{aee}}{2e}\right)\boldsymbol{\nabla}a \equiv -2\mu_B\boldsymbol{\sigma}_e\cdot\boldsymbol{B}_a. \tag{3.3}$$

μ_B is the Bohr magneton of the electron, and an effective magnetic field has been defined:

$$\boldsymbol{B}_a \equiv \left(\frac{g_{aee}}{2m_e}\right)\boldsymbol{\nabla}a. \tag{3.4}$$

Therefore, the effect of the axion is that of an effective magnetic field interacting with the spins of electrons. The process can be thought of as an absorption of the axion causing a spin flip, with the macroscopic consequence of changing the magnetization of the sample containing the spins.

The detection principles depend on the characteristic of the effective magnetic field $\boldsymbol{B}_a$ and the magnetization of the ferromagnet. $\boldsymbol{B}_a$ is an oscillating magnetic field at radio-frequencies and its properties derive from the axion field, that for simplicity can be considered as a coherent classical field (details can be found in [92]). As a magnetic sample, a high spin density material has to be chosen, as clarified in a while, and it is initially polarized with a static magnetic field B_0 along a given direction (say $\hat{z}$). Consequently, the sample acquires a magnetization M_0 along the $\hat{z}$ axis. Contrary to the case of the axion-photon coupling, B_0 only serves as a polarizing field and does not affect the intensity of the interaction. Typical values for the QUAX case are at the level of 1–2 T, thus being easily obtainable.

The effect of $\boldsymbol{B}_a$ is to drive oscillations of the magnetization in a plane perpendicular to the $\hat{z}$ axis, and the mode of the uniform precession that is established is called Kittel mode [93]. The equations governing the time evolution of the $\hat{x}$, $\hat{y}$ and $\hat{z}$ components of $\boldsymbol{M}$ are the Bloch equations [94]. These also include damping terms due to spin-spin relaxation, spin-lattice relaxation, and the radiation damping term. The latter is due to the reaction of the material to its own radiation [95, 96], and at microwave frequencies this is the limiting factor. To make its contribution ineffective, the phase-space of the radiated light is limited by putting the magnetic sample in a microwave cavity. Note that when the frequency of the Kittel mode is close to the resonance frequency of the cavity, hybridization between the two modes occurs. A detailed description of the hybridized system can be found in [92, 97–99].

The resulting time-dependent magnetization $M_a(t)$ is then

$$M_a(t) = \gamma_e \mu_B B_a n_s \tau_{\text{min}} \cos \omega_a t, \tag{3.5}$$

where $\gamma_e = e/m_e$, n_s is the sample spin density, $\nu_a = \omega_a/2\pi$ is the frequency of the oscillating magnetic field $B_a(t)$, and τ_{min} is the minimum between the axion relaxation time and the hybrid system relaxation time.

The average power deposited in the cavity after an axion interaction can be obtained by

$$P_{\text{in}} = B_a \frac{\mathrm{d}M_a}{\mathrm{d}t} V_s = \gamma_e \mu_B N_s \omega_a B_a^2 \tau_{\text{min}}, \tag{3.6}$$

where $N_s = n_s V_s$ is the number of spins. For a cavity read by a critically coupled antenna, the output signal is finally $P_{\text{out}} = P_{\text{in}}/2$. Therefore, besides the quantities fixed by axion physics, the output power from an axion-electron interaction depends on n_s, V_s and τ_{min}. To increase P_{out}, N_s and τ_{min} must be large, so a suitable sample has a high spin density and a narrow linewidth. The best material identified so far is Yttrium Iron Garnet (YIG), with roughly $n_s \simeq 2 \times 10^{28}$ m^{-3} and 1 MHz linewidth. τ_{min} is the most limiting factor and is dominated by the decoherence time of resonant cavities. The goal is to build resonant cavities in such a way that the relaxation time is only naturally limited by the axion field decoherence.

In the expression for P_{out}, the effective magnetic field $B_a(t)$ depends on axion properties, including the axion-electron coupling constant g_{aee}. Thus, the expression for the latter can be obtained by inverting P_{out} (Eq. (3.6) divided by 2). When performing an axion search with no observed signal, the power P_{out} is substituted with the measured noise power σ_P, and an upper limit on g_{aee} is set:

$$g_{aee} < \frac{e}{\pi m_a v_a} \sqrt{\frac{2\sigma_P}{2\mu_B \gamma_e n_a N_s \tau_s}}, \tag{3.7}$$

where v_a is the speed of the axion wind perceived on an Earth-based laboratory (see subsection 1.2.3), n_a is the axion number density in our galaxy, and τ_s is the relaxation time of the hybrid system.

The most recent QUAX-ae ferromagnetic axion search [99] is done with ten YIG spheres of 2.1 mm diameter, coupled to the TM110 mode of a cylindrical cavity of frequency 10.7 GHz. The system is housed in a dilution refrigerator with base temperature 90 mK and the preamplification stage consists of a JPA, which is described later in subsec. 3.2.2, with a total noise temperature of $T_n = 0.99$ K. The magnetic field B_0 is varied to obtain a 120 MHz scan in the mass range $42.4 - 43.1$ μeV. The upper limit set in this range is $g_{aee} \leq 1.7 \times 10^{-11}$ at 95% CL (Fig. 3.2), currently making QUAX-ae the most sensitive magnetometer for the axion search.

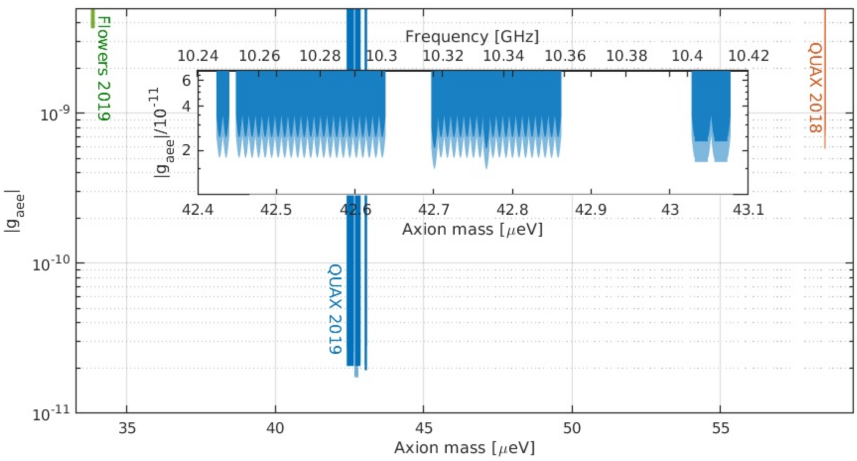

Figure 3.2: 95% upper limit on g_{aee} obtained with the described QUAX-ae ferromagnetic haloscope. The DFSZ model line is at $g_{aee} \simeq 10^{-15}$. Other axion-electron coupling searches are [98] (orange) and [100] (green). The inset shows a detail of the reported measurement.

3.2 QUAX–aγ

The QUAX-aγ experiment exploits the classical haloscope detection scheme, relying on the axion-photon interaction. From equations (1.21) and (1.23), the Lagrangian of the axion cou-

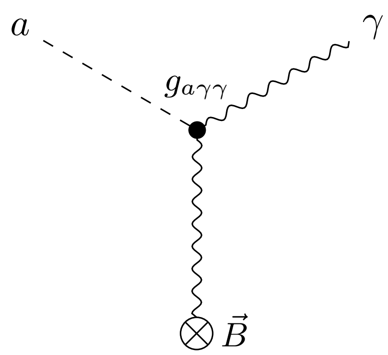

Figure 3.3: The inverse Primakoff effect. An axion coming from left absorbs a photon of the magnetic field $\boldsymbol{B}$ and is converted into a photon on the right (the electric field in the case of a resonant cavity).

pling to the electromagnetic field is

$$\mathscr{L}_{a\gamma\gamma} = -g_{a\gamma\gamma}\, a(x)\, \boldsymbol{E} \cdot \boldsymbol{B}, \tag{3.8}$$

where $\boldsymbol{E}$ is the electric field of a resonant mode which is excited in the resonant cavity and $\boldsymbol{B}$ is the external magnetic field. The interaction is schematized in Fig. 3.3.

Following the derivation of Sikivie [58] and the revisited calculations of [43], the signal power of an axion-photon conversion can be obtained starting from Maxwell's equations including the axion field. The cavity walls impose the boundary conditions to the equations, leading to an expression for the electric field of the cavity modes as a function of $a(x)$ and $g_{a\gamma\gamma}$. Then, the energy U transferred by the axion field oscillations and stored in the resonant cavity is written as the sum of electromagnetic modes. Finally, the power that is collected from the cavity is the power dissipated on the receiver (an antenna in this case): $P_{\text{sig}} = \omega_c U/Q_r$, where $\omega_c/2\pi$ is the cavity resonance frequency and Q_r the receiver quality factor, taking into account the fraction of the energy transferred to the receiver itself. The final form of the signal power becomes

$$P_{a\gamma} = \left(\frac{g^2_{a\gamma\gamma}}{m_a^2}\, \hbar^3 c^3 \rho_a \right) \times \left(\frac{\beta}{1+\beta} \omega_c \frac{1}{\mu_0} B_0^2 V C_{mnl} Q_L \frac{1}{1 + (2 Q_L\, \delta\omega/\omega_c)^2} \right). \tag{3.9}$$

In (3.9), theory and detector parameters are grouped separately in the first and second sets of parentheses, respectively. ρ_a is the local galactic DM energy density, and is taken to be $\rho_a = 0.45\ \text{GeV}/\text{cm}^3$ [4]. In the second set of parentheses, the parameters that can be actually adjusted in a haloscope show up. Whilst ω_c and partially V, the cavity volume, are fixed by the axion mass to search for, the detector's β, Q_L and B_0 are tunable. It is worth noting that the power goes with the square of the applied magnetic field B_0. Q_L is the loaded quality factor of the cavity, expressed as

$$\frac{1}{Q_L} = \frac{1}{Q_0} + \frac{1}{Q_r}, \tag{3.10}$$

where Q_0 is the unloaded quality factor, defining the cavity losses only due to the nonzero resistivity of the walls. β is the cavity coupling coefficient and is defined as $\beta = Q_0/Q_r$; this quantifies the fraction of the signal power extracted from the cavity with the receiver and can be changed allowing antennas to be tuned in a haloscope. From the definition of β, the loaded quality factor can also be rewritten as

$$Q_L = \frac{Q_0}{1+\beta}. \tag{3.11}$$

The form factor C_{mnl} parametrizes the overlap between the cavity mode's electromagnetic field and the external magnetic field, defining a sort of effective detection volume VC_{mnl}. Its value depends on the mode indexes m, n, l and is $C_{mnl} < 1$. The last fraction in the second set of parentheses of eq. (3.9) is a Lorentzian term taking into account the cavity resonance lineshape: the maximum enhancement is achieved at the resonance peak and then the power degrades with increasing detuning $\delta\omega$ from ω_c.

The following sections (3.2.1–3.2.4) describe in detail the setup of the latest QUAX-aγ measurement and the analysis procedure involved to extract the axion-photon coupling upper limit. The results are also published in [2].

3.2.1 LNL haloscope

The haloscope operated for the axion search, shown in Fig. 3.4, is assembled at LNL and is composed of a cylindrical oxygen-free high conductivity (OFHC) copper cavity with an inner radius of 11.05 mm and length 210 mm, inserted inside the 150 mm diameter bore of an 8.1 T superconducting (SC) magnet of length 500 mm. The total volume of the cavity is $V = 80.56\,\mathrm{cm}^3$. The whole system is hosted in a dilution refrigerator with a base temperature of 90 mK. Each cavity endplate hosts a dipole antenna in the holes drilled on the cavity axis. The cavity is treated with electrochemical polishing to minimize surface losses. The working electromagnetic mode is $TM010$, and for a cylindrical cavity the value of the form factor appearing in eq. (3.9) results $C_{010} = 0.69$. We have measured the resonance peak of the $TM010$ mode at 150 mK and with the magnet on, with a vector network analyzer, obtaining the frequency $\nu_c = 10.4018$ GHz and an unloaded quality factor $Q_0 = 76,000$, in agreement with expectations from simulations performed with the ANSYS HFSS suite [101]. During data-taking runs, the cavity is critically coupled to the output rf line and the loaded quality factor is measured to be about $Q_L = 36,000$.

The rf setup is the same as our previous measurement of the QUAX-ae experiment [2]

Figure 3.4: View of the QUAX$-a\gamma$ dilution refrigerator insert, instrumented with the resonant cavity (at the bottom) and amplification chain. In the background, the 8.1 T magnet with its countercoil is visible.

(Sec. 3.1) and is shown in Fig. 3.5. It consists of four rf lines used to characterize and measure the cavity signal and to determine attenuations and gains. Starting from the left of Fig. 3.5, the "SO" line connects the source oscillator to the fixed, weakly coupled antenna D2 and is used to inject calibration and probe signals into the cavity. The "Pump" line connects the pump-signal generator to the corresponding "p" port of a JPA amplifier (described in 3.2.2). The cavity is critically coupled to the "Readout" line through antenna D1, tunable via a micrometric screw. The emitted power enters the JPA on the "s" port and is reflected, amplified, toward the HEMT cryogenic (A1) and HEMT room-temperature (A2) amplifiers. The signal is then downconverted with an I-Q mixer with a 100 MHz IF band; the phase and quadrature components of the heterodyne signal are postamplified in a 10 MHz band and finally sampled via an analog-to-digital converter (ADC) with a 2 MHz bandwidth. The "Aux" line is an auxiliary line introduced for calibration purposes. To minimize the Johnson noise contribution at the coldest stage, we insert attenuators and circulators in the rf lines. A nonoptimal attenuation of the "Aux" line with 10 dB attenuation at 1 K and 10 dB at 150 mK causes an excess Johnson noise of about 95 mK on the circulator and on the cavity (since they are thermally connected), corresponding to an effective temperature of the circulator of 273 mK at 10 GHz. We monitor the temperatures with RuO_2 thermometers, one in thermal contact with the cavity and the other with the mixing chamber. Due to some unexpected behavior of the thermometers, we only estimate a temperature between 100 mK and 150 mK

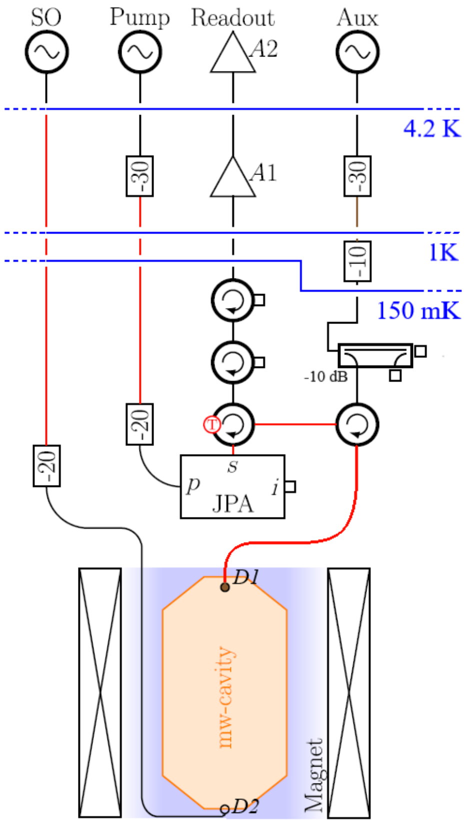

Figure 3.5: Schematics of the experimental apparatus. The microwave cavity (orange) is immersed in the uniform magnetic field (blue shaded region) generated by the magnet (crossed boxes). A1 and A2 are the cryogenic and room-temperature amplifiers, respectively. The JPA amplifier has three ports: signal (s), idler (i), and pump (p). Superconducting cables (red) are used as transmission lines for rf signals from the 4 K stage to the 150 mK stage. Thermometers (red circled T) are in thermal contact with the resonant cavity and the signal port on the JPA. Attenuators are shown with their reduction factor in decibels. The horizontal lines (blue) identify the boundaries of the cryogenic stages of the apparatus, with the cavity enclosed within the 150 mK radiation shield. The magnet is immersed in liquid helium.

in the mixing chamber and between 200 mK and 250 mK on the cavity.

3.2.2 JPA

Although HEMTs possess optimum noise performances, the best haloscope sensitivities using available devices are achieved with JPAs, linear amplifiers with thermal noise at the quantum limit. Details on the fundamentals of parametric amplification can be found in Chap. 2. The JPA in our setup is of the type described in [102], has been developed by the same group and is schematized in Fig. 3.6. It is made up of a ring of four Josephson junctions functioning as a three-wave mixing device, converting power between the signal (“s”), pump (“p”) and idler (“i”) ports. It is also provided with four linear inductances cross-linked to the junctions’ terminals, allowing an extension of the working frequency range.

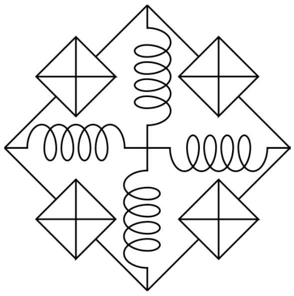

Figure 3.6: Schematics of the widely tunable ring modulator, made up of four Josephson junctions crossed with four linear inductances.

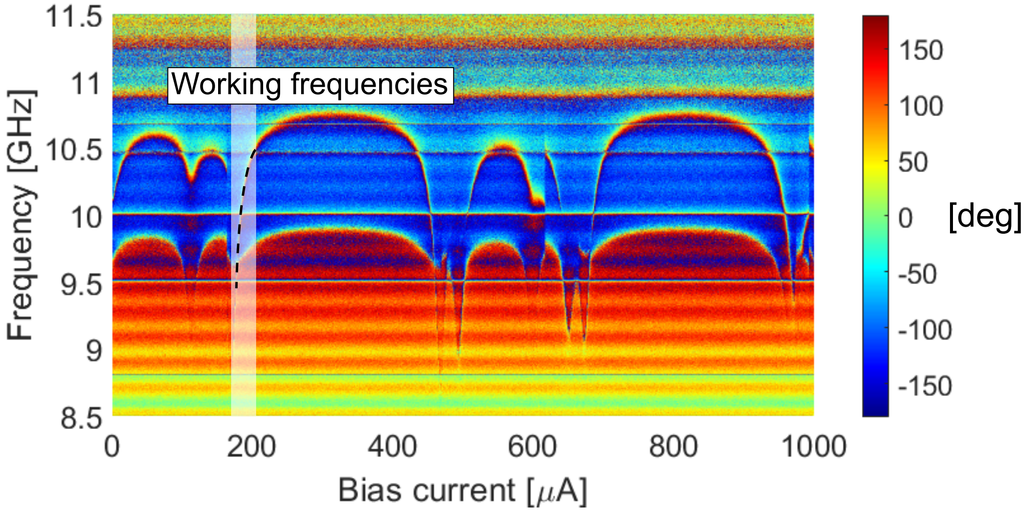

Figure 3.7: Phase-current plot of our JPA, obtained by varying the bias current of the superconducting coil below the device and measuring the phase of the S_{21} spectra. The measurements have been repeated with the external magnetic field on and show no difference. The intensity map is given in degrees, and the possible working points are highlighted in the plot.

The JPA is enclosed inside two shields, protecting it from the Earth magnetic field and external disturbances. To tune the frequencies of the signal, pump and idler modes, a bias field to the loop is provided thanks to a small superconducting coil positioned below the ring and biased with a current I_b. All the pieces are in thermal contact with the mixing chamber plate of the dilution refrigerator of our setup. The effect of I_b on the modes is summarized in a phase-current characteristic, as in the plot of Fig. 3.7. For every bias value, a transmission measurement (S_{21}) on the vertical frequency sweep is done, and the color scale indicates the phase of the S_{21} values in degrees. The possible working points, one of which is shown with the dashed curve, are the steep segments at the edges of the large lobes, where the derivative of the mode's resonance frequency is maximum, so that the pump drives the parametric amplification of the signal.

Preliminary tests were performed to characterize the JPA. By varying the pump amplitude and frequency and by applying a small bias magnetic field, the JPA tunability is between

10 and 10.5 GHz. After having verified the linear and saturation regimes of the JPA, its gain is measured by injecting in the test line a power level high enough to be read with the JPA off and such that it does not saturate with the JPA on. At the cavity frequency of 10.4018 GHz, we measure a gain $G_{JPA} = 18$ dB in a 10 MHz bandwidth. Finally, the noise temperature of the JPA is expected to be at the standard quantum limit of 0.5 K at this working frequency, including the contribution of 0.25 K from vacuum fluctuations.

3.2.3 Calibration

Before explaining the calibration procedure, in Table 3.1 the expected noise contributions from the system are grouped together. "Input noise" means that all noise contributions are

Table 3.1: Noise contributions estimated at the cavity resonance frequency. "Vacuum" is the contribution of quantum fluctuations of vacuum. The room-temperature HEMT (A2) contribution is negligible. "Cables" refers to rf attenuation of cables, with the only effect that of reducing the overall gain.

Source	Gain [dB]	Noise temp. [K]	Input noise [K]
Cavity	–	0.078	0.078
Vacuum	–	0.25	0.25
JPA	18	0.25	0.25
Cables	-3	–	–
HEMT (A1)	30	8	0.25
Total			0.83

referred to the amplification chain input, i.e. the JPA input. In this case, the HEMT contribution is obtained dividing its noise temperature by the linear gain of the JPA, to which the cables attenuation is subtracted:

$$T_{\text{input}}^{\text{HEMT}} = \frac{T_n^{\text{HEMT}}}{G_{JPA}^{\text{lin}} - A_{\text{cables}}} = \frac{T_n^{\text{HEMT}}}{10^{\left((G_{JPA}^{\text{dB}}-3)/10\right)}} = 0.25\,\text{K}\,.$$

The cavity contribution of 0.078 K is due to the thermal noise generated by its conductive walls at 250 mK (this value of the cavity temperature will be cleared in the next section) and it is calculated with the full Bose-Einstein distribution.

The calibration procedure allows to directly measure the total gain and noise temperature of the Readout line. The first step consists in measuring the attenuations of the rf lines in Fig. 3.5: *i)* the transmittivity K_{AR} of the Aux-Readout line is measured by decoupling the antenna D1 from the cavity, so that the power from Aux is reflected to Readout at the cavity input; *ii)* the antenna is then critically coupled to the mode and the transmittivity K_{AS} of the Aux-SO line is acquired; *iii)* with the antenna critically coupled it is also possible to measure the transmittivity K_{SR} of the SO-Readout line. The attenuation K_{SO} of the SO line

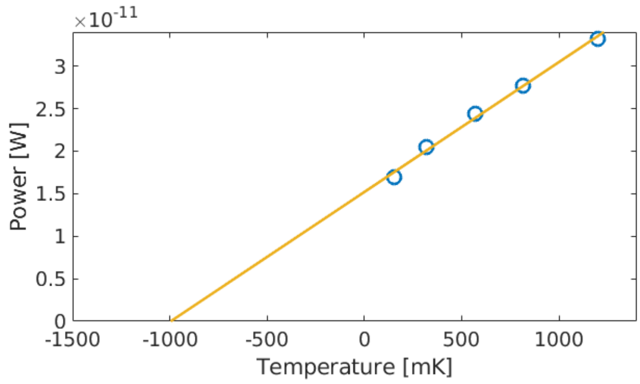

Figure 3.8: Calibration curve of the system gain and noise temperature, obtained by injecting known signals in the SO line. The power injected in the cavity through the antenna D2 is given in terms of an effective temperature proportional to A_{cal}.

can be obtained from a combination of the previous measurements, and in linear units it results $K_{SO} = \sqrt{K_{SR}K_{AS}/K_{AR}}$. Now that the SO line is calibrated, the second step consists in injecting a known signal from SO and reading the output from Readout to extract its gain and noise. The amplitude of the input signal at the antenna D2 is $A_{\mathrm{cal}} = K_{SO}\,A_{\mathrm{in}}$. Injecting increasingly large input signals A_{in} and detecting the output powers allows us to get the calibration curve, shown in Fig. 3.8. The x-axis values are given in terms of an effective temperature proportional to A_{cal}. Since the dependence of the output power on the input power is linear, the gain is the slope of the curve and the noise temperature is obtained from the intercept.

Finally, the system gain and noise temperature after calibration read

$$
\begin{aligned}
G &= 70.4\ \mathrm{dB}, \\
T_n &= \left(0.99 \pm 0.15_{\mathrm{cal}} \pm 0.04_{\mathrm{stab}}\right)\ \mathrm{K}.
\end{aligned}
\tag{3.12}
$$

The first error results from an uncertainty of 16% in the calibration scale due to a limited tunability of the coupling of antenna D1, that can be varied by an amount of 8 dB. The second error is attributed to temperature instability; in fact, during data-taking runs, the system had some uncontrolled temperature variations. However, the value of T_n, within the error, is in agreement with our estimate of 0.83 K obtained from the single contributions reported in Table 3.1.

3.2.4 Analysis and results

After setting the magnetic field to 8.1 T, we perform the axion search for a total time $\Delta t =$ 4203 s with an ADC sampling of 2 Ms/s, with the cavity tuned at a fixed frequency of $\nu_c = 10.4018$ GHz. We compute the average power spectrum with a fine frequency bin of 651 Hz, corresponding to 1/16th of the expected axion signal width [54]; the recorded

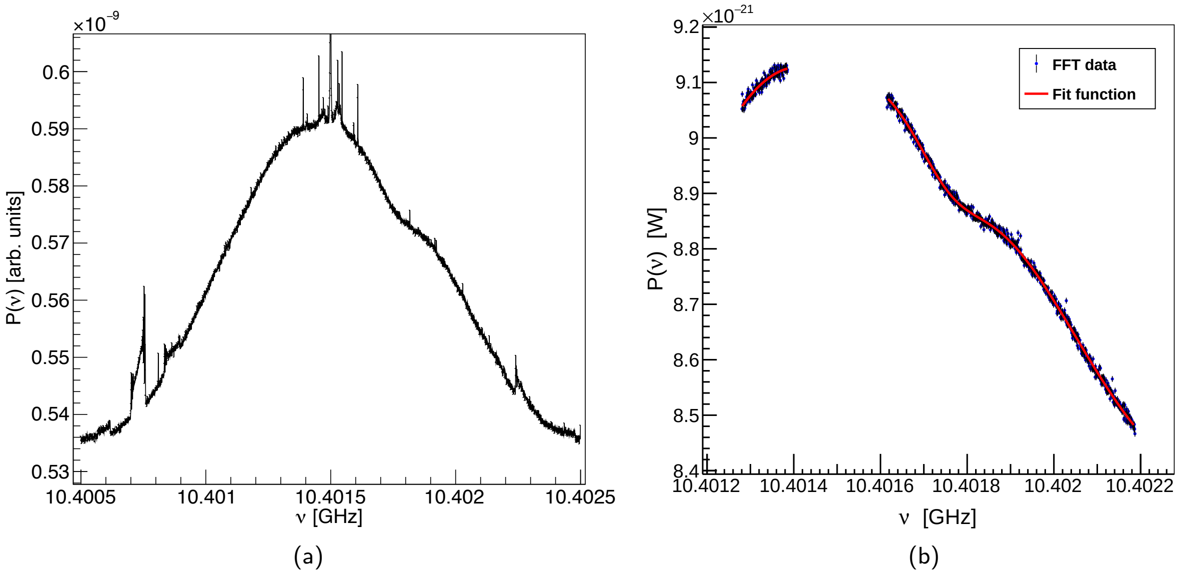

Figure 3.9: **a)** Recorded raw power spectrum in arbitrary units, before the noisy regions have been removed. **b)** Measured power spectrum after the quality cuts have been applied. The red line represents the model function used to obtain the residuals.

raw power spectrum after the average is shown in Fig. 3.9a. We then identify and remove IF noise bins, which have a width $\Delta\nu_{\mathrm{IF}} << \Delta\nu_{\mathrm{bin}}$. We exclude from our analysis a 200 kHz frequency region around the local oscillator frequency, $\nu_{lo} = 10.4015$ GHz, which is affected by $1/f$ and pickup noise, also appearing when running the setup with the magnet off. For the same reason we also exclude a single bin in the cavity region; this has an off-resonance counterpart, symmetric with respect to the LO after the down-conversion, where ν_{lo} is set to zero. Performing the ratio of the left half of the spectrum to the right half, the single bin and its counterpart perfectly cancel; thus it is considered a noise bin and is removed. This single bin and the 200 kHz region around LO are the only features removed from the spectrum. Finally, we consider only the region of the Lorentzian distribution of the cavity power spectrum with an expected power of at least 10% of the peak value. The resulting spectrum is shown in Fig. 3.9b.

In order to extract the residuals, we model the system composed of the cavity and the "Readout" line with an equivalent electrical circuit. All the calculations are explicited in Appendix A. Using the transmission-line formalism, we derive the following expression of the power spectrum:

$$P_n = G_{TOT}(\omega) k_B (\tilde{T}_1 + T_{A,tot}) \times \left(\frac{\tilde{T}_1}{T_{A,tot} + \tilde{T}_1} \frac{\tilde{T}_c/\tilde{T}_1 + (Q_L\delta)^2}{1 + (Q_L\delta)^2} + \frac{T_{A,tot}}{T_{A,tot} + \tilde{T}_1} \right). \tag{3.13}$$

Note that $T_{A,tot} = 0.50$ K is the sum of the noise temperatures of the JPA and HEMT (A1) amplifiers, as reported in Table 3.1. Here, $T_1 \sim 270$ mK is the effective temperature of the circulator on the "Aux" line, and T_c is the temperature of the cavity, which is left as a free parameter. Low temperatures require the use of the Bose-Einstein distribution, so instead of T_1 and T_c we use the noise temperatures $\tilde{T}_1$ and $\tilde{T}_c$; the tilde stands for

$$k_B \tilde{T} = \frac{h\nu_c}{\exp\left(h\nu_c/k_B T\right) - 1} + \frac{h\nu_c}{2},$$

including the contribution from vacuum fluctuations. Therefore, the first term in the big parentheses of eq. (3.13) represents the contribution of the circulator's Johnson noise reflected by the cavity and the thermal noise emitted by the cavity itself, while the second term is the added noise of amplifiers. Here, Q_L is the loaded quality factor, $\delta = (\nu/\nu_c - \nu_c/\nu)$, ν_c the cavity resonance frequency and $G_{TOT}(\omega)$ is the total gain function.

We fit the power spectrum by expressing $G_{TOT}(\omega)$ as 2nd and 4th order polynomials in the left and right branches of Fig. 3.9b, respectively. Given the large number of unknown parameters, we fix all known quantities to the best of our knowledge, taking into account measurement errors. The best fit is obtained for $\nu_c = 10.40176$ GHz and $Q_L = 35\,000$, in reasonable agreement with our measurements. When fixing the "Aux" circulator temperature to $T_1 = 273$ mK, we obtain a cavity temperature $T_c = 250$ mK, compatible with our expectations. The fit has $\chi^2/n = 1226/1032$ and is shown by the red line in Fig. 3.9b. Changing T_1 in an interval between 150 and 273 mK does not impact the quality of the fit and just reduces the cavity temperature down to about 100 mK in the former case.

Since the expected axion signal width is of about 10 kHz in the lab frame [12, 54, 58], with a bin width of 651 Hz a power excess is expected in about 16 consecutive bins. We normalize the residuals obtained in the fit procedure to the expected noise power $\sigma_{\text{Dicke}} = 5.38 \times 10^{-24}$ W derived from the Dicke radiometer formula [103] using the system temperature $T_n = 0.99$ K:

$$\sigma_{\text{Dicke}} = k_B T \sqrt{\Delta\nu/\Delta t}\,, \tag{3.14}$$

where Δt is the integration time. The distribution of the normalized residuals is shown in Fig. 3.10 together with the result of a Gaussian fit, showing a rms compatible with 1.

To claim a discovery candidate we require that power is in excess of 5σ from the noise spectrum, corresponding to some bins > 5 in the normalized residuals. Correcting for the look-elsewhere effect, the requirement would be to find excesses greater than [26]

$$Z = \Phi^{-1}\left(1 - 2.87 \times 10^{-7}/N_{\text{bin}}\right), \tag{3.15}$$

where Φ is the cumulative of the normal distribution and $N_{\text{bin}} = 1041$ is the number of data bins, corresponding to an effective number of $Z = 6.204$. We did not find any candidate, so we interpret our result as an exclusion test for the axion existence in this mass range. A maximum likelihood approach is used to compute the estimator $\hat{g}_{a\gamma\gamma}$ from the data, with the

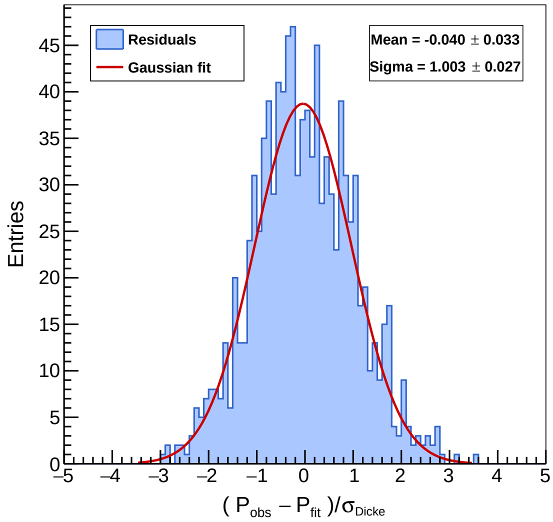

Figure 3.10: Distribution of the residuals normalized to the expected thermal noise, fit with a Gaussian function (red curve).

logarithmic likelihood

$$-2\ln\mathcal{L}(m_a, g^2_{a\gamma\gamma}) = \sum_{i=0}^{N_{\rm bin}} \frac{\left(R_i - S_i\left(m_a, g^2_{a\gamma\gamma}\right)\right)^2}{(\sigma^{\rm max}_{\rm Dicke})^2}\,, \tag{3.16}$$

where we have assumed Gaussian statistics. The index i runs over bins, R_i are the observed residuals, S_i are the model signals which are given by Eq. (3.9) multiplied by the full Standard Halo Model distribution of Eq. (1.35), and $\sigma^{\rm max}_{\rm Dicke} = 6.41\times10^{-24}$ W is the most conservative noise power, obtained with the maximum temperature allowed within its error, $T_n^{\rm max} = (0.99+0.15+0.04)$ K. Note that the rhs of Eq. (3.16) is a χ^2 distribution, thus the estimator $\hat{g}^2_{a\gamma\gamma}$ is evaluated by minimizing it:

$$\frac{\partial\chi^2}{\partial g^2_{a\gamma\gamma}} = 0 \qquad \Rightarrow \qquad \hat{g}^2_{a\gamma\gamma} = \frac{\sum_i R_i s_i}{\sum_i s_i^2}\,, \tag{3.17}$$

where $s_i \equiv S_i(g^2_{a\gamma\gamma} = 1)$. The error on the estimator is calculated as

$$\sigma_{\hat{g}^2_{a\gamma\gamma}} = \left(\frac{1}{2}\,\frac{\partial^2\chi^2}{(\partial g^2_{a\gamma\gamma})^2}\right)^{-1/2} = \frac{\sigma^{\rm max}_{\rm Dicke}}{\sqrt{\sum_i s_i^2}}. \tag{3.18}$$

The maximum likelihood procedure is repeated for each axion test mass, precisely $N_{\rm bin}$ times, resulting in a step size of 651 Hz. Finally, we calculate the limit to the axion-photon coupling with a single-sided 90% confidence level, power-constraining values of $\hat{g}^2_{a\gamma\gamma}$ as

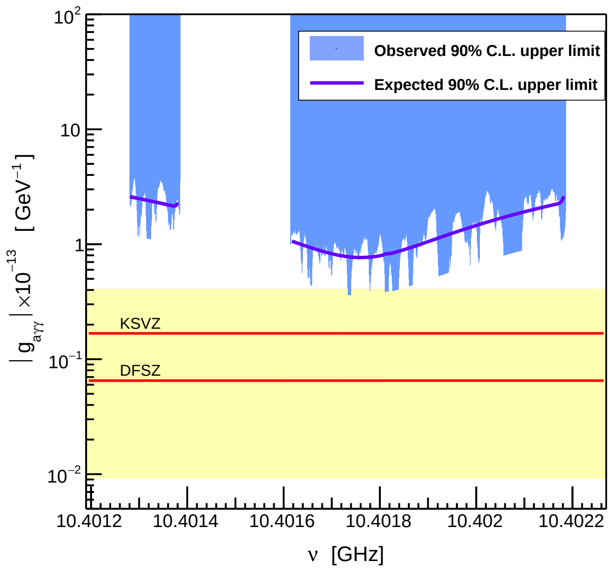

Figure 3.11: The 90% single-sided C.L. upper limit for the axion coupling constant $g_{a\gamma\gamma}$. Each point corresponds to a test axion mass in the analysis window. The solid curve represents the expected limit in the case of no signal. The yellow region indicates the QCD axion model band. We assume $\rho_a \sim 0.45$ GeV/cm^3.

in [104]. This avoids negative values of $\hat{g}^2_{a\gamma\gamma}$ to underfluctuate below -1σ and to underestimate the limit setting it by hand. The values are

$$g^{\mathrm{CL}}_{a\gamma\gamma} = \begin{cases} \sqrt{0.28\,\sigma_{\hat{g}^2_{a\gamma\gamma}}} & \text{if } \hat{g}^2_{a\gamma\gamma} < -1\sigma_{\hat{g}^2_{a\gamma\gamma}} \\ \sqrt{\hat{g}^2_{a\gamma\gamma} + 1.28\,\sigma_{\hat{g}^2_{a\gamma\gamma}}} & \text{otherwise} \end{cases} . \tag{3.19}$$

The limit as a function of the tested axion masses is reported in Fig. 3.11, shown with a colored area, together with a solid purple line showing the expected limit in the case of no signal. The reference upper limit of our search is the value at the maximum sensitivity (the minimum of the purple line of Fig. 3.11), $g^{\mathrm{CL}}_{a\gamma\gamma} < 0.766 \times 10^{-13}$ GeV^{-1} at 90% C.L.

In Fig. 3.12 the limit $g^{\mathrm{CL}}_{a\gamma\gamma}$ that we observed, in a mass window $\Delta m_a = 3.7$ neV centered at the mass $m_a = 43.0182$ μeV, is compared with those obtained in previous searches. The limit set on the axion-photon coupling is about a factor 2 from the QCD band. This demonstrates that, even at a frequency as large as 10 GHz, haloscopes can reach the sensitivity to observe QCD axions when exploiting quantum devices, like a Josephson parametric amplifier with noise at the standard quantum limit in this case. The total noise in our setup, estimated as twice the SQL, can be further reduced by improving the thermalization of the resonant cavity and the line filtering, and by reducing the noise contribution from the HEMT. The implemented analysis technique relies on a simple maximum likelihood method, but a more

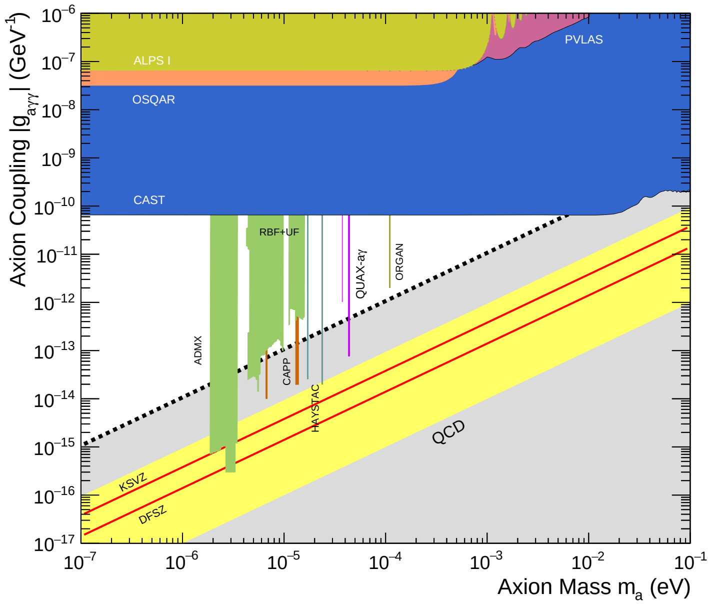

Figure 3.12: Aggregate plot of the limits on $g_{a\gamma\gamma}$ obtained from the main axion search experiments. The two limits obtained by the QUAX Collaboration are highlighted in purple. The gray area identifies the region where axions could be found, with the yellow band and the two solid red lines identifying the coupling predicted by the KSVZ and DFSZ models and its uncertainty.

thorough procedure can be implemented, as for example in [53, 60, 64, 105].

Finally, it is important to note that while the sensitivity to the KSVZ line can be achieved running the setup at milliKelvin temperatures with a 10 T magnetic field and a JPA at the standard quantum limit, linear amplifiers become a technical limitation when trying to reach the DFSZ line. This is a reason to motivate the implementation of a single photon detector, not subject to the SQL, which is argument of the following Chapters.

CHAPTER 4

The LNF haloscope

The QUAX measurements reported in Chap. 3 were carried out with the Legnaro haloscopes. In this Chapter, a new haloscope under construction at LNF (Laboratori Nazionali di Frascati) is presented, which will be used as a second haloscope of the QUAX-aγ experiment. The dilution refrigerator is already available and has been exploited for a series of measurements, as the ones described in Chap. 6. The cryostat is being constantly characterized, monitored and upgraded. My activities concerning the LNF haloscope consisted mainly in the characterization of the cryostat rf environment and in setting up the related instrumentation.

An axion haloscope is a cryogenic, tunable high-Q microwave cavity immersed in a strong magnetic field and coupled to a low-noise receiver. Before describing the components of the LNF future haloscope, as an introduction I will talk about the noise sources present in a haloscope to give an idea of the various noise contributions of the devices (such as amplifiers) to the figure of merit of the axion search.

4.1 Noise in a haloscope

It is important to appreciate that an axion signal in a haloscope is identical to a noise signal: a fluctuation in the acquired power spectrum from a resonant cavity. However, this does not put an end to all the research, as statistical techniques are involved to constrain the presence of an axion signal. Noise contributions in a haloscope come from the Johnson (thermal) noise and quantum noise, which in turn divide in vacuum fluctuations and noise added by amplifiers.

Johnson noise, first measured by Johnson [106] and then explained by Nyquist [107], is associated to the resistance of the metallic cavity walls. In fact, it is caused by the irregular thermal motion of electrons in an imperfect conductor; this generates fluctuating electromagnetic fields in the resonant cavity. Dicke [103] has shown that the Johnson noise of a resistive load is equivalent to the voltage noise on an antenna receiving blackbody radiation at the same load temperature. Thus, Johnson noise can be thought of as arising form a blackbody photon gas inside the cavity, in equilibrium with its walls.

The root mean square of the voltage noise of a resistance R at temperature T in the Rayleigh-Jeans approximation is given by [108]

$$\bar{V}_n = \sqrt{4k_B T_{\text{sys}} \Delta\nu R}, \tag{4.1}$$

where $\Delta\nu$ is the bandwidth of the system and T_{sys} is the *system noise temperature*, comprising the physical temperature T and the added noise temperature (more details on T_{sys} are given in a while). Considering an output load matched to the resistance R, on which maximum power is delivered, the noise power can be written as

$$P_n = \left(\frac{\bar{V}_n}{2R}\right)^2 R = k_B T_{\text{sys}} \Delta\nu\,. \tag{4.2}$$

To give a quantitative example of the thermal noise, consider a room temperature of 300 K and a bandwidth equal to the axion linewidth $\Delta\nu_a \sim 10$ kHz, the noise power results in $P_n \sim 4 \times 10^{-17}$ W, almost a factor 10^7 greater than the KSVZ model expected signal power. That's why cryogenic temperatures are mandatory! But even if we put a 10 mK temperature in equation (4.2), P_n would overcome P_{sig} by order 10^3.

The crucial point is that the figure of merit in a haloscope is the **signal-to-noise ratio** (SNR):

$$SNR = \frac{P_{\text{sig}}}{\delta P_n}, \tag{4.3}$$

where δP_n is the uncertainty in the noise power. The motivation is based on the argument that if we were able to measure the noise power with no uncertainty, any power excess would be attributed to an axion signal or other new physics. To write an expression for δP_n, a distinction between coherent and incoherent receivers has to be done.

A coherent, or linear, receiver returns a linear function of the input signal, preserving information of the frequency and phase content in the output, while in an incoherent, or bolometric, receiver the output is proportional to the input average intensity, losing the phase information. Single photon detectors are included in the incoherent category of receivers. For the present arguments, however, only linear receivers are considered.

The distribution of the noise voltage amplitude for the Johnson noise within a bandwidth $\Delta\nu$ is assumed to be Gaussian, so that δP_n is proportional to the variance of the voltage distribution, resulting in

$$\delta P_n = \sqrt{\frac{2}{n-1}} k_B T_{\text{sys}} \Delta\nu \,, \tag{4.4}$$

with n the number of the samples of the distribution. This is taken large enough so as to approximate $n - 1 \approx n$. Now, the Nyquist-Shannon sampling theorem [109] can be exploited; this guarantees that a signal is completely represented with an acquisition at a sampling rate n/t equal to twice the signal bandwidth: $n = 2\Delta\nu\, t$, where t is the total acquisition time. Substituting this expression for the independent samples in Eq. (4.4) gives

$$\delta P_n = k_B T_{\text{sys}} \sqrt{\frac{\Delta\nu}{t}} \,. \tag{4.5}$$

This is again the Dicke equation encountered in Chap. 3 for the uncertainty of the noise power. The signal-to-noise expression is then immediately found:

$$SNR = \frac{P_{\text{sig}}}{k_B T_{\text{sys}}} \sqrt{\frac{t}{\Delta\nu}} \,, \tag{4.6}$$

often referred to as the Dicke radiometer equation. This is also useful to calculate the required acquisition run time of a haloscope to reach an *a priori* specified signal-to-noise ratio to detect or exclude an axion signal.

Note that all the equations starting from (4.1) were obtained in the Rayleigh-Jeans limit $k_B T \gg h\nu$. At very high frequencies or low temperatures, which is the case for our haloscope, the right temperature term must be considered and the equations (especially the Dicke relation) modified, as is done in the introduction to Chap. 5 and just below for quantum noise considerations.

Now, for a haloscope coupled to a linear receiver, the full expression for T_{sys} at low temperatures can be written as

$$k_B T_{\text{sys}} = h\nu N_{\text{sys}} = h\nu \left(\frac{1}{e^{h\nu/k_B T} - 1} + \frac{1}{2} + N_A \right) , \tag{4.7}$$

where N_{sys} represents the total number of noise quanta. The first term on the right hand side is a Bose-Einstein term corresponding to the number of blackbody photons in the cavity, so that it expresses thermal Johnson noise in the Dicke correspondence. $h\nu/2$ is a quantum noise term associated to the zero-point fluctuations of the same blackbody gas, while the last additive term N_A is the noise added by the receiver, referred to its input. Eq. (4.7) shows that for high enough temperatures, the expression reduces to $T_{\text{sys}} \approx T + T_A$, where $T_A = (h\nu/k_B)N_A$ is the effective noise temperature associated to the receiver, while in the low temperature limit $k_B T \ll h\nu$ it is clear that the thermal contribution is suppressed and quantum noise terms dominate.

The justification of the second term on the right hand side of Eq. (4.7) is simple. A voltage signal, as the one extracted from the cavity with an antenna, can be written in the quadrature representation, a basis where the quadratures are the amplitudes of two 90-degree phase-shifted terms. When quantizing the fields, the quadratures are promoted to operators, but they neither commute with the Hamiltonian nor with each other, giving rise to half a quantum noise.

The last term N_A has a quantum nature as well. A coherent receiver is constituted by a linear amplifier with gain $G \gg 1$, and this requires energy coming from some power line. An amplifier then couples the noise from that power line into the output signal. The minimum amount of noise quanta added by a linear receiver is given by the Haus-Caves theorem [110, 111]:

$$N_A \geq 1/2\,, \tag{4.8}$$

valid for "phase-insensitive" linear amplifiers, which apply the same gain to both quadratures. This is because a phase-insensitive linear amplifier measures both the quadratures, but, again, they do not commute with each other. For a JPA, the added noise comes from vacuum fluctuations at both the signal and idler frequencies.

With the definition of the input-referred noise N_A of a linear receiver as the physical added noise divided by the gain G, the noise coming from an amplification chain composed of i linear amplifiers is easy to calculate. In fact, if the amplifiers have gain G_i and added noise N_{A_i}, the input-referred noise of the whole series is

$$N_A = N_{A1} + \frac{N_{A2}}{G_1} + \frac{N_{A3}}{G_1 G_2} + \dots\,, \tag{4.9}$$

thus, in the realization of a haloscope, it is important to have a low-noise and high-gain preamplifier, as it determines the noise performance of the amplification chain.

Summarizing, the two quantum contributions to the noise in a phase-insensitive linear amplifier are due to vacuum fluctuations and to the Haus-Caves theorem, implying the *standard quantum limit* (SQL):

$$N_{\text{sys}} \geq 1\,. \tag{4.10}$$

This may be expressed in temperature units as

$$T_{\text{SQL}} = \frac{h\nu}{k_B}\,, \tag{4.11}$$

where $N_{\text{sys}} = 1$ is implicit. Numerically, $T_{\text{SQL}} \simeq 480$ mK for 10 GHz frequency photons. Below this value, once fixed the operating frequency, trying to lower the physical temperature is useless, as it has no effect on the signal-to-noise ratio. Here stands the importance of the realization of a single-photon counter: measuring a number of photons instead of two quadratures, it is not subject to the SQL, thus having profound implications on a haloscope

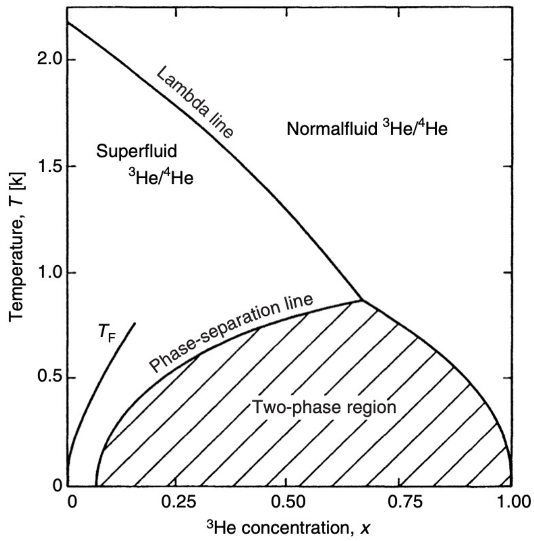

Figure 4.1: (T, x)-plane of a mixture of ^{3}He-^{4}He, where $x = n_3/(n_3 + n_4)$ is the ^{3}He concentration. Taken from [113].

search.

4.2 Cryogenics

Based on what I said in the previous Section, the need of a cryogenic environment is self-explaining, as it leads to the suppression of thermal noise, and devices that give low-noise amplification require cryogenic temperatures to work.

To cool our environment, we use a Leiden Cryogenics CF-CS110-1000 ^{3}He-^{4}He dilution refrigerator (DR). The advantage of dilution refrigerators based on mixtures of ^{3}He and ^{4}He over other cooling methods is that they are able not only to reach very low temperatures, but to maintain such temperatures for months [112].

4.2.1 Principles of DR operation

To understand the operation of a DR, one can start from the description of ^{3}He-^{4}He mixtures. ^{3}He and ^{4}He have different entropies, as they follow different statistics. The latter is a Bose fluid, and below 2.17 K it undergoes a transition to a superfluid state; at typical refrigerator temperatures below few hundreds of milliKelvins it can be considered at the ground state, having little entropy. ^{3}He, on the other hand, is a Fermi fluid and has large entropy. When mixed to the superfluid ^{4}He, ^{3}He can flow through it with little impedance. Fig. 4.1 shows the phase diagram of the mixture: on the left of the λ line the ^{3}He is immersed in ^{4}He in its superfluid phase, while on the right the fluids are normal. If the temperature is lowered below about 0.7 K (the three-phase point in Fig. 4.1), the two isotopes start to spontaneously separate at temperatures depending on the concentration. Below the separation line ^{3}He floats on top of ^{4}He like oil on water, as ^{3}He has a lower density than ^{4}He. When the temperature is further lowered, the ^{3}He-rich phase, called *concentrated phase*, approaches purity, while the ^{4}He-rich phase reaches a ^{3}He concentration of $x = 0.066$, thus being called *diluted phase*. The reason lies in the quantum nature of the fluids, but the fact that ^{3}He always dissolves in ^{4}He with a minimum concentration is crucial for the success of dilution refrigerators. In fact, forcing a flux of ^{3}He isotopes from the concentrated phase to the diluted one is analogous to an evaporation process, causing the cooling of the ^{3}He pure phase. The limiting concentration of $x = 0.066$ assures that this diffusive process is always present at any temperature.

The three main parts of a dilution refrigerator are the mixing chamber (MC), the still and the heat exchangers. A schematic of a dilution refrigerator unit is given in Fig. 4.2, where all the main parts and the workflow are indicated. To describe the refrigerator operation, assume that it is already running at base temperature. Starting from the mixing chamber: this is the coldest stage in the process and it contains the pure ^{3}He phase on top of the dilute phase of ^{4}He contaminated with 6.6% of ^{3}He. The dilute phase in the MC is connected with an upward pipe to the still, where a heater is switched on. Therefore, the still volume is partially filled with liquid ^{3}He and mainly vapor ^{3}He, which is removed by vacuum pumps. This causes a gradient in the ^{3}He concentration in the dilute phase of the MC. Therefore, to maintain an equilibrium, the pure ^{3}He in the MC crosses the phase boundary in a diffusive motion downwards the dilute phase. This is an endothermic process, thus subtracting heat from the external environment, allowing to cool the whole system.

The circulation is finally completed when the vapor ^{3}He removed from the still is returned to the pure phase of the mixing chamber. The gas is first condensed again, and this can happen in two ways, that distinguish between *wet* and *dry* dilution refrigerators, depending on the presence or the absence of liquid ^{4}He in the cryostat. In the former, ^{3}He gas is first thermalized at 4 K thanks to a liquid ^{4}He bath, then it is cooled down to about 1.6 K in a 1 K pot, which is a container where the liquid ^{4}He is being pumped. Pressures of the order of 0.1 mbar are sufficient to liquefy ^{3}He at that temperature. In a dry cryostat, the returning ^{3}He gas is thermalized at about 4 K thanks to a pulse tube, so that liquefaction requires higher pressures, say $2 \div 3$ bar. The liquid ^{3}He is cooled further thanks to the heat exchangers before reaching the MC.

Much more details on dilution refrigeration can be found in many textbooks on low-temperature techniques, as in [114] or in the more recent [112].

4.2.2 Leiden Cryogenics CF-CS110-1000

The LNF dilution refrigerator is schematized in Fig. 4.3, while in Fig. 4.4 all the main parts of the refrigerator are indicated in detail, including the thermalization plates with their tem-

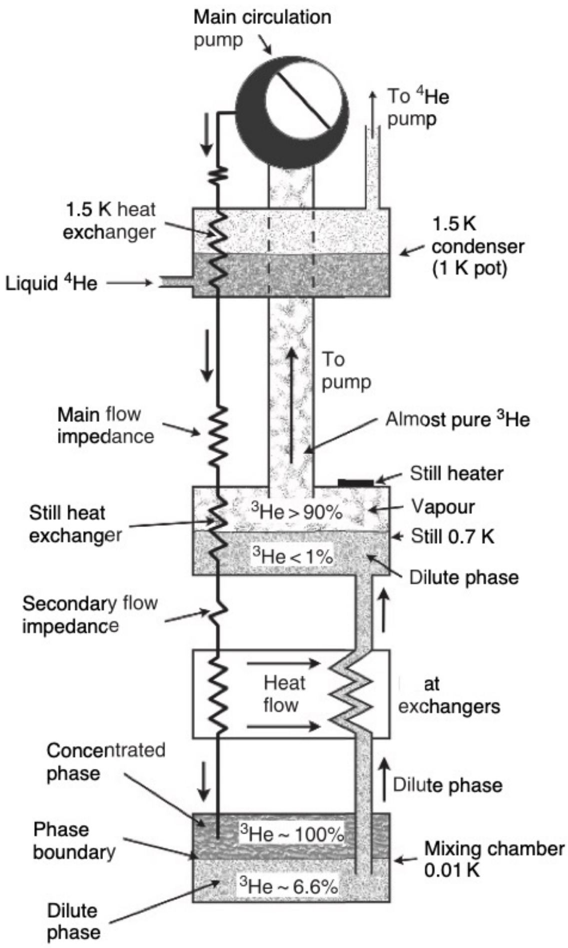

Figure 4.2: Schematics of a dilution refrigerator unit. Here the 1 K pot is present, so this is a wet dilution refrigerator. Image taken from [112].

peratures during regular operation.

The LNF haloscope is a dry dilution refrigerator. As a precooling operation, we use liquid Nitrogen to bring the temperature from 300 K to 77 K. The liquid Nitrogen flows in the LN pipes indicated in Fig. 4.4, in thermal contact with each plate. Then, a pulse tube, which operates compression and decompression cycles to the ^{4}He gas, is switched on and brings the temperature down to about 4 K. Finally, circulation of the ^{3}He-^{4}He mixture is activated and the system is cooled down to about 10 mK in the coldest plate as described in the previous section.

As explained in Sec. 4.2.1, the mixing chamber determines the coldest stage of the dilution process. Thus, the samples are mounted in the last plate (10 mK plate in Fig. 4.4), where the MC is thermally anchored. The coldest stable temperature we measured on the 10 mK plate in the absence of any sample is $T_{\text{base}} = 8$ mK. The MC is a stainless steel cylindrical container closed with a copper cap on the bottom side, with a diameter of about 120 mm. The still plate is usually at about 0.8 K, and this is an optimal temperature for the operation of our

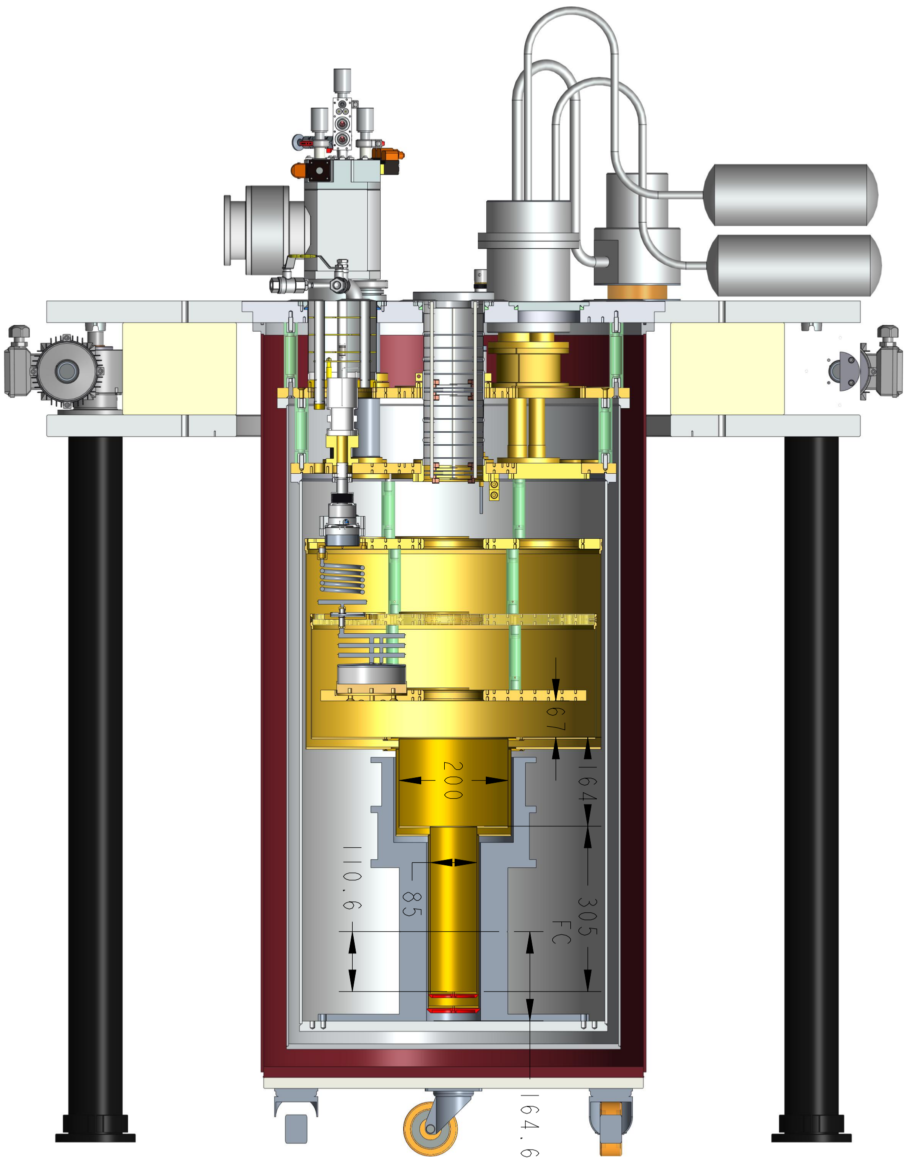

Figure 4.3: Schematics of the Leiden Cryogenics CF-CS110-1000 dilution refrigerator showing mechanical details. At the bottom, the magnet with its radiation shields is included. The gas handling system is not shown. Leiden Cryogenics has given consent to publish the picture.

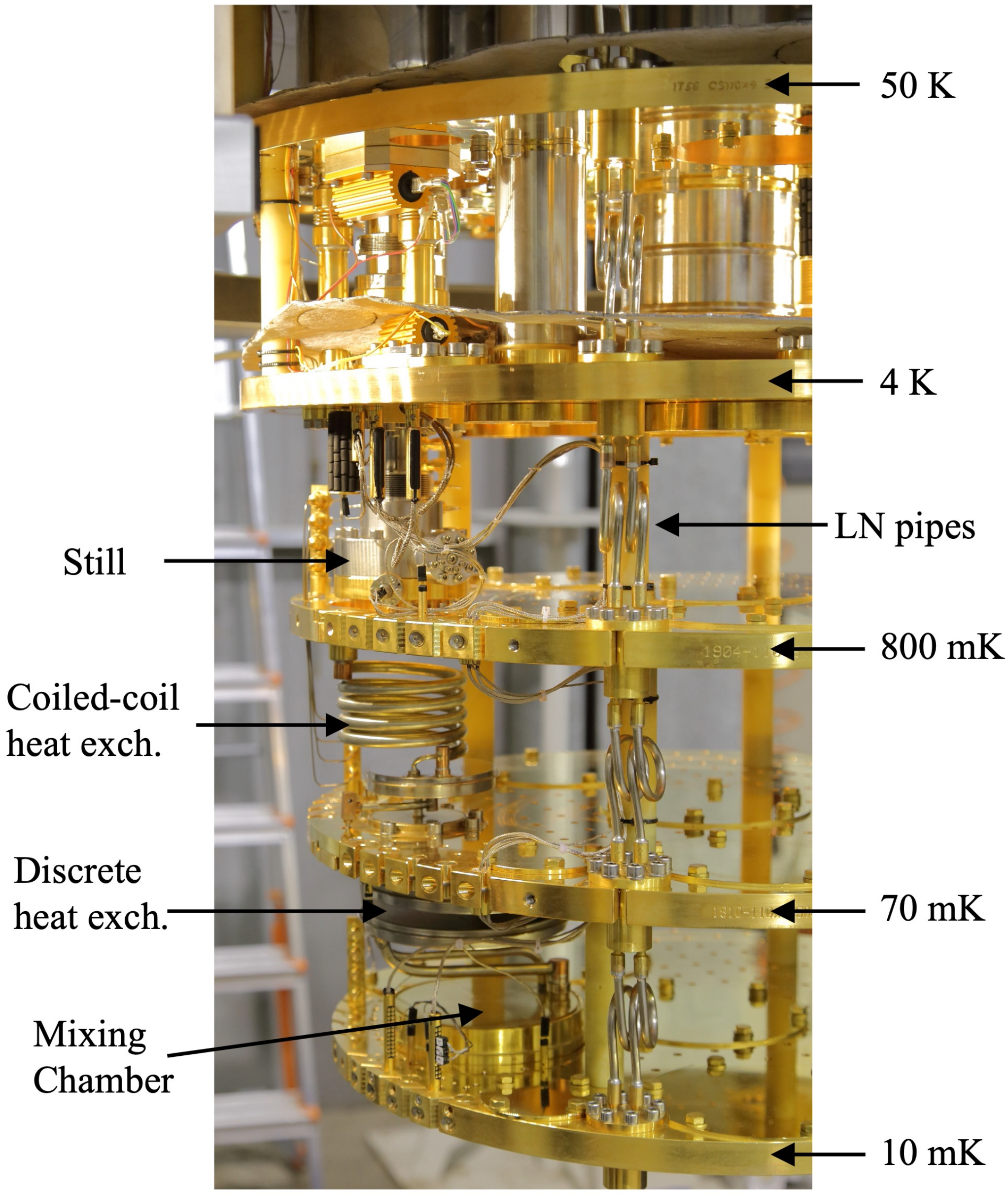

Figure 4.4: Detail of the Leiden Cryogenics CF-CS110-1000 dilution refrigerator, showing the plate temperatures of all the thermalization stages. The main parts where the dilution process happens are also indicated: the mixing chamber, the still and the continuous and discrete heat exchangers. LN refers to liquid Nitrogen.

refrigerator. In fact, due to the parasitic heat input on the 0.8 K plate, the still does not need to be heated, although being provided with an internal heater. The 4 K plate is stabilized at this temperature thanks to the contact with the pulse tube.

The thermometry is almost equally distributed in all thermalization stages. The 50 K plate is provided with a platinum resistive thermometer, while on all the other plates ruthenium oxide (RuO_2) thermometers are mounted. Additionally, a CMN[1] thermometer based on electronic paramagnets is also used at very low temperatures, on the 10 mK plate, having a minimum detectable temperature of 2 mK [115].

The theoretical cooling power of a dilution refrigerator depends on the molar flow rate of ^{3}He atoms from the pure to the diluted phase in the mixing chamber, and quadratically on the temperature [115]:

$$\dot{Q} = 84\, \dot{n}_3 T^2 \quad [W]\,. \tag{4.12}$$

It might seem that the optimal operation of a DR is obtained with the highest possible circulation rate, but the minimum base temperature has to be considered. This results from the balance of heat transfer to heat loads and/or inefficiencies in heat exchange and the cooling power. Thus, low circulation rates imply a low cooling power, with the result that background heat loads raise the temperature; at high circulation rates, the returning helium has not enough time to adequately cool in the heat exchangers. An optimum circulation rate thus exists in each DR.

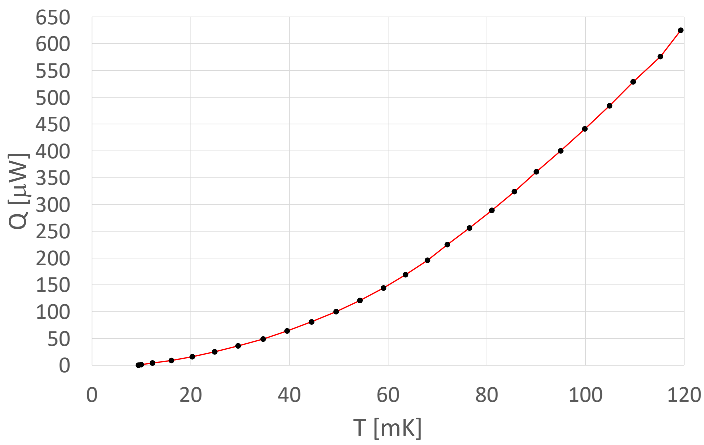

Figure 4.5: Cooling power $\dot{Q}$ of the Leiden Cryogenics CF-CS110-1000 as a function of temperature.

The cooling power can be measured by injecting a known amount of electrical power to the mixing chamber, waiting for equilibrium and recording the new temperature reached. Fig. 4.5 shows this plot for our dilution refrigerator as a function of temperature. From the characterization, the cooling power of our DR is about 450 μW at a temperature of 100 mK, and about 1 μW at 10 mK. A new vacuum pump has been recently mounted, which should

[1]CMN is a paramagnetic salt made with cerium ions, magnesium and nitrogen oxide.

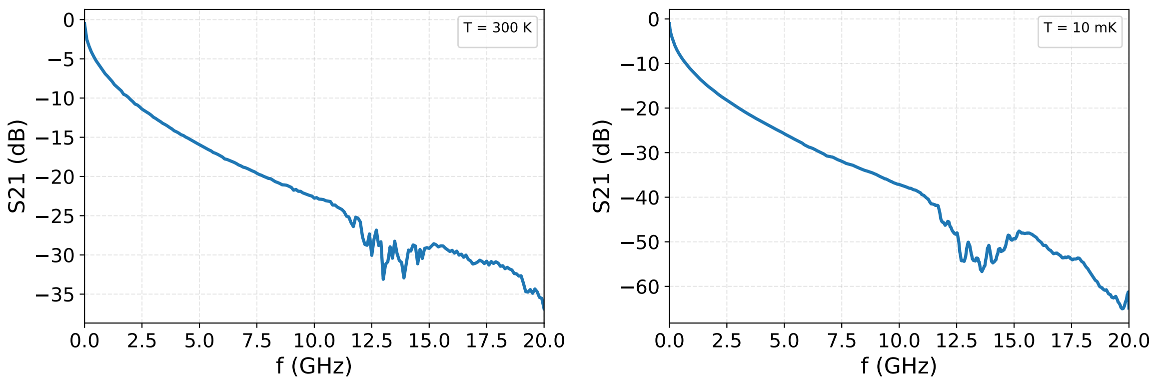

Figure 4.6: *Left*) Attenuation of Line 1 at 300 K, including the contribution of measurement cables. *Right*) Attenuation of Line 1 and Line 2 at temperatures down to 10 mK, including the contribution of measurement cables.

bring the cooling power up to 750 μW at 100 mK.

4.3 Instrumentation

4.3.1 Rf wiring and instrumentation

For testing samples with microwave radiation, the cryostat is provided with four high-attenuating rf lines, from 300 K to the 10 mK stage, used as inputs, and one low-attenuation rf line used as output; the latter will be described in Sec. 4.3.2. The rf wires are thermalized in each plate of the fridge (Fig. 4.4) with columns anchored to the plates. The wires are coaxial cables made of BeCu-Ag-CuNi and we use SMA connectors. Usually, power attenuators are mounted along the input wires to reduce the amount of thermal power coming from the 300 K environment.

Rf lines have to be calibrated to know the input power delivered to a device and the extracted output power, including the gain factor of the amplifiers. Since the lines' setup changes each time we cool the cryostat for a different data taking, it will be described in detail when the time comes (Chap. 6). An example of the attenuation of the rf lines is given in Fig. 4.6, where the measurements are done at $T = 300$ K for one line (on the left) and at $T = 10$ mK for two lines connected together (on the right). The attenuations are measured as S_{21} scattering parameters with a vector network analyzer (VNA). The plots include the measurement cables from the VNA to the cryostat and back, that give additional attenuation. The curves follow the expected attenuation behavior of lossy transmission lines (apart from a distortion between 11 and 15 GHz probably due to very tight bendings of the wires in the cryostat). In fact, the solutions of the propagating waves on a transmission line are of the form $V(x) = V_0^+ e^{-\gamma x} + V_0^- e^{\gamma x}$, where the first term represents wave propagation in the $+x$ direction and the second term in the $-x$ direction. γ is a complex propagation constant, and the attenuation is enclosed in its real part, which depends on the resistance of the transmission line. Thus, besides an oscillating term $e^{j\Im(\gamma)x}$, waves undergo attenuation as $\sim e^{-\Re(\gamma)x}$.

Upon subtracting the contribution of the measurement cables, the four rf lines have total attenuations between 16.5 and 18 dB at 10 GHz, at room temperature.

Comparing the two data sets of Fig. 4.6, the difference due to the temperature, although this is difficult to calculate since pieces of wire are at different temperature stages, is small, about 1 or 2 dB at a frequency of 10 GHz.

The instruments we use for rf measurements are a VNA, a signal generator and a spectrum analyzer. The VNA is an Agilent E5071C from 300 kHz to 20 GHz and has two ports. It measures scattering parameters S_{ij} of a two-port network by reading the reflected wave from the network with respect to the incident wave, $S_{ij} = V_i^- / V_j^+$ [108]. The signal generator is a Rohde&Schwarz SMA100B from 8 kHz to 20 GHz, with one channel available. We use it as a source oscillator in continuous wave mode or in pulsed mode, as for the characterization described in Chap. 6. The digital spectrum analyzer is a Signal Hound SM200B from 100 kHz to 20 GHz; it measures the power spectrum of the input signal in absolute units (dBm).

Other devices available and necessary for setups are attenuators, splitters, an rf switch, circulators, bias tees and a directional coupler.

4.3.2 Amplification chain

Although the topic of the thesis is the development of a single photon detector as a low-noise receiver, this section is on the characterization of the already available linear amplifiers that will be part of the LNF haloscope. The two commercially available microwave amplifiers are a cryogenic HEMT and a room-temperature FET, and are both field-effect transistor amplifiers. They are shown in Fig. 4.7.

The HEMT is a model LNF-LNC6_20C s/n 1403Z from Low Noise Factory and is installed

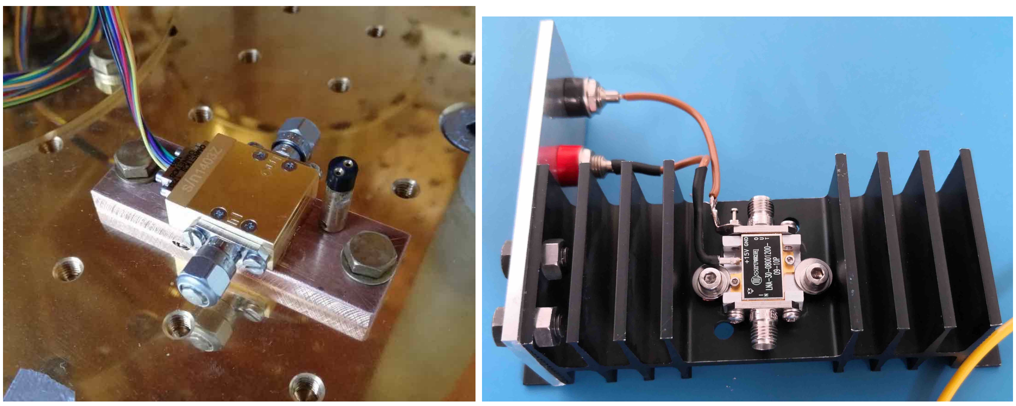

Figure 4.7: *Left*) Cryogenic HEMT amplifier attached to the 4 K plate. *Right*) Room-temperature FET amplifier, mounted on a radiator.

on the 4 K plate. Before using it in the receiver chain, it has been tested to verify the nominal values given in the datasheet, at both cryogenic and room temperature. The main measured features are gain, compression point and noise temperature. The gain is measured as an S_{21} parameter with a frequency sweep from the VNA, and results in 30 dB over a large bandwidth, between 4 and 20 GHz, consistent with the nominal value. The 1 dB compression point defines the saturation of the amplifier, and is defined as the input power value at which the gain is decreased by 1 dB with respect to the linear regime, where the gain is constant. The 1 dB compression point is measured with a power sweep of the VNA in continuous wave mode, at different frequencies. As a reference, the HEMT compression point at 10 GHz is approximately -27.5 dBm. Finally, the measured noise temperature differs a bit from the nominal value of 3 K added noise, given at 10 GHz when the temperature is 4 K. Acquiring the power spectrum with the spectrum analyzer, we estimate an added noise temperature of about $T_n^{\mathrm{HEMT}} \approx 8.4$ K (see 6.2.1), assuming the superconducting rf wiring is lossless and matched to the amplifier.

The FET is a model LNA-30-08001200-09-10P from Narda-Miteq and is put at 300 K on the outside of the cryostat. The gain has been verified only between 8 and 12 GHz, resulting in 30 dB. The 1 dB compression point at 10 GHz has been found to be about -16.5 dBm.

The tests are also repeated with the two amplifiers in series. Note that in this configuration, the noise temperature of the FET amplifier (with nominal value of about 66 K) does not contribute significantly to the total noise temperature of the receiver chain. In fact, referring it to the HEMT input, the contribution should be $T_n^{\mathrm{FET}} = 66\ \mathrm{K}/1000 = 66$ mK, where 1000 is the HEMT gain in linear units, thus being small compared to the HEMT noise.

The HEMT and FET amplifiers are put in series on an rf line used exclusively as readout line. Since the four original lines are very lossy, this is a fifth custom line. To minimize loss contributions, the fifth rf line pieces between the 10 mK stage and the still plate are constituted of NbTi-PTFE-NbTi coaxial cables, which remain superconducting under about 10 K. Currently, therefore, the output line is made up of a superconducting cable between 10 mK and the still plate, a normal metal cable from the latter to the 4 K stage, the HEMT, a normal metal cable for the remaining route from 4 K to 300 K, a commercial room-temperature cable to the FET, and another commercial room-temperature cable from the FET to the VNA.

Although only semiconductor-based amplifiers are now available at LNF, to reach the QUAX experiment goal by 2025 amplification based on quantum technologies is foreseen.

4.4 Magnet and resonant cavity

The magnet that will be mounted in the LNF haloscope, manufactured by American Magnetics Inc., has been delivered while this thesis is being written, and is shown in Fig. 4.8. Its dimensions are 486 mm height and 100 mm of cold bore diameter. The maximum current in

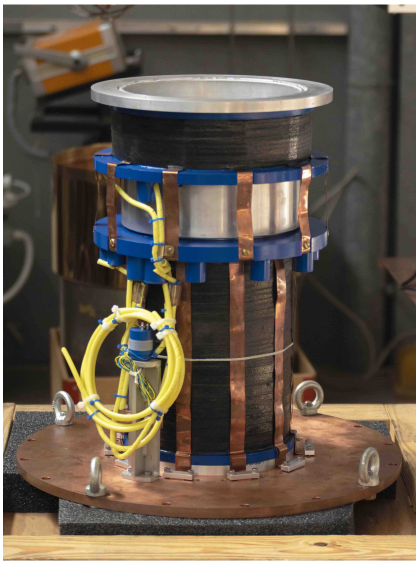

Figure 4.8: 9 T magnet to be mounted in the LNF haloscope. The main coil (in correspondence of the cold bore volume) and the countercoil (in the upper part of the structure) are covered with a black tape. The lower copper flange will be attached to the 4 K environment.

the coils is of about 90 A, supplying energy for a 9 T magnetic field at the magnetic center. The field uniformity is expected to be of the order of $\pm 0.1\%$ in a sphere of 1 cm radius around the center, and the field is expected to be reduced to less than 200 gauss at 33 cm from the magnetic center on the z axis. Radially, the field should decade to 50 gauss at about 100 cm.

As shown in the schematics of Fig. 4.3, the magnet will be anchored to the 4 K radiation shield, thus thermalized at the pulse tube temperature. The magnet coils are made of NbTi, thus being superconductive at 4 K. The magnet is also provided with a superconducting switch to work in persistent mode, where the field is maintained without requiring external power to be supplied.

Above the cold bore volume, a second superconducting set of coils is present, oppositely oriented with respect to the main coils, to reduce the field to less than 50 gauss, thus providing a small volume where devices requiring a zero magnetic field can be housed. At the moment, magnetic shields are not available, but shielding this zero-field region is foreseen. In the meanwhile, the samples will be temporarily housed in a Pb case.

Although the final LNF haloscope operation contemplates a multicavity scheme, as will be mentioned in the conclusive chapter (Chap. 7), in the immediate future a data run with a single tunable resonant cavity is planned. Here I give some details on the design and simulation of the cavity.

The microwave cavity is a cylindrical OFHC copper cavity, with height 246 mm and inner radius 13.51 mm, thus having a total volume of 0.141 liters. The body is divided into two semi-cylinders that will be sealed with screws; in this way, additional endcaps that would

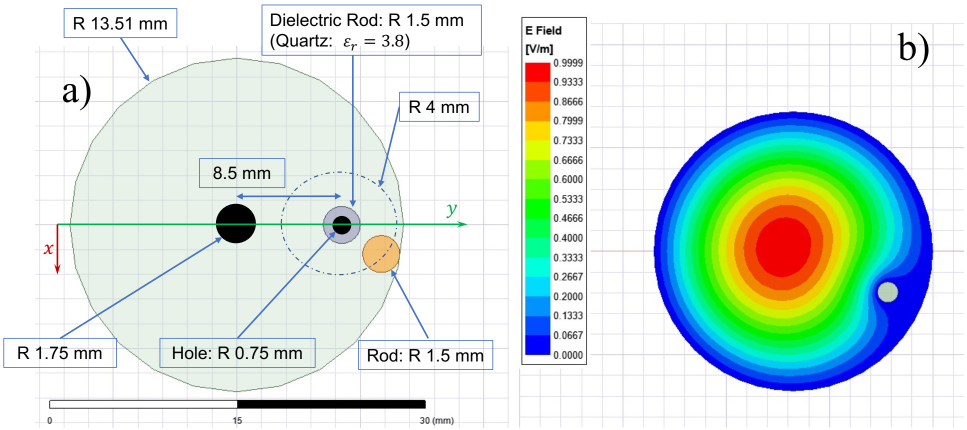

Figure 4.9: **a)** Top view of the designed cavity, with all the dimensions shown. The scheme refers to the tuning system with a metallic rod (in orange) pivoting around a dielectric axle (grey). **b)** Top view of the simulated electric field profile of the $TM010$ mode with a single tuning rod.

interrupt the flow of the rf currents causing losses are not necessary. At the top and bottom of the cavity, the holes for the input and readout antennas are put at the center of the endcaps. The resonant frequency of the $TM010$ mode is of the order of 8.5 GHz, but precise frequency and quality factor values depend on the tuning, which is described in a while.

Two possible tuning scenarios have been designed. In the first one, a copper tuning rod with 1.5 mm radius is used for frequency tuning, pivoting around an off-axis dielectric axle. The rod would be attached to the axle with two horizontal bars made of a low-loss dielectric (as alumina) or copper. This scheme is shown in Fig. 4.9a), together with the cavity and rods dimensions. The dielectric axle is a tube of inner radius 0.75 mm and outer radius 1.5 mm, made of quartz, which has a relative electrical permittivity $\varepsilon_r = 3.8$. Pivoting around the axle, the rod would describe an arc of circumference with radius 4 mm, with initial position (depicted in Fig. 4.9) at 36° and final position at 80°, where the 0° reference lies on the y axis and the center of the circumference is the dielectric axle. The second scenario involves only a single copper tuning rod, with the same dimensions as the first scenario and on the same positions. Actually, the second is the preferred scenario, but the first must be chosen if the single rod of the second scenario does not rotate properly, because of torques.

Simulations with the ANSYS HFSS suite [101] have been carried out to know the performances of the designed cavity at 4 K. The results are very similar in the two tuning scenarios, so I will only mention results for the case in which the dielectric axle is present. Simulating the movement of the metallic rod from 36° to 80°, the resonant frequency of the $TM010$ mode results in about 300 MHz tuning, ranging from 8.592 GHz to 8.900 GHz, as can be seen in Fig. 4.10. Note that higher order TM modes are also present in the cavity, but they never overlap with the primary $TM010$, as they shift in frequency by the same amount as the $TM010$ mode. Finally, the simulated $TM010$ quality factor at 4 K does not suffer from significant degradation, passing from a maximum value of about 1.1×10^5 at the rod's initial

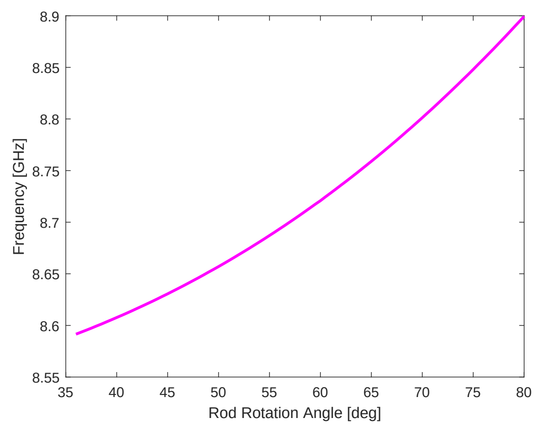

Figure 4.10: Frequency change as a function of the rod rotation angle, in the scenario with the rod attached to the dielectric axle.

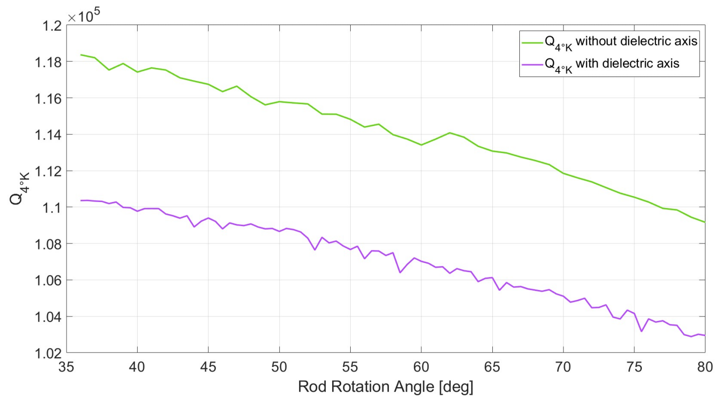

Figure 4.11: Simulations of the $TM010$ quality factor at 4 K in the tuning rod scenario with single rod (green) and with rod attached to a dielectric axle (violet). The difference between the two cases is of about 6%.

position to about 1.025×10^5 at the rod's stroke end. It is also important to mention that the quality factor in this scenario is degraded by a little amount with respect to the case where no dielectric axle is present. In fact, the dielectric causes some losses (depending on its tangent loss), but the quartz axle spoils the quality factor only by an amount of about 6%.

The quality factor results are shown in comparison in Fig. 4.11, where the violet curve refers to the dielectric axle case, while the Q of the single rod scenario is showed in green.

Fig. 4.12 shows a picture of the open resonant cavity and its spectrum up to 9.1 GHz at room temperature, showing some resonances. The inset is the zoom on the $TM010$ mode at 8.5 GHz, having a quality factor of about 13 000.

Now that the design parameters of the resonant cavity have been defined, the expected conversion power of an axion in a 9 T magnetic field can be calculated. Equation (3.9) can be

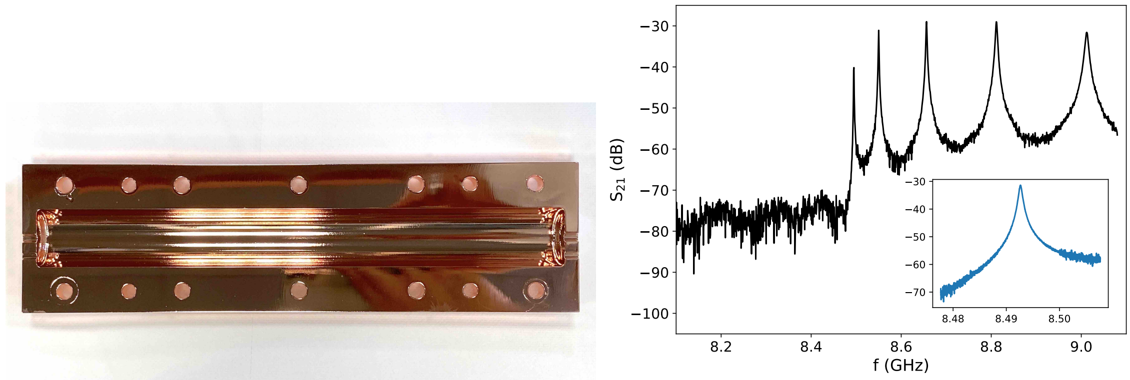

Figure 4.12: *Left*) Half of the electropolished OFHC copper cavity that will be used for measurements with the first tuning system. *Right*) 1 GHz-wide cavity spectrum. The inset shows the zoom on the $TM010$ mode at 8.5 GHz.

rewritten in a more readable form making experimental parameters explicit:

$$
\begin{aligned}
P_{a\gamma} \simeq 4.7 \times 10^{-24}\ \mathrm{W} \left(\frac{g_\gamma}{0.97}\right)^2 \left(\frac{\rho_a}{0.45\ \mathrm{GeV\,cm^{-3}}}\right) \left(\frac{V}{0.141\ \mathrm{l}}\right) \left(\frac{B}{9\ \mathrm{T}}\right)^2 \\
\times \left(\frac{C}{0.69}\right) \left(\frac{f_c}{8.58\ \mathrm{GHz}}\right) \left(\frac{Q}{1.2 \times 10^5}\right).
\end{aligned}
\tag{4.13}
$$

Here the power is considered at the resonance peak and the antenna is assumed to be critically coupled to the cavity ($\beta = 1$). With the design parameters of the tunable cavity with the rod in the initial position, the expected signal power in the KSVZ model (where $g_\gamma = -0.97$) is then $P_{a\gamma} \simeq 4.7 \times 10^{-24}$ W.

If a one-hour measurement were performed with the currently available HEMT amplifier, its 8 K added noise would lead to exclude a $g_{a\gamma\gamma}$ value one order of magnitude from the KSVZ line at 90% C.L. If a JPA with $T_n = 1$ K were used (as the one in Sec. 3.2.2), the sensitivity would increase to be at a factor of three from the KSVZ line. Using a resonant cavity with $Q \sim 300\,000$ in the same noise conditions, the sensitivity would reach the QCD band, almost at the KSVZ line. Such a cavity could be a superconducting one, as NbTi which was tested and used in [116, 117]. Finally, with a noise at the standard quantum limit of $T_n \sim 0.5\ K$ and a quality factor of $Q \sim 300\,000$, the KSVZ line sensitivity would be achieved.

To go further, a multicavity scheme can be designed (Chap. 7), and in this case the integration time gains a multiplication factor equal to the number of cavities read at the same time. To reach the DFSZ sensitivity instead, linear amplifiers constitute a technological limitation, underlining the need of a single photon detector at such high frequencies.

CHAPTER 5

Design of a single-photon detector based on a JJ

Before starting with the description of a Josephson junction as a photon detector, the advantage that a single photon counter has over linear amplifiers is stressed. The point was first discussed in [118] and then extended in [21]. Consider the Dicke equation (3.14) [103], that gives the fluctuations of the noise power of a receiver based on a linear amplifier:

$$\delta P_{\text{lin}} = k_B T \sqrt{\frac{\Delta\nu_a}{t}}, \tag{5.1}$$

where $\Delta\nu_a \simeq \nu[\text{GHz}] \times 10^{-6}$ is the axion linewidth, ν is the cavity resonance frequency, T is the system temperature and t the integration time. The point is that Equation (5.1) is only valid in the limit $k_B T \gg h\nu$ and must be modified for small temperatures. The new *ad hoc* equation can be written as [118]

$$\delta P_{\text{lin}} = h\nu(\bar{n}+1)\sqrt{\frac{\Delta\nu_a}{t}}, \tag{5.2}$$

where $\bar{n} = (e^{h\nu/k_B T} - 1)^{-1}$ is the photon occupation number in the cavity representing the thermal noise. From (5.2) the SQL is also clear: the vacuum fluctuations and the linear amplifier added noise both contribute $h\nu/2$ (Haus-Caves theorem [110, 111]), bringing to the minimum noise temperature $T_{SQL} = h\nu/k_B$, equal to about 500 mK for 10 GHz photons. Therefore, when approaching the low temperatures achievable with dilution refrigerators, where $\bar{n} \ll 1$, the noise is completely dominated by quantum fluctuations and does not depend on temperature.

On the contrary, the noise power for a single photon counter, derived assuming Poisson statistics and including dark counts, is [21]

$$\delta P_{\mathrm{sp}} = h\nu\sqrt{\frac{\bar{n}\Delta\omega_c + \nu_{DC}}{t}}, \tag{5.3}$$

with $\Delta\omega_c = 1/\tau_c$ the cavity linewidth and ν_{DC} the dark count rate. When $\bar{n} \approx 0$, photon counters do not suffer from the standard quantum limit, but they are limited by dark counts. Comparing the performances of linear amplifiers and photon counters at low temperatures,

$$\frac{\delta P_{\mathrm{lin}}}{\delta P_{\mathrm{sp}}} \simeq \sqrt{\frac{\Delta\nu_a}{\nu_{DC}}}, \tag{5.4}$$

it turns out that single photon counters will be competitive with respect to a quantum-limited amplifier if dark counts are below the intrinsic axion linewidth $\Delta\nu_a$, corresponding to $\nu_{DC} \simeq$ 10 kHz at 10 GHz. However, switching devices as current-biased Josephson junctions (CBJJs) have the potential to reach dark counts at mHz rates.

Within the SIMP project [119], we are developing a microwave single-photon detector based on CBJJs to couple to a haloscope, with the aim of probing the axion existence. In this Chapter I describe the device and its response to photon excitations obtained from simulations of different experimental conditions, showing that single photons can induce the switching of a JJ. I describe the first step in the characterization of a JJ with parameters optimized to detect photons originating from an axion conversion and derive the dark counts expected for a photon detector. Finally, the improvements needed to keep both high efficiency and a low dark count rate are discussed. My tasks included setting up the measurements, performing part of the analysis and drafting the related paper [1]. The simulations were performed by the people of the INFN group in Salerno.

The electrodynamics of a CBJJ is accurately described in terms of the resistively shunted junction (*RCSJ*) model [120], as previously described in Sec. 2.1.2. Fig. 5.1(a) is again the equivalent electrical circuit, now showing all the current sources. The capacitor C_J is the capacitance between the junction electrodes, the resistor R_J represents the tunneling of normal electrons (quasiparticles), and the component J_J represents the tunneling of superconductive electrons (Cooper pairs). The components I_s, I_b, and I_n are current sources that will be detailed below. The current I_J and the corresponding voltage drop V_J are related to the phase difference φ by the Josephson equations (2.1) and (2.2), that are again reported here for convenience:

$$I_J = I_0 \sin\varphi, \tag{5.5}$$

$$V_J = \frac{\hbar}{2e}\frac{\mathrm{d}\varphi}{\mathrm{d}t}. \tag{5.6}$$

As an additional comment to what is explained in Chap. 2, it is worth noting that in a typical tunnel-type JJ, the resistance R_J strongly depends both on voltage and temperature. However, as the overall effect of the resistor is to introduce dissipation in the system, its nonlinearity is often not considered in the presence of moderate or weak damping. Another important effect of the quasiparticle current, modeled by R_J, is the presence of random charge fluctuations, which can be represented, using the fluctuation-dissipation theorem, by a noise current source, indicated with I_n in Fig. 5.1, whose spectral power density is assumed to be frequency-independent (Johnson noise) [121].

A CBJJ as a photon detector. In order to use a JJ as a detector, it is biased with a dc current just below I_0 through a suitable source, indicated with I_b in Fig. 5.1. The occurrence of an external additional current (i.e., the signal to be detected) can induce the switching of the junction from the zero- to the finite-voltage state. Of course, current noise can also induce a switching, contributing to *dark counts*. In the washboard potential model (see Sec. 2.2) [87], sketched again in Fig. 5.2, the tilt is given by the normalized bias current I_b. In Fig. 5.2 the potential has quantized energy levels, where E_0 is the ground state of the phase particle energy and E_1 the first excited level. This is motivated if the $\cos\varphi$ term in the JJ potential (2.11) is expanded to the second order, which defines a harmonic approximation (see also [122]). This harmonic potential can be quantized, and the spacing between the levels is $\hbar\omega_p(I)$. The spacing can be varied according to the bias I_b, which changes the barrier height $\Delta U(I)$.

Upon the absorption of an incoming photon with enough energy, $E_{\text{ph}} \simeq \hbar\omega_p$, the phase particle can overcome the barrier height ΔU and escape from the potential well, rolling down the potential slope and giving rise to a finite-voltage state. At temperatures such that $k_B T \gg \hbar\omega_J$, the escape rate is dominated by the thermal activation (TA) process [123] (equation (2.14)), whereas at lower temperatures it is dominated by macroscopic quantum tunneling (MQT) (equation (2.17)), which provides an irreducible contribution to the dark count rate. An incoming photon with the right energy facilitates the escape process and would be detectable by measuring the voltage across the junction.

5.1 Device simulation

We investigated the dynamics of a CBJJ in the presence of a microwave pulse, representing the process of single-photon absorption, by means of numerical simulations of the model equations [124]. We estimated in this way the parameters needed to make the junction switch in the presence of a signal. This is done for three different scenarios: in one case, the ideal situation of an isolated JJ is considered; then a model of JJ coupled to an RC circuit is simulated, which is used to motivate the results obtained in Sec. 5.3; finally, the case of a JJ coupled to a transmission line is taken into account, which has been used to design the device described

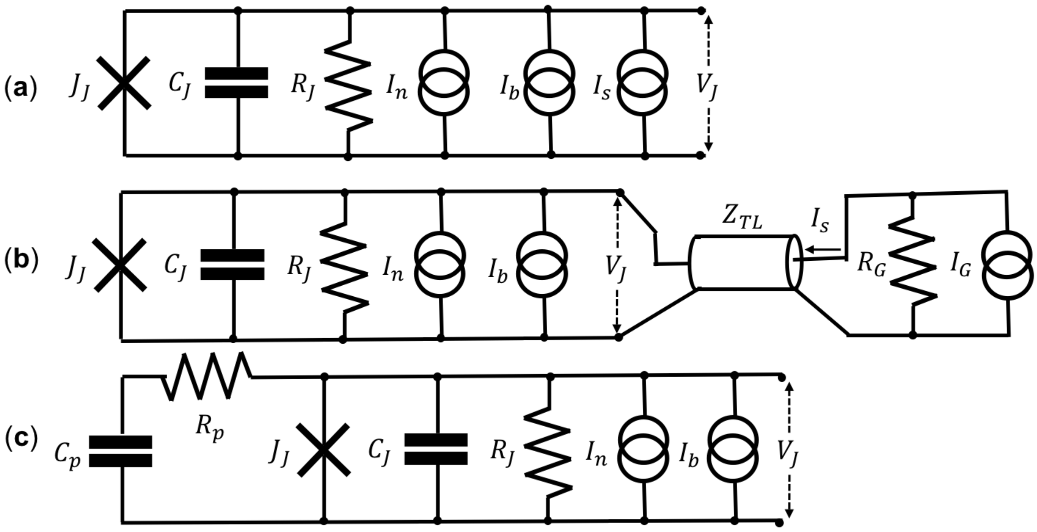

Figure 5.1: (**a**) An electrical model of a JJ with intrinsic and external current sources. (**b**) An electrical model of a JJ attached to a transmission line. (**c**) An electrical model of a JJ with a parasitic RC load.

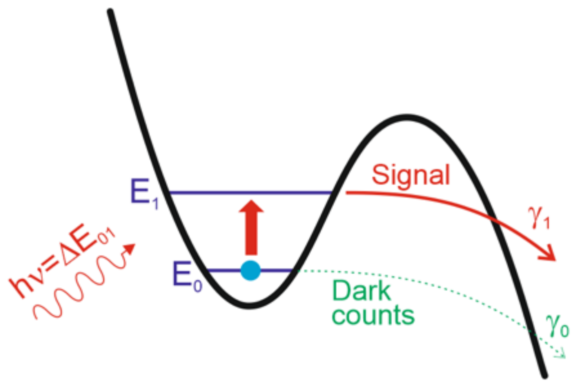

Figure 5.2: Equivalent potential of a JJ. The phase value is represented by the green particle which can overcome the energy barrier after the absorption of a suitable stimulus.

in Chapter 6 and to compare its experimental results with simulations.

5.1.1 Isolated CBJJ

To model a weak microwave field (weak because carrying few photons) coupled to the junction, we consider a deterministic current source, I_s in Fig. 5.1, generating a properly shaped current pulse, representing the absorption of a single microwave photon. The following equations refer to the circuit of Fig. 5.1(a) and describe the dynamics of an isolated junction where we imagine the current source directly coupled to the junction.

By denoting I_J as the current through the J_J element, I_{R_J} as the current through the resistor, and I_{C_J} as the current through the capacitor, we write the following current balance equation:

$$I_{C_J} + I_{R_J} + I_J = I_b + I_s\left(t\right) + I_n\left(t\right). \tag{5.7}$$

By using the constitutive relations of the resistor and capacitor, and the Josephson relations, we obtain the following second-order differential equation:

$$C_J \frac{\hbar}{2e}\frac{\mathrm{d}^2\varphi}{\mathrm{d}t^2} + \frac{1}{R_J}\frac{\hbar}{2e}\frac{\mathrm{d}\varphi}{\mathrm{d}t} + I_0 \sin\varphi = I_b + I_s\left(t\right) + I_n\left(t\right), \tag{5.8}$$

which, due to the presence of the stochastic noise term, is a Langevin equation [125]. By defining a normalized time $\tau = \omega_J t$, where

$$\omega_J = \sqrt{2eI_0/C_J\hbar} \tag{5.9}$$

is the Josephson plasma frequency, Equation (5.8) is re-written as

$$\frac{\mathrm{d}^2\varphi}{\mathrm{d}\tau^2} + \alpha\frac{\mathrm{d}\varphi}{\mathrm{d}\tau} + \sin\varphi = \gamma_b + \gamma_s\left(\tau\right) + \gamma_n(\tau), \tag{5.10}$$

where the parameters are defined as

$$\alpha = \frac{1}{R_J C_J \omega_J}, \qquad \gamma_b = \frac{I_b}{I_0}, \qquad \gamma_s = \frac{I_s}{I_0}. \tag{5.11}$$

The statistical properties of the noise term γ_n are:

$$\begin{aligned} \langle\gamma_n(\tau)\rangle &= 0, \\ \langle\gamma_n(\tau), \gamma_n(\tau')\rangle &= 4D\delta(\tau - \tau'), \end{aligned} \tag{5.12}$$

where $D = k_B \mathcal{T} \omega_J / \left(R_J I_0^2\right)$ is the normalized noise intensity (k_B is the Boltzmann constant and $\mathcal{T}$ the physical temperature), $\delta()$ is the Dirac delta function, and the parentheses $\langle\rangle$ represent ensemble averages.

5.1.2 CBJJ coupled to an RC circuit

If the JJ is small in size, its capacitance and conductance can be very small too, thereby making it possible for external parasitic effects to modify its dynamics. To investigate these effects, we considered a model of a JJ loaded with a series parasitic RC circuit, as in Fig. 5.1(c). This is due to the load of the twisted dc leads feeding the JJ with the bias current. In this case, Equation (5.7) becomes:

$$I_{C_J} + I_{R_J} + I_J + I_{R_p} = I_b + I_s\,(t) + I_n\,(t)\,, \tag{5.13}$$

where I_{R_p} is the current flowing in the parasitic resistor R_p. The JJ voltage V_J is related to I_{R_p} by:

$$V_J = R_p I_{R_p} + \frac{1}{C_p}\int I_{R_p}\,\mathrm{d}t. \tag{5.14}$$

By repeating the same procedure as before, we obtain the following two normalized differential equations:

$$\frac{\mathrm{d}^2\varphi}{\mathrm{d}\tau^2} + \alpha\frac{\mathrm{d}\varphi}{\mathrm{d}\tau} + \sin\varphi = \gamma_b + \gamma_s\,(\tau) + \gamma_n(\tau) + \gamma_R, \tag{5.15}$$

$$\frac{\mathrm{d}\gamma_R}{\mathrm{d}\tau} + \alpha_{RC}\gamma_R + \alpha_{int}\frac{\mathrm{d}^2\varphi}{\mathrm{d}\tau^2} = 0, \tag{5.16}$$

where

$$\alpha_{RC} = \frac{1}{R_p C_p \omega_J}, \qquad \alpha_{int} = \frac{1}{R_p C_J \omega_J}, \qquad \gamma_R = \frac{I_{R_p}}{I_0}. \tag{5.17}$$

5.1.3 CBJJ coupled to a transmission line

The simplest design for a photon detector operating at microwave frequency based on a JJ is a transmission line (TL), such as a coplanar waveguide, terminated with a JJ. When the JJ is coupled to a TL with a characteristic impedance Z_{TL}, as shown in Fig. 5.1(b), signal reflection back to the TL has to be considered. The overall effect is modeled by a modified effective junction resistance, given by the values of the parallel resistors R_J and Z_{TL}. In Fig. 5.1(b), the current source I_s is given by an ideal generator I_g with an impedance R_g in parallel. The latter has to be equal to Z_{TL} to ensure impedance matching. To relate the simulation results to this particular case, we compare Equation (5.8) with the equation for the flux variable $\phi = \varphi(\phi_0/2\pi)$ in a TL terminated by a parallel LC (a linearized JJ) [126]:

$$C_J\ddot{\phi} + \frac{\phi}{L_J} + \frac{1}{Z_{TL}}\dot{\phi} = 2\frac{1}{Z_{TL}}\dot{\phi}^{in} = 2I^{in}, \tag{5.18}$$

where L_J is the Josephson inductance and the term $1/Z_{TL}$ models the aforementioned signal reflection on the TL. Moreover, the current I_s has to be interpreted as twice the input current I^{in}, as motivated in Appendix B. The input peak current due to a single photon on the waveguide with a Gaussian wavepacket of time duration σ_t is

$$I_{\text{peak}}^2 = \frac{\hbar\omega_J}{Z_{TL}} \frac{2}{\sqrt{2\pi}\sigma_t}. \tag{5.19}$$

Then, the amplitude of the signal current I_s in Equation (5.8) corresponding to a single photon is:

$$I_s^{\text{photon}} = 2\sqrt{\frac{\hbar\omega_J}{Z_{TL}} \frac{2}{\sqrt{2\pi}\sigma_t}}. \tag{5.20}$$

For a 10 GHz photon with $\sigma_t = 600$ ps on a 50 Ω TL, this corresponds to about 26 nA. The value of 600 ps was chosen to best accomplish the activation of the junction when coupled to a TL with $Z_{TL} = 50\ \Omega$. In fact, with a 10 GHz photon, the JJ phase makes a complete oscillation in a period of about 100 ps. An incoming signal with smaller duration would not have the time to drive the junction oscillations. Moreover, speaking of bandwidth instead of period, the efficiency on the detection of a signal with bandwidth greater than that of a detector would be completely lost. Here, the bandwidth of the JJ coupled to the TL is defined as the relaxation rate $\gamma_{TL} = \omega_J/Q = \omega_J Z_J/Z_{TL} = 1/Z_{TL}C_J$, where $Z_J = \sqrt{L_J/C_J}$ and $C_J \sim 1$ pF. In our simulation, the 600 ps wavepacket has a bandwidth of the order of 0.3 GHz, well within the bandwidth of about 1.5 GHz associated to a relaxation time of $\gamma_{TL}^{-1} = Z_{TL}C_J \sim 100$ ps.

5.1.4 Design simulations of a photon detector based on JJ coupled to TL

We ran several simulations with the CBJJ either isolated or coupled to a TL excited by Gaussian current pulses of about 600 ps in length. We considered values of the critical current ranging from few hundred nanoAmperes to a few microAmperes, and junction capacitance ranging from a fraction of a picoFarad to a few picoFarads, as shown in the table of Fig. 5.3. The chosen areas are 6, 8, 12 and 16 μm^2, while having different combinations of capacity and critical currents, thus obtaining eight different junctions. The ratio I_b/I_0 was set in such a way as to keep the estimated rate of the MQT from the ground level by a few Hertz at most and to keep a good switching efficiency.

We first checked that the isolated junction gives the best performances when excited by microwave pulses. In this situation, the impedance is set to the subgap resistance $R_J = 50$ kΩ (last column in Fig. 5.3). With the isolated junction, we observed switching currents I_{sw} between 20 and 50 nA corresponding to about 1 to 4 photons, estimated as

$$N_\gamma = \left(\frac{I_{\text{sw}}}{I_s^{\text{photon}}}\right)^2. \tag{5.21}$$

					Rj = 50 Ohm	Rj = 50 kOhm
Area (µm²)	C (pF)	Ic (nA)	Ibias/Ic	νp (GHz)	I switch (nA)	I switch (nA)
6	0,5	1300	0,93	8,6	300	
8	0,7	1700	0,94	8,3	240	
12	1,2	4284	0,96	8,77	220	
16	1,6	5712	0,97	8,17	200	
6	0,375	477	0,85	7,2	320	25
8	0,5	637	0,87	7,0	330	30
12	0,75	956	0,90	6,5	260	35
16	1,0	1275	0,92	6,2	240	30

Figure 5.3: Simulation parameters for eight different junctions. From left to right, the columns are: the area of the junctions; the capacity; the critical current; the normalized bias; the plasma frequency at the bias I_b; the current pulse value at which the JJ switches when coupled to the TL ($R_J = 50\ \Omega$); the current pulse at which the JJ switches when isolated ($R_J = 50\ \mathrm{k}\Omega$).

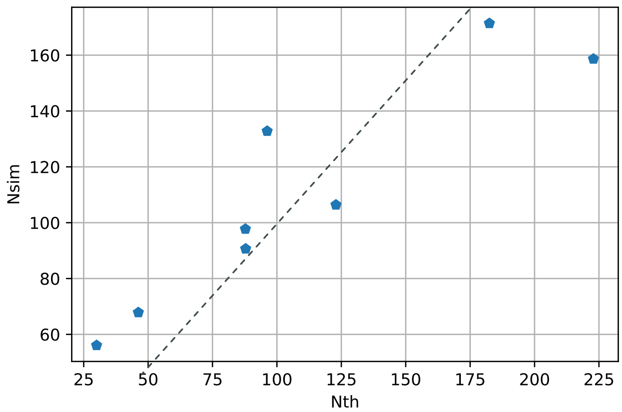

Figure 5.4: Number of simulated photons compared to the number of levels in the potential well, for a JJ coupled to a 50 Ω TL. The blue points are the simulation results and are approximately distributed around the dashed line representing $N_{\text{sim}} = N_{\text{th}}$.

On the contrary, with the junction coupled to a 50 Ω TL, the relaxation rate of the junction $\gamma_{TL} = 1/Z_{TL}C_J$ inhibits the junction switching, so that to cause an escape event, a number of photons equal to the number of levels in the potential well must reach the junction within a time $1/\gamma_{TL}$. The number of levels in the potential well is calculated considering the raw approximation of harmonic potential, giving

$$N_{\text{lev}} = \frac{\Delta U(I)}{\hbar\omega_p(I)}\,. \tag{5.22}$$

The values of switching current increased to a range between 200 to 300 nA, corresponding to about 100 photons. The results are collected in the plot of Fig. 5.4, where each point corresponds to one of the eight simulated junctions. On the y-axis, N_{sim} is given by Eq. (5.21), while on the x-axis N_{th} is the expected number of photons required to jump out of the well with N_{lev} levels:

$$N_{\text{th}} = N_{\text{lev}}\sqrt{2\pi}\sigma_t\gamma_{TL}\,. \tag{5.23}$$

In Fig. 5.4, the dashed line indicates the equality $N_{\text{sim}} = N_{\text{th}}$. The simulated points are then approximately distributed around this line. Thus, we expect that the junction switches when a number of photons $N_\gamma \approx N_{\text{lev}}$ is absorbed within the time $1/\gamma_{TL}$.

The increase of the number of photons needed to switch is directly proportional to the relaxation rate γ_{TL}, highlighting the need for a proper circuit for matching the CBJJ to the TL. Matching of a device to a TL is discussed in [18, 122], where the detection efficiency is expressed as

$$P_{\text{R}} = \frac{4\gamma_{TL}\gamma_{\text{sw}}}{(\gamma_{TL}+\gamma_{\text{sw}})^2}. \tag{5.24}$$

γ_{sw} is the switching rate of the excited JJ to the resistive state. The perfect matching condition $\gamma_{TL} = \gamma_{\text{sw}}$ implies that the escape to the resistive state must be as fast as the relaxation of the junction to the ground level. This prevents us from using MQT transitions from the first excited level as a detection mechanism: an escape caused by MQT from the first excited level, E_1 in Fig. 5.2, equal to $\gamma_{TL} \sim$ 1–10 GHz, would give rise to a dark count rate due to escape from the ground level of about $\gamma_0 \sim 10^{-3}\gamma_{\text{sw}} \sim$ 1–10 MHz[1]. On the contrary, while keeping low dark count rates, one or more photons may induce the escape by resonant activation within the relaxation time $1/\gamma_{TL}$. A discussion on the design of a proper matching circuit, the stub tuner, is present in Chapter 7.

After estimating a suitable bias for the junction activation from simulations, the following Sections are dedicated to the experimental verification of the existence of a suitable working point for a photon detector.

5.2 Dc characterization of JJ for the working point determination

The study of the escape mechanisms of a CBJJ allows understanding and characterizing the escape rates in the absence of excitation signals, and therefore of the dark counts. Much literature on measurements and interpretations of the escape processes has been published and underlines different dynamics, such as the TA regime, MQT, and phase diffusion (PD) with multiple retrapping processes [81, 86–89, 127–131]. The experimental conditions to highlight the diverse regimes and transitions between them have been defined. The regimes will depend on the comparison between the Josephson energies (E_J), related to the Josephson critical current I_0; the Coulomb energy E_C, depending on the capacity C_J; the plasma frequency ω_J proportional to the $\sqrt{I_0/C_J}$ ratio; the quality factor $Q = \omega_J R_J C_J$, proportional to the losses; the potential tilt $E_J\,(I/I_0)$, controlled by the bias current I; and temperature [81,

[1] The factor of about 10^{-3} comes from the MQT escape rate of Eq. (2.17): when considering two consecutive levels in the potential, which are separated by $\hbar\omega_p$ in the harmonic approximation, the ratio between their quantum escape rates gives $e^{-36/5} \simeq 0.75 \times 10^{-3}$.

86–89, 127–131]. This rich phenomenology of the escape process makes it ideal for a DC characterization of a JJ. In general, the typical escape dynamic's experimental setup consists in a slow ramping of the bias current across the junction up to the value of the critical current [127]. This ensures both that the JJ stays at the temperature of the cryostat thermal bath at milliKelvins, and that the superconducting state does not dissipate during the escape measurements before the final switching. Then, the data analyzed are the switching current distributions produced after countless repetitions of the process. Finally, measurements as a function of temperature can be a diagnostic tool for determining the processes of TA, tunneling, and phase diffusion regimes that regulate the escape process.

5.2.1 Fabrication parameters

The JJs we tested were fabricated at the Institute of Photonics and Nanotechnology (IFN) of CNR in Rome by shadow mask evaporation (Figure 5.6), with electron beam lithography on a copolymer/PMMA bilayer (thickness of about 1 μm for each layer) over a Si substrate, with two evaporation angles of Al at 25° and 90° (thickness of about 30 nm), and with 5 min of oxidation at 5 mbar (expected thickness of the order of 1 nm). The fabrication process is described in Sec. 2.6. Two junctions with different areas were fabricated: 2 μm $\times$ 2 μm ($I_0 \simeq$ 300 nA and $C \simeq$ 200 fF, expected from design parameters) and 2 μm $\times$ 4 μm ($I_0 \simeq$ 600 nA and $C \simeq$ 400 fF).

5.2.2 Setup

We tested the devices in a range of temperatures between 50 mK and about 1 K in a Leiden Cryogenics MCK 50–100 dilution refrigerator (Figure 5.5). We used a 4-terminal measurement scheme (Figure 5.7), with a bias resistance R = 14.63 kΩ at room temperature, twisted/shielded phosphor bronze cryogenic lines (about 25 Ω per line), and EMI low-pass filters at room temperature (bandpass 600 kHz). An Agilent 33220A waveform generator was used, together with two low noise preamplifiers (both EGG 5113) and a NI USB 6366 acquisition board.

This experimental setup allowed us to acquire current-voltage characteristics. We measured a gap $\Delta \simeq$ 200 μV and critical currents within a factor 2 with respect to the estimated ones (Figure 5.8), indicating the presence of some trapped magnetic field.

In order to measure the escape probabilities, we applied a sawtooth waveform with frequency f = 314 Hz, amplitude I_{pp} = 670 nA and offset I_{off} = 250 nA. In each period, during the slow growth (with slope $\mathrm{d}I/\mathrm{d}t$ = 210 μA/s), sudden transition to the voltage state occurred at random values of current I_c. In the fast decrease region, the junction resets to the superconducting state. We acquired a series of N = 5000 transition values I_c by using the voltage jumps as trigger signals. These values were arranged in a histogram to evaluate the escape probability $P(I)$. In Fig. 5.10 we report the experimental escape probabilities at

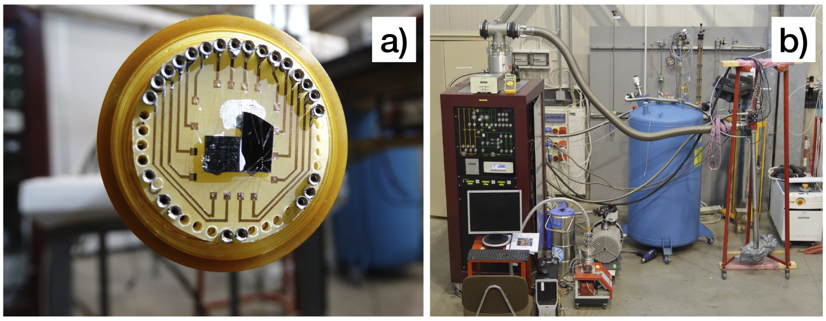

Figure 5.5: (**a**) The chip holding the JJ, attached to the end of the insert, in thermal contact with the mixing chamber. (**b**) View of the Leiden Cryogenics MCK 50–100 dilution refrigerator.

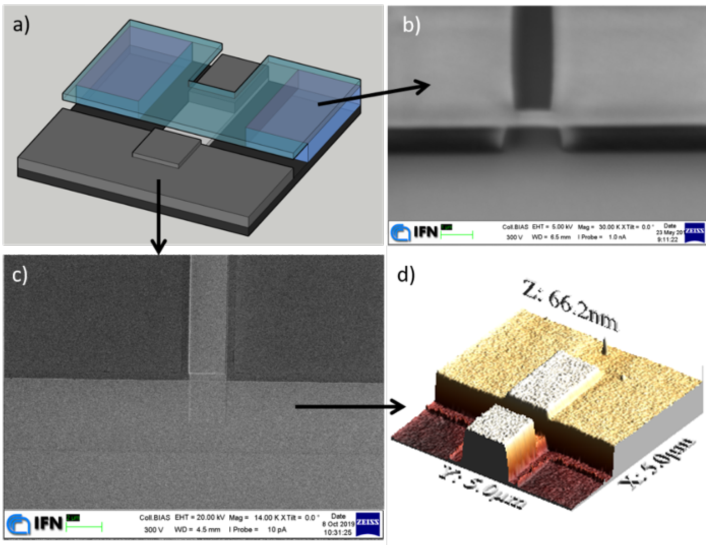

Figure 5.6: (**a**) Schematic image of the shadow mask evaporation technique. The copolymer/PMMA bilayer was exposed by EBL and developed, in order to obtain a self-standing bridge of the desired geometry, as shown by the scanning electron microscope (SEM) micrograph in (**b**). A two-angle evaporation with an oxidation step in between defines the junction geometry (light and dark gray in (**a**). (**c**) SEM micrograph of the junction after the lift-off process used to remove the bilayer mask. (**d**) An atomic force microscope (AFM) characterization of a typical junction.

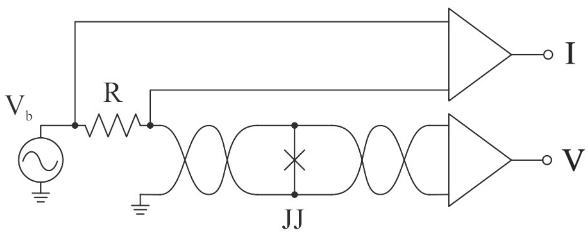

Figure 5.7: A scheme of the experimental setup.

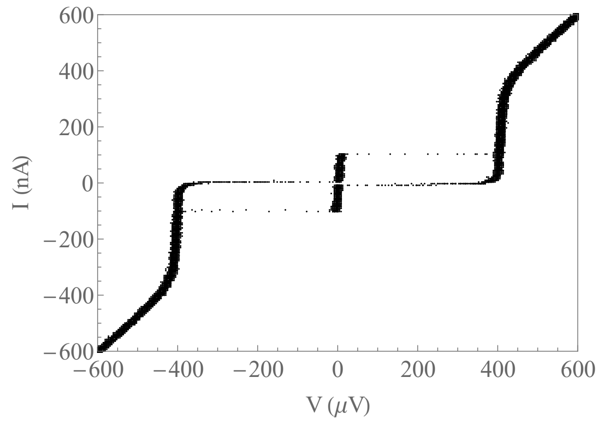

Figure 5.8: Measured voltage-current characteristic of a Josephson junction (2 μm$\times$ 2 μm).

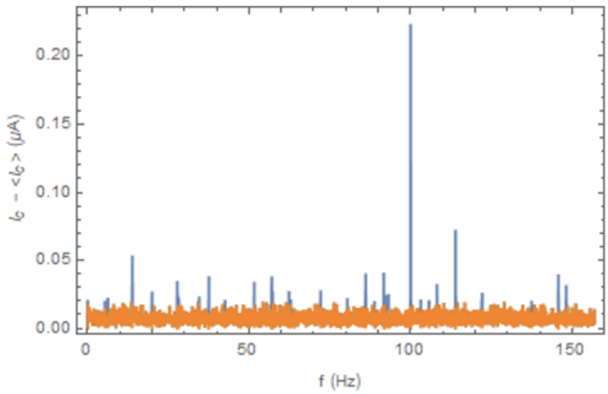

Figure 5.9: Fourier transform of the 5000 measured I_c values before filtering (blue) and after filtering out the low-frequency noise (orange).

different temperatures ranging from about 40 to 850 mK. Data analysis is discussed in the next section.

5.3 Results and discussion

5.3.1 Results

From the 5000 transition values I_c we constructed escape-probability densities. Before doing this, we applied a fast Fourier transform to the measured I_c series and identified a narrow peak at 100 Hz and minor peaks at lower frequencies, attributed to electronic noise in the current measurement setup (blue lines in Fig. 5.9). We calculated the peaks' frequencies, phases, and amplitudes from the Fourier analysis, and filtered out the noise from the original I_c series (orange data in Fig. 5.9). We thereby obtained a 20% improvement in resolution. We show the experimental switching distributions $P(I)$ obtained after filtering the data for each temperature in Fig. 5.10—the smallest and the largest junctions, respectively.

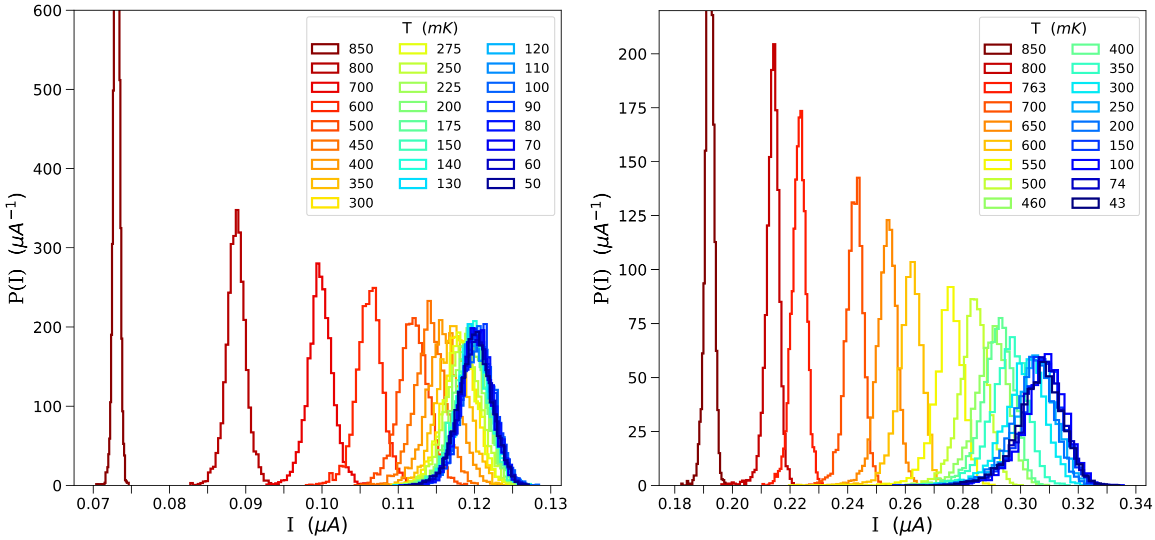

Figure 5.10: Filtered escape current distributions for $2\,\mu\text{m} \times 2\,\mu\text{m}$ junction (*Left*) and for $2\,\mu\text{m} \times 4\,\mu\text{m}$ junction (*Right*). The ranges of temperatures are slightly different and are shown in the legends. Rightmost curves are taken at the lowest temperature and leftmost curves are taken at highest temperature. The effect of the filter was a reduction of σ up to 20% with respect to the unfiltered data (not shown); $\langle I_c \rangle$ was left unchanged.

We extracted the mean $\langle I_c \rangle$ and width σ from each distribution as an arithmetic mean and a standard deviation. These are plotted as a function of temperature in Figure 5.11, for the two junctions.

The mean critical current values (empty blue squares) follow qualitatively the typical BCS behavior [120] as a function of temperature. The widths (full red squares) present a peculiar feature. The constant behavior of σ at low temperatures was expected from quantum tunneling processes, as Fig. 5.12 shows, whereas its decrease at higher temperatures, above about 400 mK, suggests that TA is suppressed—while it is supposed to increase as $T^{2/3}$ (Fig. 5.12). We attribute the decreasing regime partially to the decrease of the critical current with increasing temperature, although a further contribution due to retrapping is not excluded.

5.3.2 Interpretations of results

To investigate the effect of a dissipative environment on the escape by TA, we ran simulations of the JJ in parallel to the dissipative RC circuit shown in Figure 5.1(c) and described in Section 5.1.2. In our experimental setup, the parasitic circuit is represented by the dc lines carrying the bias current to the junction. The driving equations of the simulations were obtained from Equations (5.13)–(5.17) by setting the current source $I_s(t)$ to zero. Qualitatively,

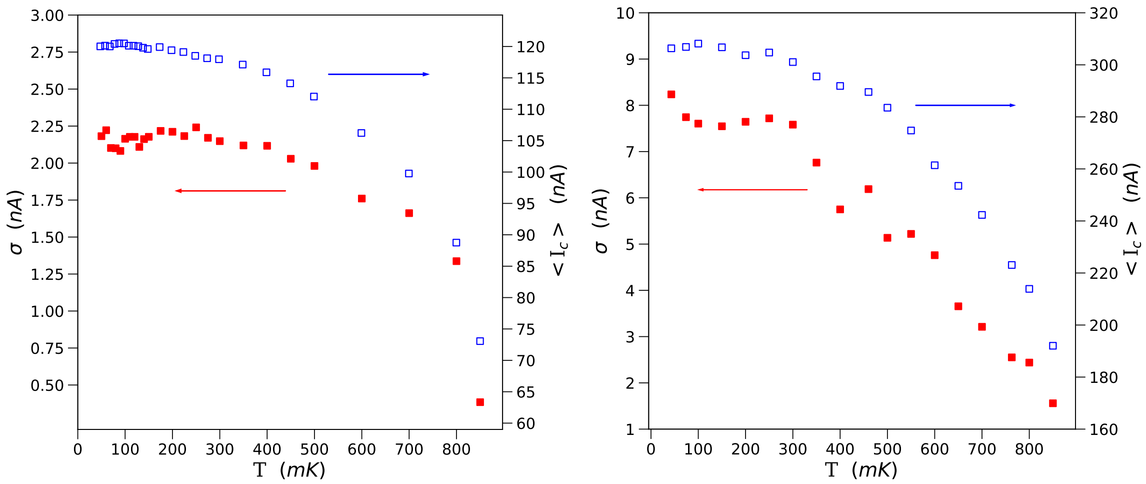

Figure 5.11: $\langle I_c \rangle$ and σ for $2\,\mu\mathrm{m} \times 2\,\mu\mathrm{m}$ junction (*Left*) and for $2\,\mu\mathrm{m} \times 4\,\mu\mathrm{m}$ junction (*Right*). In both plots, the red squares are relative to the left axis (widths) and the empty blue squares are relative to the right axis (mean currents), as indicated by the arrows.

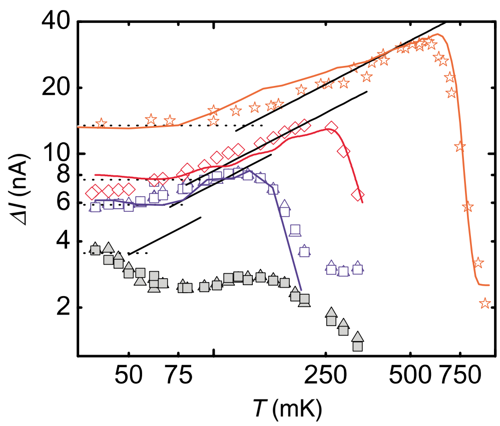

Figure 5.12: Classical behavior of the switching distributions widths as a function of temperature, for some experimental data sets measured by [127].

in the RCSJ model, energy dissipation induced a relaxation rate

$$\Gamma_{\text{rel}} = \frac{1}{\tau} = \frac{1}{RC_J} = \frac{\omega_J}{Q}, \tag{5.25}$$

where R is the parallel between R_J and R_p. If relaxation is faster than the TA, the latter is suppressed:

$$\frac{\omega_J}{2\pi} \exp\left(-\frac{\Delta U}{k_B T}\right) < \frac{\omega_J}{Q}, \tag{5.26}$$

corresponding to the condition

$$R < 2\pi Z_J \exp\left(\frac{\Delta U}{k_B T}\right). \tag{5.27}$$

Thus, even for temperatures such that $k_B T \sim \Delta U$, TA is suppressed if $R < 2\pi e Z_J \sim 20 Z_J$. For the described junction, Z_J is $\sim 50\ \Omega$; therefore, an external resistance equal to about 1 kΩ would dominate in parallel to $R_J = 100$ kΩ, causing dissipation. On the contrary, the MQT process, which is not affected by dissipation, would become the dominant switching effect even at temperatures higher than the expected crossing temperature. This was confirmed by our simulations, whose results for different simulation parameters are shown in Figure 5.13. The inclusion of the RC circuit strongly modifies the qualitative behavior of I_c and σ as a function of the temperature. In Figure 5.14 we show the comparison of the experimental results obtained for the 2 μm $\times$ 2 μm junction and results of a simulation run with parameters $I_0 = 143$ nA, $C_J = 0.2$ pF, $R_J = 100$ kΩ, $C = 2$ pF, and $R_p = 1$ kΩ, where only MQT and dissipation were included. Both the simulated distributions of I_c and σ are in good agreement with the measured ones. As anticipated, a further contribution from a retrapping process at a higher temperature could take into account the observed residual difference between the experimental and simulated values of σ.

As shown in Figures 5.10 and 5.11, the experimental behavior observed for the 2 μm $\times$ 4 μm and the 2 μm $\times$ 2 μm junctions is similar. Therefore, even if the analysis was not repeated for the 2 μm $\times$ 4 μm junction, we do not expect a different interpretation of the results.

5.3.3 Dark-count rate

Finally, we investigate the dark count rate performances of the 2 μm $\times$ 2 μm junction to predict how it would behave if used as a single photon counter. Following [132], we calculated the escape rate from the current distribution of the JJ taken at the lowest temperature (50 mK). The result as a function of the bias current is shown in Figure 5.15, where the blue dots represent the escape rate values extracted from data, obtained using Eq. (2.22). The dashed red line is the escape rate expected from MQT only. It reproduces the data for currents up to 120 nA, where the current distribution at 50 mK has its maximum (Fig. 5.10 left). The devia-

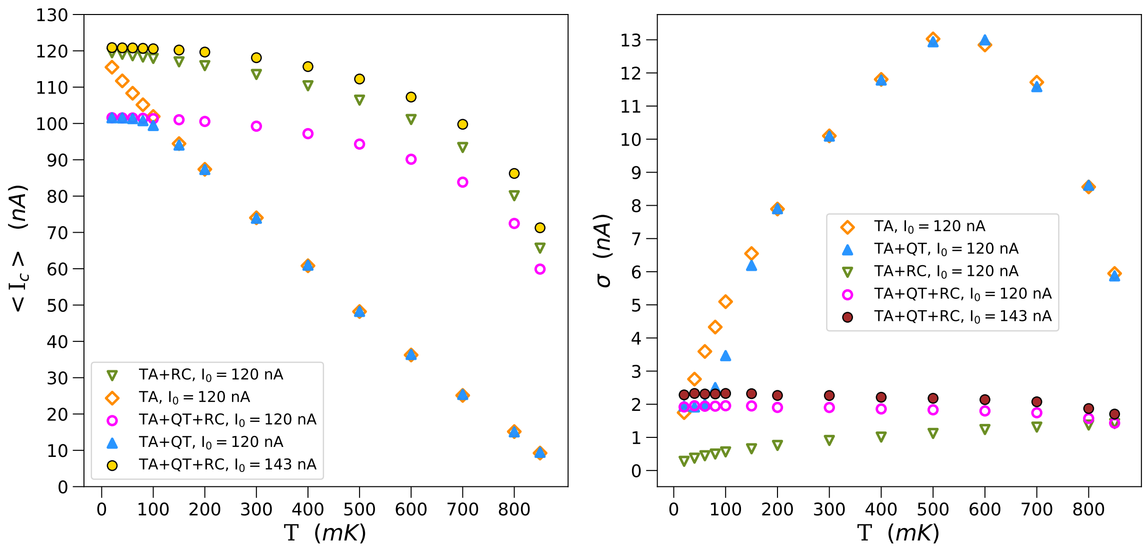

Figure 5.13: Mean switching currents (*Left*) and widths (*Right*) of the simulated data for different simulation parameters. In the legend, TA refers to thermal activation processes, QT to quantum tunneling, and RC to the dissipation effect due to the external circuit.

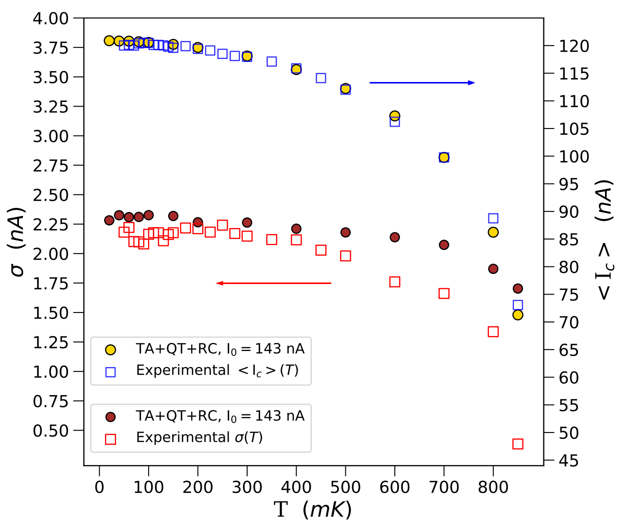

Figure 5.14: Comparison of the mean switching currents and widths of the simulated data with $R_p = 1$ kΩ, $C = 2$ pF, $R_J = 100$ kΩ, $I_0 = 143$ nA, and $C_J = 0.2$ pF with respect to experimental results of the $2\,\mu$m $\times$ $2\,\mu$m junction, shown in empty squares.

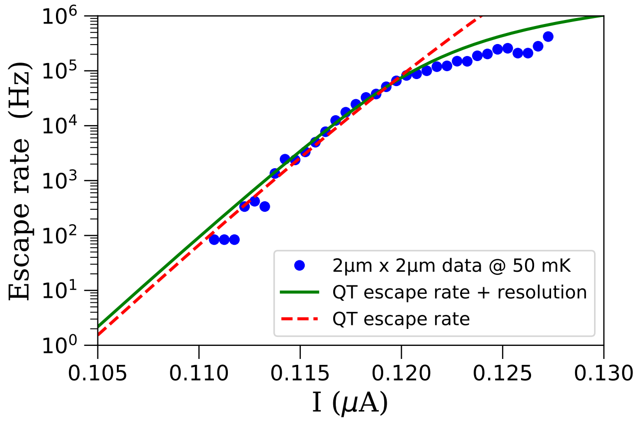

Figure 5.15: Experimental dark count rate for the $2\,\mu m \times 2\,\mu m$ junction at 50 mK, compared with quantum tunneling escape rate (red dashed line) and quantum tunneling plus the effect of 1.1 nA of Gaussian smearing (green solid line).

tion at higher currents is attributable to a Gaussian resolution effect with standard deviation $\sigma = 1.1$ nA, as confirmed by the data's agreement with the green solid line obtained by applying such a smearing to the theoretical current distribution of the MQT before deriving the escape rate.

To determine the working point for a photon detector based on a similar JJ ($I_0 = 140$ nA, $C_J = 0.2$ pF), we relied on the simulation of an "isolated" junction with $R_J = 5$ kΩ driven by a resonant rf Gaussian pulse of frequency 6.5 GHz, duration $\sigma_t = 370$ ps, and peak current $I_{max} = 21$ nA corresponding to one photon. The simulated junction switched for a bias current $I_b \simeq 91$ nA ($\gamma_b \simeq 0.65$) when the junction plasma frequency was about 6.5 GHz. By extrapolating the escape rate measured in our data (Figure 5.15) to the value $\gamma_b \simeq 0.65$, we estimated for the photon detector a dark count rate of about 1 mHz.

It should be noted that in simulations with $R_J < 1.5$ kΩ, dissipation inhibits junction switches, as observed in the TA process in our data and as expected from the discussion in Section 5.3.2. As already noted in Section 5.1.3, when a junction is coupled to a TL, the 50 Ω line impedance acts as a dissipative medium, preventing the junction from switching. Moreover, when $\gamma_b \simeq 0.65$, the height of the potential well is estimated to be 28 GHz, corresponding to about four energy levels, showing that the current pulse must induce a strong modification of the potential to cause the junction switching.

5.4 Summary

We have investigated the escape mechanism of a CBJJ both with simulations and through measurements of the escape currents in two Al JJs. We highlighted the effect of the dissipative mechanism introduced by the current leads—in particular, the suppression of escape induced by TA. While this suppression leads to a reduction in the escape rates and to dark counts above the crossover temperature, it also implies a low quality factor with consecutive reductions in signal efficiency, and this must be taken into account in the design of a microwave photon counter. We in fact showed with simulations that a current pulse with peak current $I_{max} = 21$ nA, corresponding to a single photon, induces the switching of an isolated junction of critical current $I_0 = 140$ nA when biased with a current $I_b \simeq 91$ nA, and that the expected dark count rate would be at the milliHertz level. This value was confirmed by the escape rates extracted from our data. However, when the junction was not isolated but coupled to a TL, the simulation showed that switches were inhibited, and larger current pulses were required. The JJ must then be resonantly matched with the TL with a bandwidth estimated to be of the order of $1/R_jC_j \sim 1$ GHz.

CHAPTER **6**

Resonant activation in the first prototype of a JJ photon detector

As anticipated in Chap. 5, we aim to develop a single microwave photon counter based on current-biased Josephson junctions to be used as the photon detector in an axion haloscope. The absorption of a microwave photon triggers the transition of the junction to the normal state, due to an escape of the phase variable from the atom-like potential well, and this causes a sudden variation of the voltage across the junction. In principle, we would like the junction to switch when hit by one single photon and at the same time have a low dark count rate, at the milliHertz level. With the results of Chap. 5 we demonstrated that the latter point is feasible.

While in the previous Chapter I described the dc characterization of a JJ mainly to gather information on its noise performance, this Chapter is dedicated to the characterization of the first and simplest prototype of photon detector, a transmission line terminated with a single JJ. The response of the junction to microwaves is investigated, to mimic the arrival of a photon while the junction is biased. This is done both by applying a continuous rf signal (Sec. 6.3) and pulsed rf (Sec. 6.4), a situation that is similar to the excitation with a handful of microwave photons.

Note that, as anticipated in subsection 5.1.4, there is a significant mismatch between the transmission line and the junction, being their impedances $Z_{TL} = 50\ \Omega$ and $R_J = 50\ \mathrm{k}\Omega$, causing signal reflection and a small relaxation time $\tau = \gamma_{TL}^{-1}$. The matching issue is a critical point in the design of an efficient photon detector and a possible solution is discussed in Sec. 6.5.

6.1 Experimental setup

The junction is again an $Al/AlO_x/Al$ one, and the sample is tested in the Leiden Cryogenics CF-CS110-1000 dilution refrigerator described in Sec. 4.2.2, where we registered a base temperature of 10 mK.

6.1.1 Sample fabrication parameters

The Josephson junction used for rf characterization has been fabricated at IFN-CNR with the same technique as the JJs mentioned in the previous Chapter, a shadow mask evaporation with electron beam lithography (see Sec. 2.6), but the fabrication parameters are a bit different. The resist is again a copolymer/PMMA bilayer (with thickness of about 1 μm for each layer) over a Si substrate. The Al evaporation angles are 155° and 90° (thickness of about 30 nm), with an intermediate oxidation of 5 min at 3 mbar (expected thickness between 1 and 1.5 nm). The resulting junction has an area of 8 μm^2 and expected critical current and capacity of $I_0 \simeq 3$ μA and $C \simeq 1$ pF. The choise to fabricate a JJ with bigger area with respect to Chap. 5, and thus a bigger capacity, is motivated by the fact that increasing the quality factor $Q = \omega_p RC$ means increasing the relaxation time $\tau = Q/\omega_p$, preventing the junction to immediately reflect photons back into the TL.

The 5.44 mm-long Al transmission line feeding the junction is fabricated at the same time and with the same technique as the JJ, and is galvanically connected to the junction. The losses due to connection mismatches from the TL to the cryostat rf lines are minimized by keeping the impedance to 50 Ω. To achieve a 50 Ω impedance in the TL, the width of the central conductor and the distance between the latter and the grounding are linearly reduced from millimeters to micrometers. In particular, the final sizes are 10 μm for the central conductor and 5.8 μm for the gaps between the latter and the grounding. The connectors are of the SMA type with a 50 Ω impedance, as by specifications, and the cryostat is provided with 50 Ω rf lines. The only uncertainty is left to the bonding wires from the chip to the TL, but since they are very short we expect a small effect, widely contained within the calibration uncertainty (subsection 6.1.2).

The left picture of Fig. 6.1 shows the chip on which the junction and the transmission line are deposited, and is mounted in the sample holder. The junction studied in this Chapter is the second from the bottom of the chip, and the thin wires soldered to the transmission line can also be seen in the figure. The image on the right of Fig. 6.1 is a picture of the junction taken at the microscope.

Since the empty remaining volume in the sample holder behaves as a resonant cavity, we simulated its geometry with ANSYS HFSS. We found a single TM mode at a frequency of about 12.51 GHz; Fig. 6.2 shows on the right the electric field component, which is present in all the "cavity" volume, while on the left the simulated S_{21} resonance is plotted.

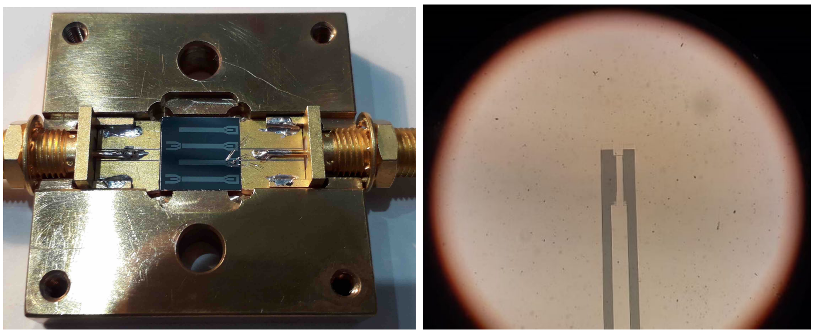

Figure 6.1: *Left)* Picture of the sample holder containing the chip on which the junction coupled to the transmission line is deposited. *Right)* Microscope image of the Josephson junction.

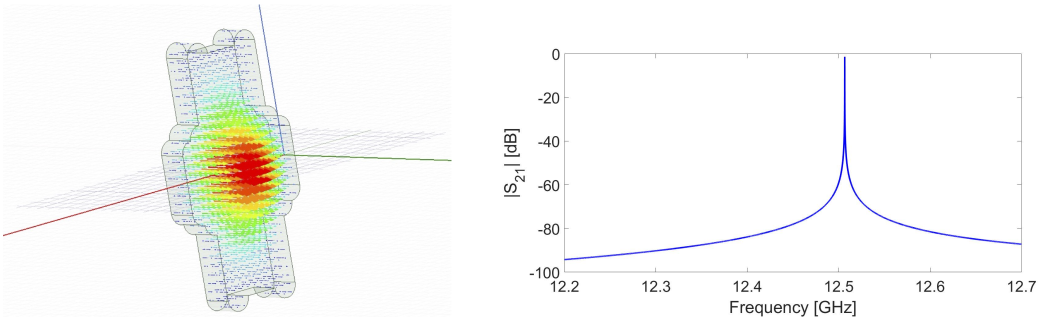

Figure 6.2: *Left)* Electric field lines from the simulation of the TM mode of the sample holder. *Right)* Its resonance peak at 12.51 GHz, plotted as an S_{21} scattering parameter.

6.1.2 RF diagram and calibration

The rf diagram that schematizes the measurements setup is shown in Fig. 6.3. The two instruments providing rf signals are in the top left of the picture, the signal generator Rohde&Schwarz SMA100B serving as a pump and the VNA Agilent E5071C. Their outputs (port 1 for the VNA) are coupled through a directional coupler (bandwidth $2 \div 18$ GHz) and directed into the same rf line going down in the cryostat, with the VNA signal passing in the "coupled" port of the directional coupler, being attenuated of 10 dB. The different temperature stages of the dilution refrigerator are shown with the dashed lines. The input rf line is interrupted with a 30 dB power attenuator at 600 mK and with another 30 dB attenuator at 10 mK, to reduce the thermal power coming from the hottest plates and environments and to avoid an overload of the JJ. Before reaching the junction, the input line encounters a double-junction cryogenic circulator (bandwidth $8 \div 12$ GHz), for which its four ports are numbered in the picture. The fourth port is terminated with a 50 Ω load. The first part of the circulator (ports 4 and 1) avoids reflected power from the JJ to return back on the input line, while the second part (ports 2 and 3) avoids that the junction is contaminated with noise power coming from the output line, which is damped on the 50 Ω load. The microwave signals reach the single port of the JJ through a bias tee (indicated as BT in Fig. 6.3), which allows to simultaneously feed the junction with rf and dc. Finally, the reflected power from the JJ is directed up to the output line; we use the fifth custom rf line described in Sec. 4.3.2 for this purpose. Here, the HEMT at the 4 K stage and the FET at room temperature give a total amplification of 60 dB. Then, the splitter ("Spl." in the figure) equally divides the output power: one half is sent to the second port of the VNA for S_{21} measurements and one half to the Signal Hound SM200B spectrum analyzer for power spectrum measurements.

Additionally, dc wires are present to bring the current bias to the junction. The positive pole enters in the inductive port of the bias tee and then feeds the junction, while the negative pole is connected to the bias tee grounding. To avoid rf contamination on the dc lines, emi filters are used; in particular LC filters at 300 K with 1 MHz bandwidth, RCR filters at 4 K and metal powder filters at 10 mK.

To screen the Josephson junction from the Earth's magnetic field, it is placed inside a lead can, as can be seen in Fig. 6.4.

Calibration of the used rf lines has to be done in order to precisely characterize the attenuation of the input line and the total gain of the output line. This is necessary to know the actual power fed to the junction and the actual power reflected by it. Since it is not possible to measure the single line components when the system is cooled, we carried out a custom calibration procedure, which has to be repeated at every measurement. In the following the calibration is described, but some additional details are reported in Appendix C.

The calibration is performed thanks to the S_{21} measurements in a dedicated cooling, in which no sample is mounted and two additional lines are used. The diagram of this calibration setup is reported in Fig. 6.5. A directional coupler followed by an rf switch allows all the possible S_{21} combinations between the lines. We call the total S_{21} parameters by Mij, with i the line connected to the VNA and j the line connected to the readout port. The single lines are Li, i from 1 to 5, with clear reference to Fig. 6.5. The procedure consists of the following steps:

- at 300 K we measure the total S_{21} parameters of all the combinations, $M12$, $M23$, $M25$, $M15$, $M13$, $M35$, and separately all the single lines $L1$, $L2$, $L3$, $L5$. To all this measures, the contribution of the external measurement cables is subtracted, apart from $L5$, which includes the external output cable. Then, the lines $L1$ to $L5$ are obtained from the solutions (C.2) to the system (C.1), starting only from the experimental Mij. These solutions are compared with the previously measured $L1$, $L2$, $L3$, $L5$, as in Fig. 6.6, to verify the validity of the solving method. From the comparison, we see that the obtained values agree with the measured ones within about 1 dB, therefore we take this value as a reasonable uncertainty on the subsequent estimations. As a further check, B is also calculated from the equations and results in about -10 dB within the error, as expected.

- As a second step, the system schematized in diagram 6.5 is cooled to 4 K and the mea-

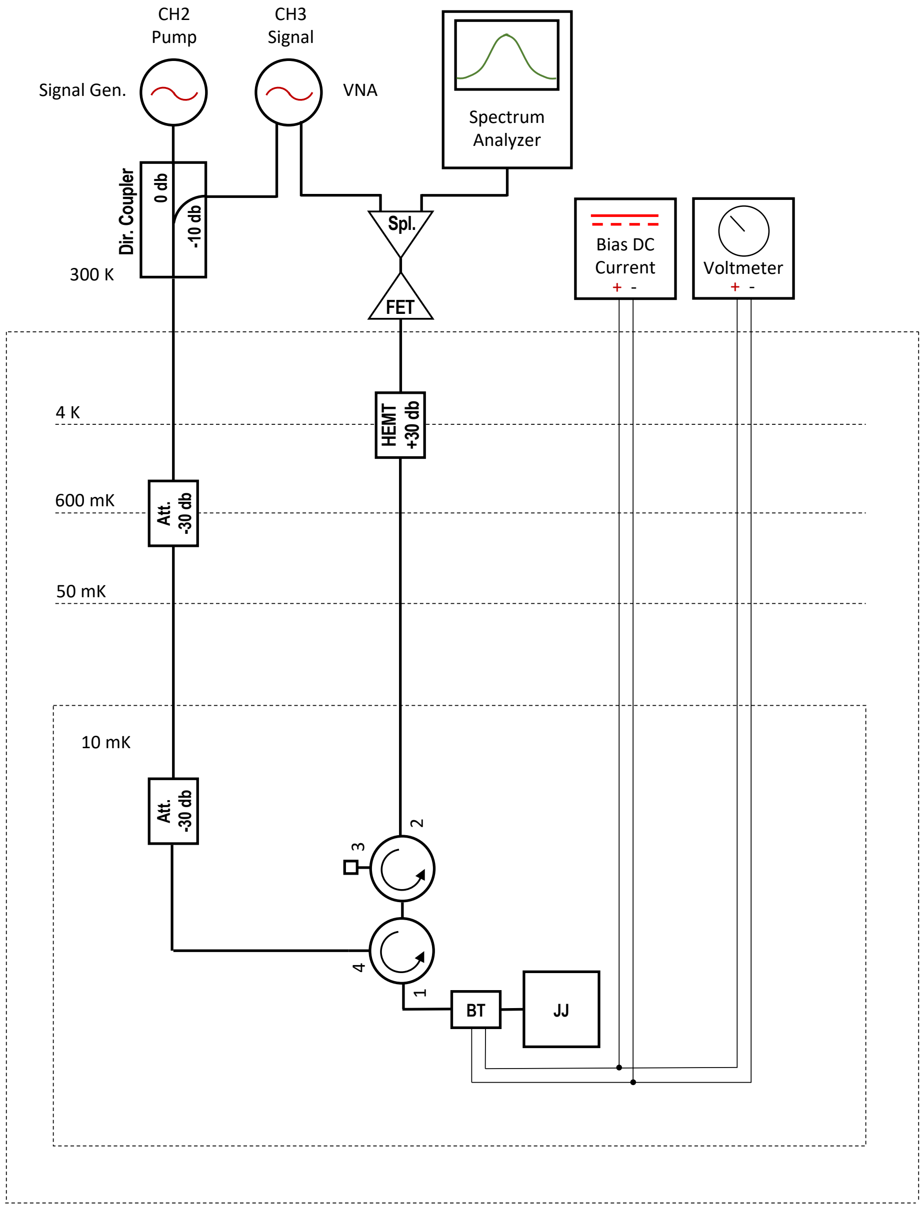

Figure 6.3: Schematic diagram of the rf wiring for the junction characterization. All attenuations and gains are indicated in dB units. Dc lines are also included in the picture. Refer to the text for a detailed description.

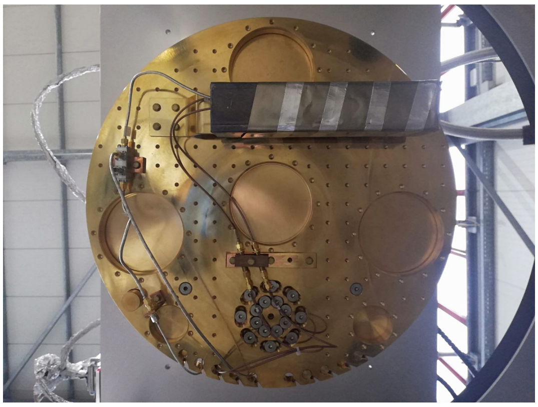

Figure 6.4: Bottom view of the 10 mK plate of the dilution refrigerator, where the sample is placed. The JJ is housed inside the Pb screen at the top of the picture. On the left, the double circulator is also visible, while at the center there are the metal powder filters for the dc lines.

surement of all the total S_{21} parameters is repeated. Starting from them, using again the solutions (C.2), the attenuations of the lines at 4 K are obtained. These are shown in Fig. 6.7, in comparison with the previously measured line attenuations at 300 K. The difference with the room temperature values is due to the change of the cables' resistivities with temperature, that gives an improvement to all the lines at 4 K, but the main improvement in lines $L2$ and $L5$ is ascribed to the presence of superconducting parts. We also checked the solution for B at 4 K, giving again -10 dB and confirming that the directional coupler is properly working even at cryogenic temperatures.

- The plots in Fig. 6.7 are the attenuations and the gain solved for the calibration run of diagram 6.5. Now, they have to be corrected to reconstruct the actual values of the $L2$ and $L5$ lines used to characterize the rf junction (diagram 6.3), and this is done by accounting for the differences in the setups. The differences during the rf junction characterization consisted in the presence of attenuators on the $L2$ line, assumed to be frequency independent and equal to -60 dB, the absence of the switch, different rf cables on the 10 mK plate and different measurement cables at 300 K. The different cables at 10 mK and the attenuation given by the switch are measured at room temperature, and then estimated at 10 mK considering a correction of 1 dB.

  The obtained $L5$ line defines the effective gain at the output of the junction, from the circulator to the VNA, including the splitter and one measurement cable, and is shown in Fig. 6.8 in the range $(5 \div 15)$ GHz. As a first approximation we can consider the gain constant between 5 and 12 GHz and equal to

$$G_5 = (49.5 \pm 1.0)\ \text{dB}. \tag{6.1}$$

  Summing the $L5$ gain profile with the corrected $L2$ line, the expected S_{21} that should

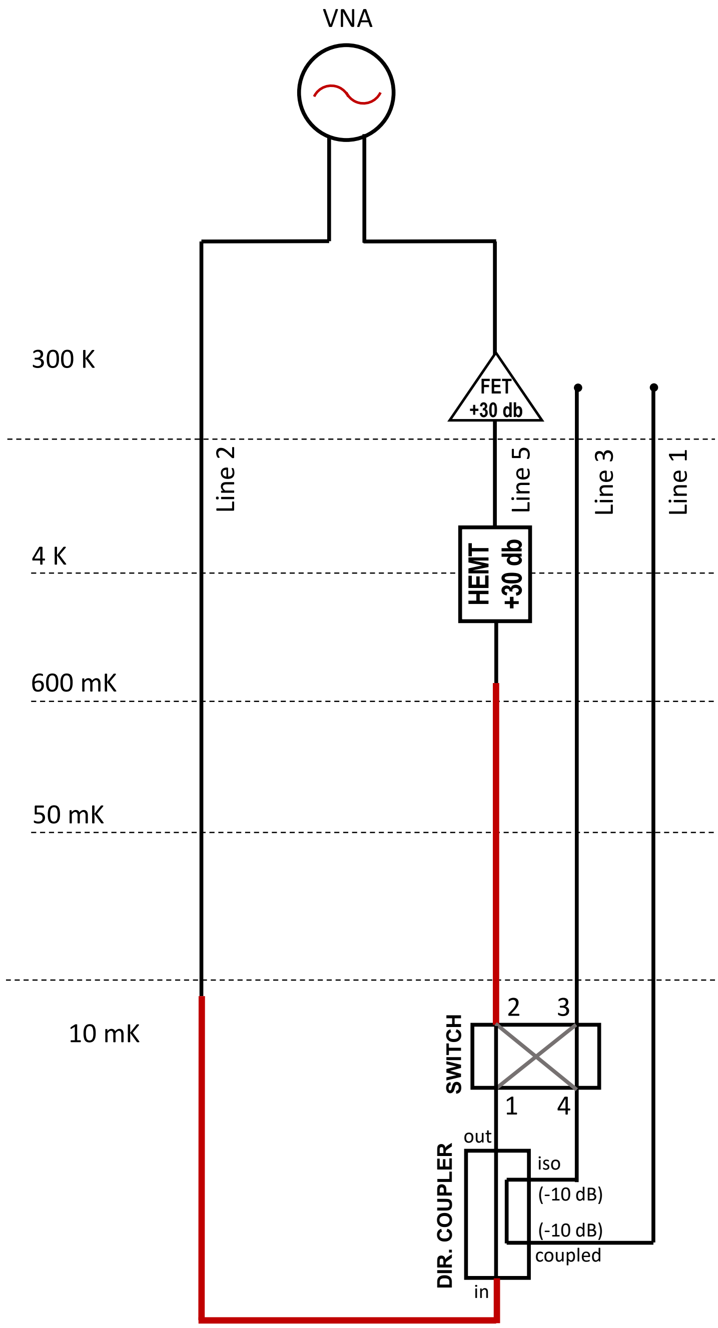

Figure 6.5: Diagram of the rf setup during the dedicated run to calibrate the rf lines. The parts in red indicate superconductive cables, that at low temperatures give no attenuation.

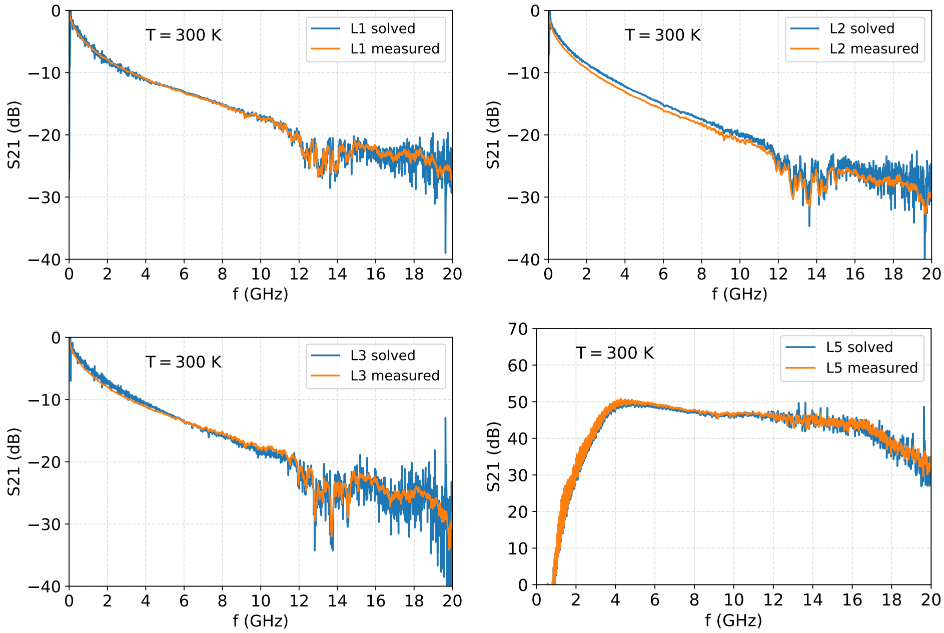

Figure 6.6: Comparison between the calculated rf lines and the measured ones at 300 K.

be measured from the VNA is obtained, as in the left picture of Fig. 6.9. Unfortunately, the actual S_{21} measured during the rf characterization is quite different, as can be seen in the right picture of Fig. 6.9 (in orange). The high peaks at about 7 and 13 GHz are due to a malfunctioning of the attenuator at 10 mK, as verified later in dedicated measurements. However, the measured and expected S_{21} curves between 8 and 11 GHz, where the attenuator is working properly, are at the same level. Due to this issue, we limited the junction rf characterizations to the region between 8 and 12 GHz.

In the final step, we calibrate the actual attenuation of the pump branch of the $L2$ line by subtracting the $L5$ effective gain and summing the difference between the VNA and pump branches of $L2$ from the measured S_{21} shown in the right picture of Fig. 6.9. The pump-VNA difference stands in the different coupling of the directional coupler and different measurement cables to the instruments. The resulting $L2$ pump attenuation is reported in Fig. 6.10. This curve is used to correct all the power values generated by the signal generator to precisely know the actual power which drives the junction. As a reference, the overall attenuation around 10 GHz is between -80 and -85 dB. Note again that the uncertainty associated to these estimations is of ± 1 dB.

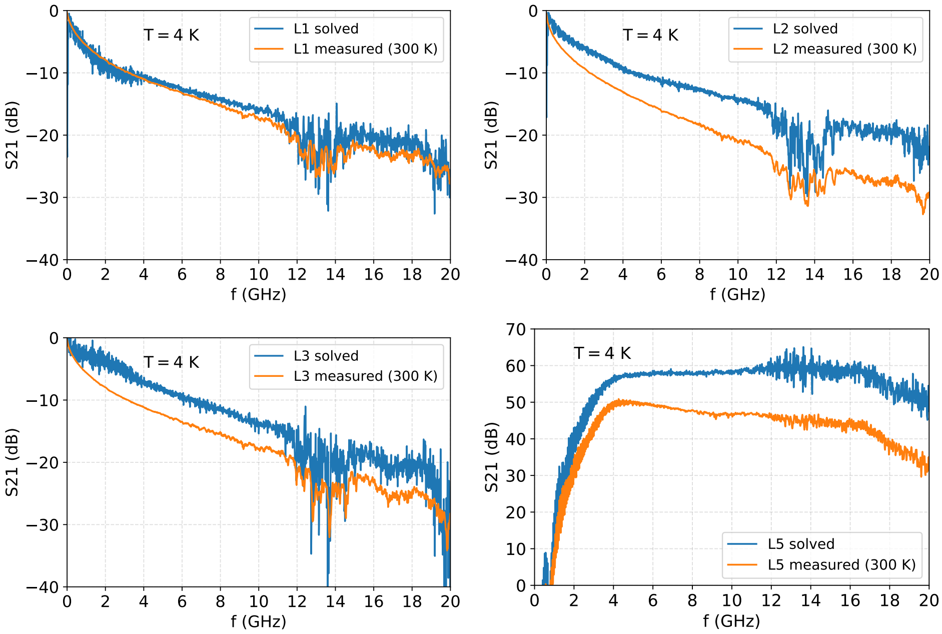

Figure 6.7: Comparison between the calculated rf lines at 4 K and the measured ones at 300 K. The $L1$ and $L3$ differences are only due to the change in resistivity with temperature, while in $L2$ and $L5$ superconducting parts play a role.

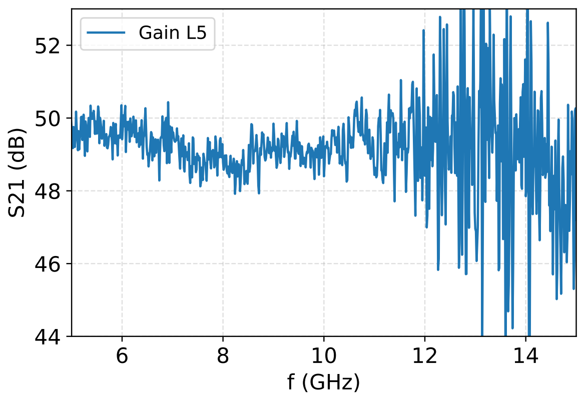

Figure 6.8: Effective gain of the output $L5$ line during the rf characterization of the junction from 5 to 15 GHz. We take a mean value of (49.5 ± 1.0) dB as a reference.

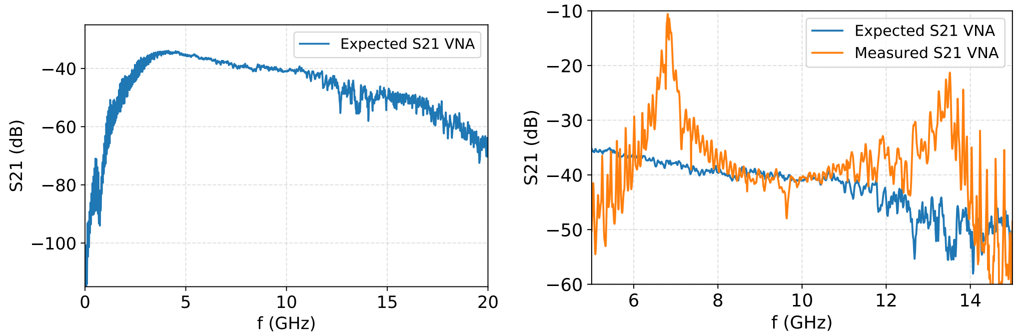

Figure 6.9: *Left)* Expected S_{21} obtained as the sum of the corrected $L2$ and $L5$ lines. *Right)* Comparison between the expected S_{21} (blue) and the measured one (orange) during the rf characterization of the junction (refer to diagram 6.3).

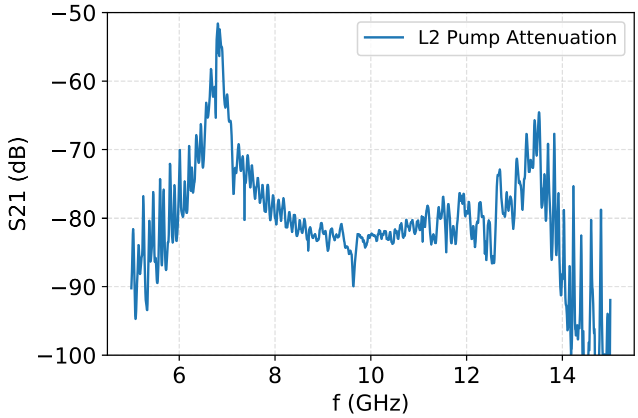

Figure 6.10: Calibrated attenuation of the pump line going from the signal generator to the junction, from 5 to 15 GHz.

6.2 Parameters estimation

IV characterization

Before starting with the rf characterization of the junction in the next sections, here I summarize the I-V measurements done with low frequency signals, fed to the junction through the dc lines of diagram 6.3. These are coupled to the junction through the inductive port of the bias tee.

The current-voltage room-temperature electronics scheme is very similar to that of Fig. 5.7. We send a voltage signal with a Keysight 33500B waveform generator on a bias resistance $R = 99.5\ \text{k}\Omega$, the current sent and the voltage read are both amplified by low-noise Stanford SR560 preamplifiers ($4\ \text{nV}/\sqrt{\text{Hz}}$) and acquired by a NI USB 6366 acquisition board. The I-V characteristic shown in Fig. 6.11 is obtained by sending a saw-tooth waveform with repetition rate 0.117 Hz and applying 3 kHz low-pass filters to the amplifiers to reduce electrical noise. From this, the normal resistance, the voltage gap and an estimate of the critical current

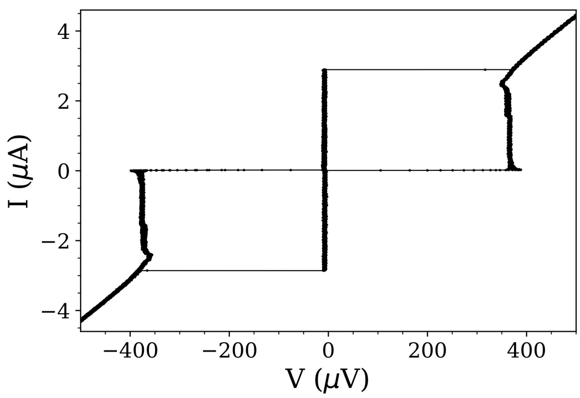

Figure 6.11: Measured current-voltage characteristic of the 8 μm^2 Josephson junction.

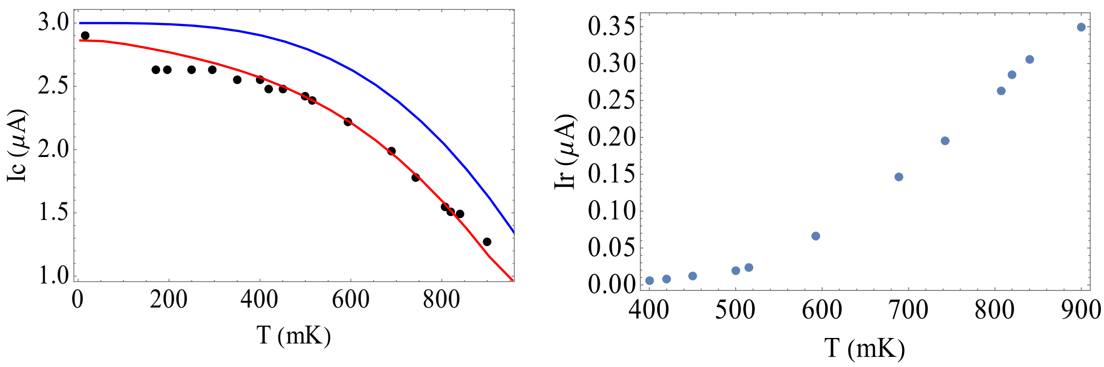

Figure 6.12: *Left)* Critical current behavior as a function of temperature. The black dots are experimental points, the blue curve is a plot of Eq. (6.2) with $I_c(0) = 3\ \mu$A and $T_c = 1.2$ K, while the red curve shows the reduction of the critical currents due to escape mechanisms. *Right)* Retrapping current as a function of temperature. Below 400 mK, the I_r values are zero.

are obtained, being respectively $R_N = 105\ \Omega$, $V_{\text{gap}} = 380\ \mu$V and $I_c \simeq 3.0\ \mu$A. The values are compatible with the Ambegaokar-Baratoff formula (see Eq. (2.3)) giving the expected critical current at zero temperature, $I_0(0) = (\pi/4)V_{\text{gap}}/R_N$.

During a heating due to some thermal instability, we took the chance to measure I-V characteristics at growing temperatures. From them, we reconstructed the critical current behavior as a function of temperature, from 16 mK to 900 mK (black dots in the left plot of Fig. 6.12). The points are fit by the expression reported in [120]:

$$I_c(T) = I_c(0)\left(1 - \left(\frac{T}{T_c}\right)^{10/3}\right)^{5/4} \tag{6.2}$$

but this gives $I_c(0) = 2.66\ \mu$A and $T_c = 1.12$ K as parameters, instead of the measured critical current and the expected transition temperature of 1.20 K for aluminum. The reason can be attributed to the effect that escape mechanisms have on the reduction of the critical current value, and this is verified by the blue and red lines in Fig. 6.12 (left). The blue line

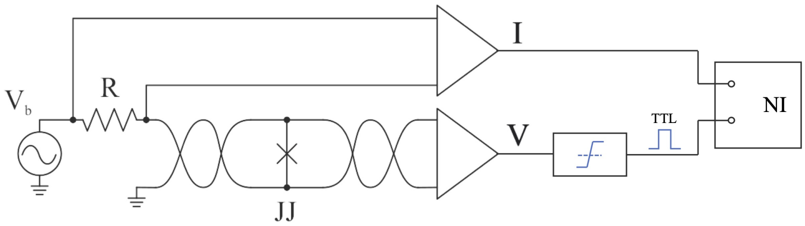

Figure 6.13: Scheme of the current and voltage readout for escape measurements. NI indicates the NI USB 6366 acquisition board.

represents equation (6.2) with the values $I_c(0) = 3\ \mu$A and $T_c = 1.2$ K, while the red curve is the behavior of the mean values $\langle I_c \rangle$ taken from escape distributions with a simple Kramers form (2.14) as a function of temperature. The latter shows a good agreement with data.

We also measured the values of the retrapping current (mentioned in Subsec. 2.1.2) as a function of temperature, shown in the right plot of Fig. 6.12. As expected, the thermal fluctuations affect the retrapping current by increasing its value above the unfluctuated one (2.10), as the temperature increases.

Escape in the absence of microwaves

Here, the switching process in the absence of radiofrequency is investigated. This method allows to independently evaluate the parameters of the junction, such as its critical current, capacity and escape temperature.

The room-temperature electronics is the same as for the I-V measurements (Sec. 6.2), with the only difference that now the voltage read from the junction is sent to a voltage comparator, as shown in Fig. 6.13. When the voltage is higher than the set threshold, the comparator generates a TTL signal that is fed to the acquisition board, and the current at which this happens is acquired. The switching currents are collected sending a saw-tooth waveform with repetition rate 314 Hz and ramp rate $\mathrm{d}I/\mathrm{d}t = 3.27$ mA/s. The $N = 10000$ acquired values are collected in a histogram, which is normalized dividing each bin by $N\,\Delta I$, where ΔI is the bin width, giving the probability density $f(I)$ of Fig. 6.14.

To extract the parameters, the points are fit with the following expression for the distribution:

$$f(I) = \frac{\Gamma_{\mathrm{esc}}(I)}{\mathrm{d}I/\mathrm{d}t} \exp\left(-\int_0^I \frac{\Gamma_{\mathrm{esc}}(I')}{\mathrm{d}I/\mathrm{d}t}\mathrm{d}I'\right), \tag{6.3}$$

where Γ_{esc} is the general escape distribution introduced in equation (2.19), but with a further prefactor, in particular the "intermediate-low damping" prefactor of equation (2.15). The result is the continuous line in Fig. 6.14 and the parameters obtained from the fit are $I_c = 3.19\ \mu$A and $T_{\mathrm{esc}} = 200$ mK, keeping the capacity fixed to $C = 2$ pF. However, the fit is not much sensitive to the choise of C, and repeating it with $C = 1$ pF does not significantly change the result. Note that, as anticipated before, the switching current approach is a more

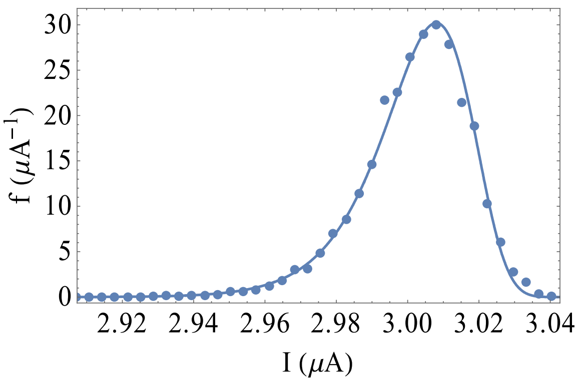

Figure 6.14: Experimental escape probability density distribution (points) and theoretical model fit to the data (solid line).

reliable method to evaluate the critical current than the estimation from IV curves.

Also, the obtained escape temperature is quite high, given that the mixing chamber physical temperature is $T = 16$ mK and the expected crossover temperature from quantum to classical regime is $T_{cr} \simeq 120$ mK. This is likely due to an excess of thermal noise coming from the rf lines, given the malfunctioning of the attenuators. However, in general, the thermal noise in the system was not fully understood; in fact, upon repeating escape measurements, we obtain T_{esc} values oscillating between 120 mK to 200 mK.

Plasma frequency

The plasma frequency of a Josephson junction can also be found by looking at its resonance frequency on a VNA and how it changes when I_b is varied, as the current dependence of equation (2.12) suggests. A region around 12.2 GHz was individuated when changing the bias from 0 to 1.8 μA, as Fig. 6.15 shows. The left plot is the "unwrapped" phase of the VNA signal as a function of the frequency at zero bias. Here, the phase is not limited to vary from 0 to 2π and is indicated in degrees; each resonance should correspond to a 180° step. In the middle of the plot there is a resonance at about 9.8 GHz, probably due to reflections in the cables, since it appears even when the junction is in the normal state. Then, above 12 GHz, there is a phase slip of about 1080° which is sensitive to the current; this is attributed to the Josephson junction. In fact, the plot on the right shows the change in the phase when different biases are applied. The pronounced phase slip in this region is also due to other resonances, as the one at about 12.4 GHz in Fig. 6.15 (right), attributed to the sample holder. As the junction resonance peak at zero bias, we consider the central frequency seen at 12.387 GHz, marked with a red circle in the left plot, and the resonance width is about 1 GHz.

The expression of the plasma frequency at zero bias is $f_{p0} = \sqrt{2eI_c/\hbar C}/2\pi$ (from Eq. (2.8)). Using the value of $I_c = 3.19\ \mu$A found in the previous subsection, the capacity of the junction

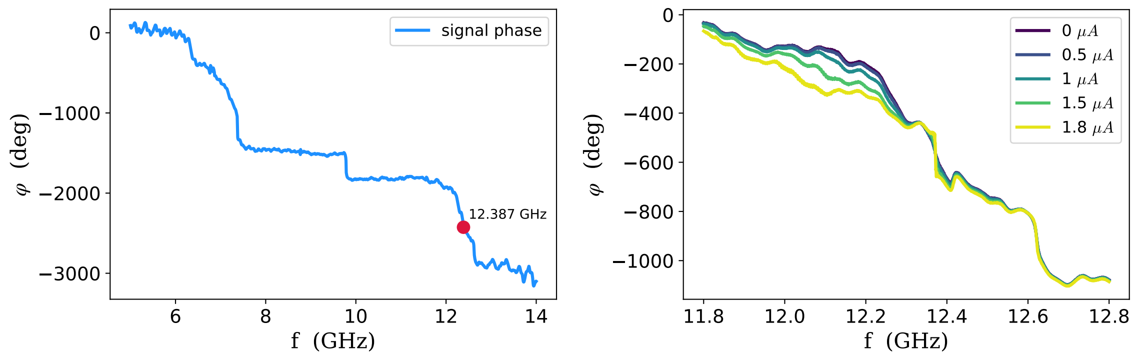

Figure 6.15: *Left*) "Unwrapped" phase of the VNA signal reflected by the junction as a function of frequency. The red circle shows the individuated junction resonance at zero bias. *Right*) Same as *Left*, from 11.8 to 12.8 GHz and for different biases.

is about $C = 1.6$ pF. Note that this is a quite rough estimation, due to the low precision of the frequency determination in Fig. 6.15; however, we can state that the capacity of our junction lies between 1 pF and 2 pF.

6.2.1 Josephson parametric amplifier

As a further characterization, we managed to use the Josephson junction as a parametric amplifier. This is a single-junction four-wave mixer, where the amplification is given by the Kerr term.

Experimental setup

This measurement has been performed in a different run with respect to the rf characterization described in the rest of this Chapter. The diagram of the rf lines is the same as in Fig. 6.3, but with the difference that two superconducting cables were mounted, one from the attenuator placed at 10 mK in the input line to the port 4 of the first circulator, and one in the output line, from the 10 mK stage to the 600 mK stage. Therefore, the calibration procedure described in subsection 6.1.2 has been repeated.

The calibrated gain of the $L5$ output line at the VNA and at the spectrum analyzer are shown in Fig. 6.16, respectively form 5 to 15 GHz and from 10 to 13 GHz. The difference resides in two different measurement cables used after the splitter. The gain estimate gives the following values:

$$\begin{aligned} G_5 &= (52 \pm 1)\ \text{dB} && \text{to VNA} \\ G_5 &= (50 \pm 1)\ \text{dB} && \text{to Spectrum Analyzer.} \end{aligned} \tag{6.4}$$

The attenuation of the $L2$ pump line is obtained in the same way as in Fig. 6.10, but sub-

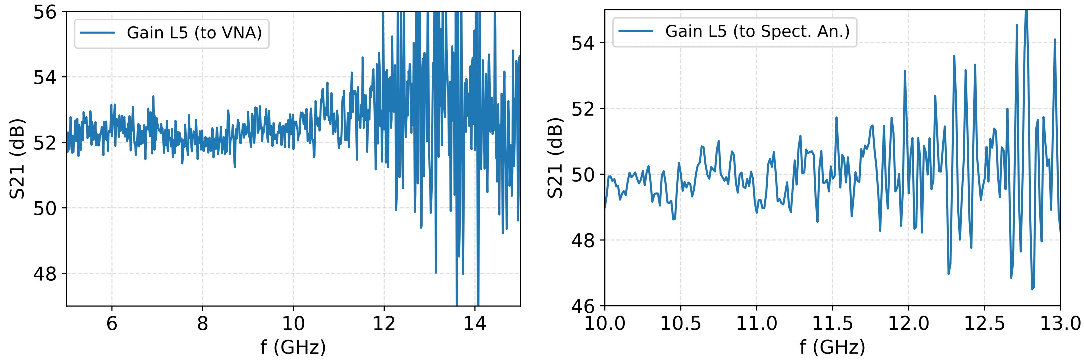

Figure 6.16: Calibrated gain of the $L5$ output line from the junction to the VNA (*Left*) and from the junction to the spectrum analyzer (*Right*), for the measurements of the junction used as a parametric amplifier.

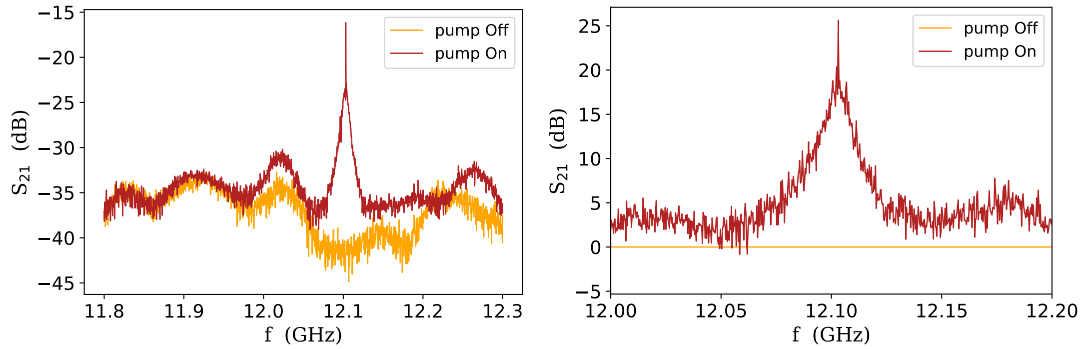

Figure 6.17: *Left*) S_{21} parameter from the VNA with $P_{\mathrm{VNA}} = -115$ dBm and pump signal at $\nu_{\mathrm{rf}} = 12.1031$ GHz and $P_{\mathrm{rf}} = -89$ dBm (red); the data with pump off is also shown (orange). *Right*) Relative gain of the single-junction JPA, obtained subtracting the pump-on and pump-off data.

tracting the new $L5$ effective gain (52 dB instead of 49.5 dB). This is used, again, to calibrate the power values of the signal generator to give the actual power at the junction input.

Gain and noise performances

As a starting point, we searched for the JPA resonance with a VNA frequency sweep, at different pump frequency and power values. One of the found resonances is shown in Fig. 6.17 (red), at pump frequency 12.1031 GHz and power -89 dBm at the junction input. As a reference, in the left plot the S_{21} profile with pump off is also reported (orange data). Then, the difference between the pump-on and pump-off data has been performed, as reported in Fig. 6.17 (right). From the resonance peak, the relative gain with the aforementioned stimulus conditions results in about 20 dB, while the linewidth (evaluated at -3 dB from the maximum) is about 10 MHz, giving the amplification bandwidth. Note that the frequency of operation of the JPA is near the plasma frequency estimated in the previous subsection.

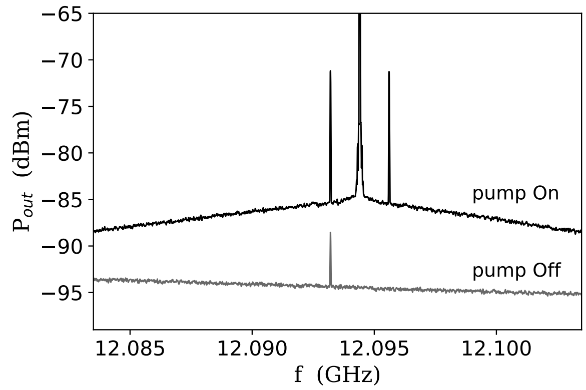

Figure 6.18: Pump off (grey) and pump on (black) output spectra with the signal from the VNA at a frequency $\nu_s = 12.0932$ GHz and power $P_s = -130$ dBm, and with pump frequency $\nu_{rf} = 12.0944$ GHz and power $P_{rf} = -88.5$ dBm. The peak at 12.0956 GHz is the idler frequency.

Many other resonance peaks were found at different frequencies around 12 GHz and different pump values, not shown here, which gave amplification values up to 20 dB.

Then, the JPA gain and noise were measured with the spectrum analyzer. The VNA was set to the continuous wave mode, with a frequency $\nu_{\text{VNA}} = 12.0932$ GHz and power $P_{\text{VNA}} = -130$ dBm, while the pump was set to $\nu_{rf} = 12.0944$ GHz. The measurements were performed again with the pump on-pump off method, at different values of pump power. An example of the output spectrum at $P_{rf} = -88.5$ dBm is given in Fig. 6.18: the grey data are the output spectrum while the pump is switched off, and the only peak is the signal frequency from the VNA; the black data are the spectrum with pump on, and besides the signal, the pump frequency can be seen and the idler is present at a frequency mirroring the signal peak. The background is also amplified by the JPA.

From the background of the pump-off data it is possible to measure the HEMT noise temperature, being the only active device in the output line to add noise when the JPA is switched off. The background level is taken to the immediate left of the signal and is -94.6 dBm. The noise temperature is calculated using equation (4.2), where here $\Delta\nu$ is the instrument resolution bandwidth (RBW) set to 3×10^4 kHz, while the measured noise power is referred to the HEMT input by subtracting the $L5$ effective gain $G_5^{\text{spect.}}$ (Eq. (6.4)). Passing from dB units to linear units, the estimated HEMT noise temperature is

$$T_n^{\text{HEMT}} \simeq 8.4 \text{ K}. \tag{6.5}$$

The JPA gain is obtained by measuring the signal peak absolute power with pump on and then with pump off. The result for different pump power values is shown in Fig. 6.19 (left): with this stimulus conditions, the maximum observed JPA gain is about 18 dB. The noise temperature is shown in Fig. 6.19 (right) and is calculated from Eq. (4.2), referring the

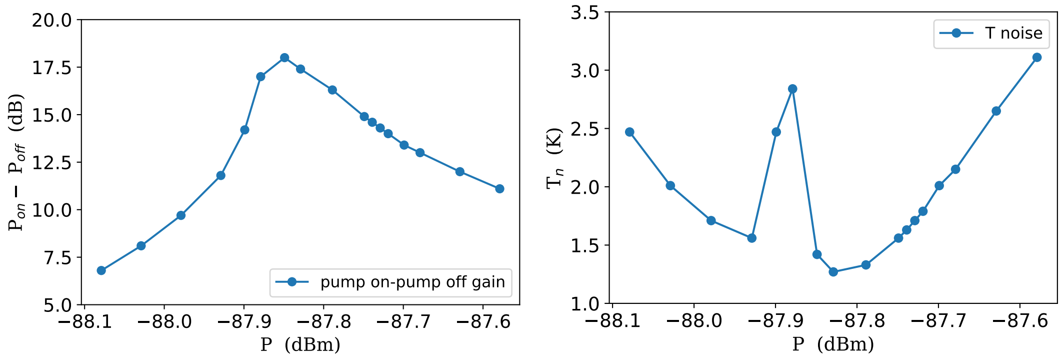

Figure 6.19: *Left*) Single-junction JPA gain obtained with the pump on-pump off method as a function of the pump power. *Right*) JPA noise temperature as a function of the pump power.

noise power to the JPA input by dividing by its gain. The minimum noise temperature is about 1.3 K. The two points above 2.5 K correspond to regions in which the background was highly amplified, giving a very bad signal-to-noise ratio. In that case the Josephson amplifier becomes unstable and behaves as an oscillator. Actually, Fig. 6.19(right) is the noise temperature of the JPA plus HEMT amplification chain. An estimation of the noise only due to the JPA (at the point with maximum gain and minimum noise temperature) can be done by subtracting the HEMT noise referred to the JPA input:

$$T_n^{\text{JPA}} = 1.3\,\text{K} - 8.4\,\text{K}/10^{18/10} = 1.17\,\text{K}\,. \tag{6.6}$$

This indicates that the amount of noise is two quanta, since the obtained temperature is twice the standard quantum limit at 12 GHz, $T_{\text{SQL}} \simeq 580$ mK.

6.3 Resonant activation

After the investigation of the escape mechanism without applied radiofrequency, described in Sec. 6.2, we also measure the junction response in the presence of continuous rf waves. The resonant activation is seen in IV-characteristics in the presence of microwaves and in escape measurements. The escape rates are obtained in different configurations of bias currents and rf excitations.

The resonance condition is fulfilled when the energy of incoming photons makes the superconducting phase φ of the junction oscillate. In terms of the quantized potential picture (see Fig. 5.2), resonant incoming photons excite the JJ to the first (E_1) or subsequent (E_n) excited energy levels. Note, however, that the condition has to be considered semiclassically. In fact, as will be shown, the de-excitation time is of order $50-100$ ps and then the bandwidth of the levels is very large, more than 1 GHz. Moreover, our noise temperature is greater than the crossover temperature (see Sec. 6.2), so that quantum escape and thermal activation

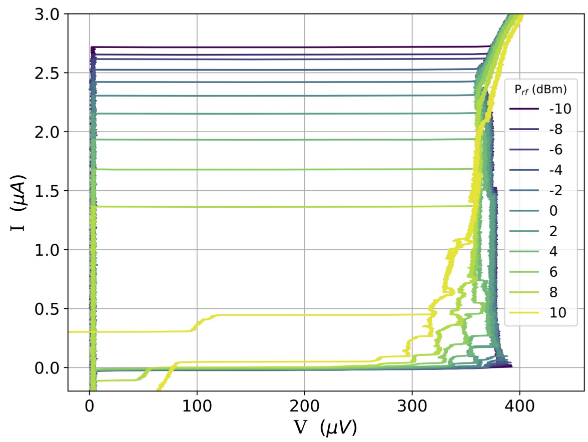

Figure 6.20: Current-voltage characteristics of the junction for different pump powers at a pump frequency of $\nu_{\rm rf} = 8$ GHz. In the legend, the power values from the signal generator are reported.

processes coexist.

6.3.1 IV in the presence of microwaves

The measurement setup is the same as for the low-frequency IV characterization, but now continuous radiofrequency is sent to the junction from the signal generator through the rf pump line.

We expect that the presence of microwaves reduces the current at which the JJ switches to the normal state. In fact, this is shown in Fig. 6.20, where the IV characteristics are plotted for increasing pump power values, at the frequency $\nu_{\rm rf} = 8$ GHz. In this figure, the steps corresponding to the photon assisted tunneling process (Sec. 2.4) are also present, visible at voltage values of about $V_{\rm gap}$ when the bias current is returned to zero.

The current-voltage plots are acquired for different pump frequencies, always with the same power range from the generator. The results of the switching currents vs. the pump power values are shown in Fig. 6.21. As can be seen, the microwaves facilitate the switching process.

6.3.2 Escape in the presence of microwaves

The collection of the switching currents happens with the same logic described in the escape measurements in the absence of microwaves (Sec. 6.2), with the difference that now continuous rf signals are injected in the pump line while the junction is dc-biased. Microwaves are coupled to the capacitive port of the bias tee and reach the junction through the Al coplanar waveguide.

The presence of microwaves facilitates the escape process, in particular when the rf frequency is in resonance with the plasma frequency of the junction. In this case, we expect

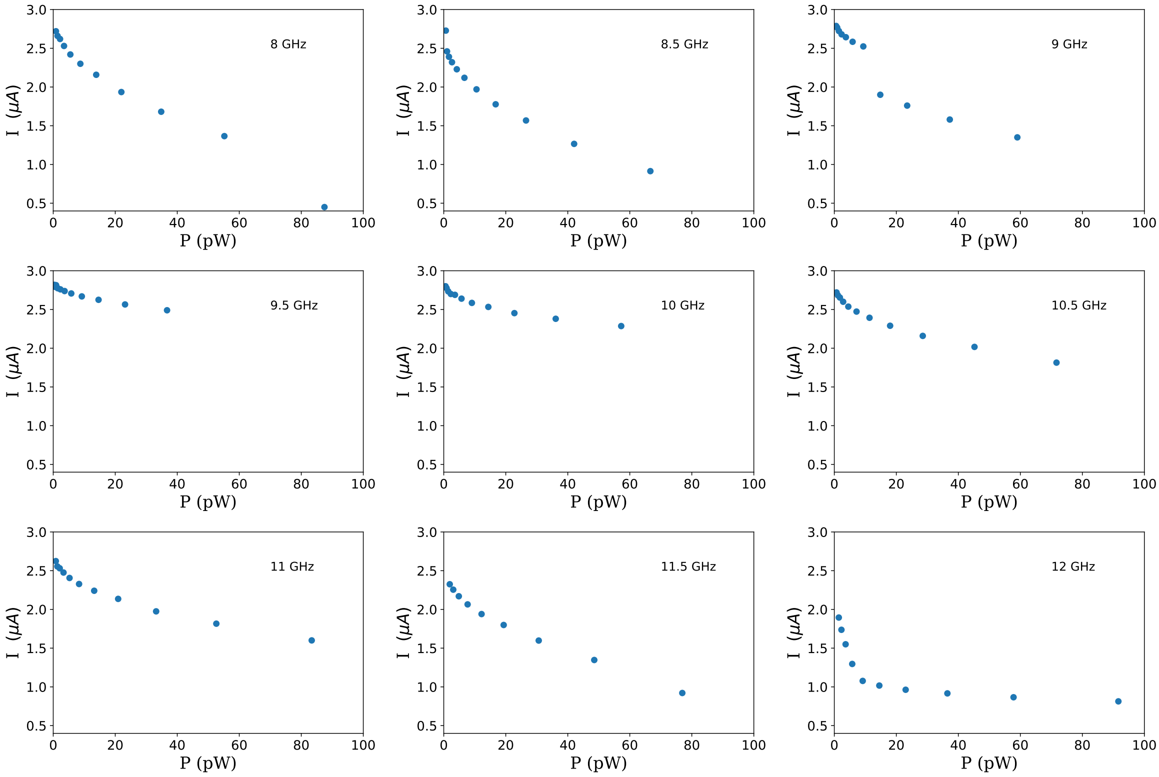

Figure 6.21: Switching currents vs. applied rf power in linear units, measured from the IV characteristics for various rf frequencies.

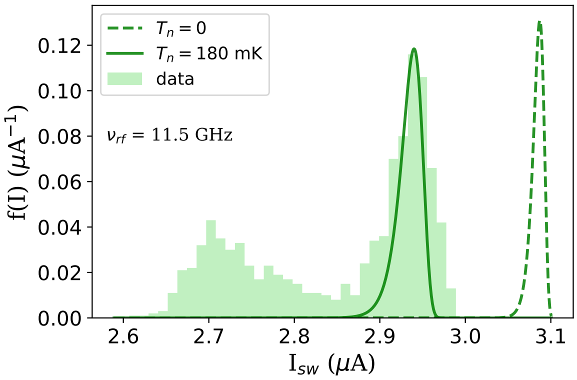

Figure 6.22: Switching distribution vs. bias current for $\nu_{\mathrm{rf}} = 11.5$ GHz and $P_{\mathrm{rf}} = -98$ dBm (histogram). The peak on the left is due to the resonant activation and the one on the right to the thermal escape. Also shown are the predicted escape rates without thermal noise (dotted line) and with $T_n = 180$ mK (solid line).

escape events occurring at currents well below the critical current. An example is shown in the escape probability distribution of Fig. 6.22, for $\nu_{\mathrm{rf}} = 11.5$ GHz and $P_{\mathrm{rf}} = -98$ dBm. The tallest histogram peak is related to the natural escape process, which is also measured without microwaves, while the smallest and broadest histogram peak on the left indicates a resonant activation process. In the same figure, the dotted line represents the expected escape distribution in the absence of microwaves and with zero thermal noise, while the solid curve is the predicted thermal escape rate with $T_n = 180$ mK, overlapping with the experimental peak and confirming that the system temperature is near 200 mK as estimated in Sec. 6.2.

For appropriate values in the rf frequency and power parameter space, we observe the sudden reduction of the switching current, as in Fig. 6.23. The points in the plot are the experimental escape distributions obtained from the data of the switching currents using equation (2.22). The different colors are related to different rf conditions, as indicated by the frequency values and number of photons in the plot. As in Fig. 6.22, the right peaks are related to thermal escapes, while the left peaks are due to premature switchings caused by the presence of microwaves. Therefore, from these distributions the resonant activation is clearly visible at different stimulus conditions. The solid curves in the plot are a model describing the escape process when rf is applied to the junction.

Before describing those theoretical curves, we discuss the frequencies at which resonant activation occurs. We measure the positions on the x-axis of the resonant peaks of Fig. 6.23 and relate them to the applied microwave frequencies, giving the behavior of frequency vs bias current shown by the points in the plot of Fig. 6.24. Their behavior is not consistent with the expression of the current-dependent plasma frequency of Eq. (2.12), which is only valid for small oscillations. The reason is that the incoming microwaves cause the junction phase to perform wide oscillations necessary to induce the escape, so that the quadratic potential

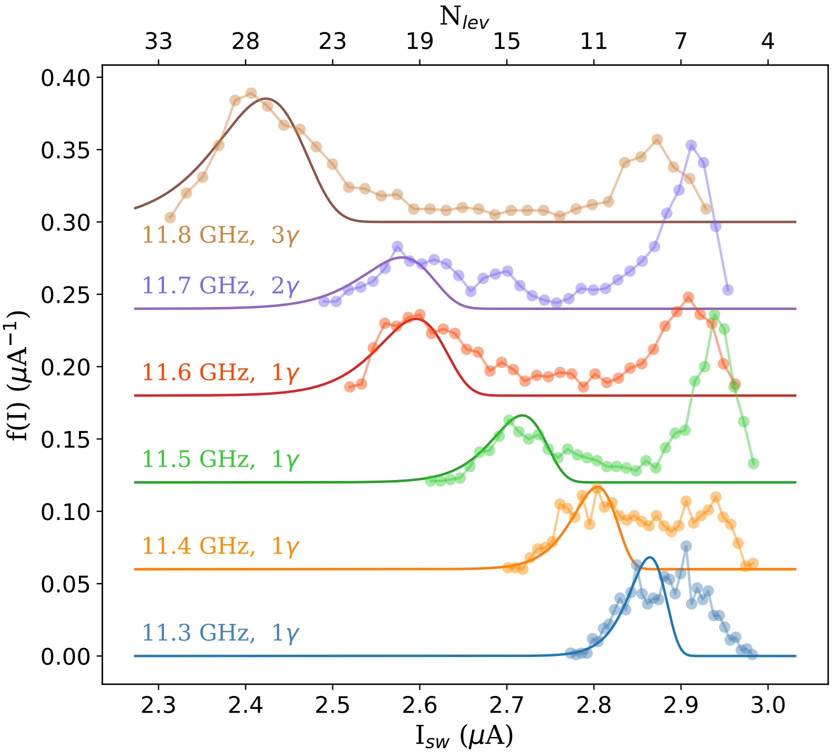

Figure 6.23: Escape distributions vs. bias current in the presence of microwaves. The points are experimental data, the frequency and number of photons corresponding to the rf power are indicated on the left. The solid curves are the expected switching distributions in the presence of microwaves, calculated with escape rates given by Eq. (6.9).

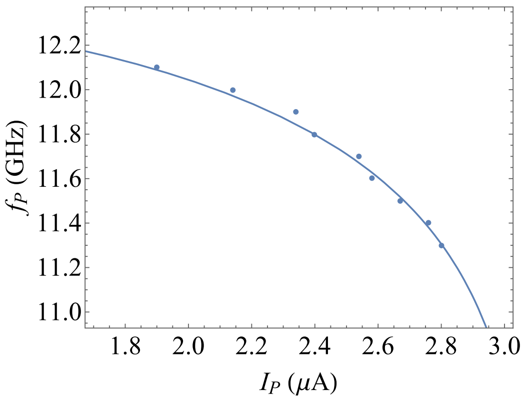

Figure 6.24: Measured position (current and frequency) of the observed resonant peaks (points) and expected behavior in the anharmonic case (line).

approximation is no more reliable.

To model the anharmonicity effects on the potential, numerical simulations of the junction dynamics with applied microwaves are performed, solving the CBJJ equations with initial total energy E_0 for the phase particle and by studying the oscillation frequency under the different rf conditions. An empirical expression for the modified plasma frequency, valid for a bias $\alpha = I_b/I_c > 0.6$, is

$$f_{\text{eff}}(\alpha) \simeq \frac{\omega_{p0}}{2\pi} \left(1-\alpha^2\right)^{1/4} \left(1 - \frac{E_0}{\Delta U(\alpha)}\right)^{0.13}, \tag{6.7}$$

similar to Eq. (2.12) with a correction depending on the amplitude of the oscillations. Now, the effect of noise and/or tunneling on the switching is described as an effective reduction ΔE of the barrier height $\Delta U(\alpha)$, so that the switching can occur when the energy of the system is $E_0 \geq \Delta U - \Delta E$. By substituting this expression in Eq. (6.7) and considering the barrier height approximation $\Delta U \simeq (2/3)E_J(1-\alpha^2)^{3/2}$ when α is close to 1, the expression becomes

$$f_{\text{eff}}(\alpha) \simeq \frac{\omega_{p0}}{2\pi} \left(\frac{3}{2}\frac{\Delta E}{E_J}\right)^{0.13} \left(1-\alpha^2\right)^{0.055}, \tag{6.8}$$

We interpret $f_{\text{eff}}(\alpha)$ as the modified current-dependent plasma frequency in the case of anharmonic oscillations. The model is shown as the curve in Fig. 6.24, giving a good agreement with the data points. The best fit is obtained with the parameters $I_c = 3.2\ \mu A$, $C = 1$ pF and $\Delta E/E_J = 0.094$.

Now the theoretical escape distributions in the presence of microwaves in Fig. 6.23 can be treated. Following Devoret et al. [133], the escape rate accounting for the microwave irradiation can be modified as

$$\Gamma_{\mathrm{esc}}(P_{\mathrm{rf}}) = a_t \frac{\omega_{\mathrm{eff}}(\alpha)}{2\pi} \exp\left(-\frac{\Delta U(\alpha)}{k_B T + E_L}\right), \tag{6.9}$$
$$E_L = \frac{P_{\mathrm{rf}}}{Q\omega_{\mathrm{eff}}} \frac{1}{[1-(\omega_{\mathrm{rf}}/\omega_{\mathrm{eff}})^2]^2 + (\omega_{\mathrm{rf}}/Q\omega_{\mathrm{eff}})^2},$$

where E_L is the energy provided to the Josephson inductance by a power P_{rf} and is summed to $k_B T$ as to increase the system temperature. In place of the plasma frequency ω_p, we use the modified frequency obtained in Eq. (6.8), so that $\omega_{\mathrm{eff}}(\alpha) = 2\pi f_{\mathrm{eff}}(\alpha)$. The switching distributions are obtained from the escape rates using Eq. (6.3). The curves reproducing the data are plotted as solid lines in Fig. 6.23 and give a good agreement. The parameters used in this case are $I_c = 3.2\ \mu$A, $C = 1$ pF, $\mathrm{d}I/\mathrm{d}t = 9.6$ mA/s, T is the physical temperature of 15 mK with additional noise of $T_n = 180$ mK and for the prefactor a_t the intermediate-low damping expression of Eq. (2.15) is used.

Note that, as reported in Fig. 6.23, the rf power values reaching the junction correspond to the absorption of one or few photons within the JJ decay time $\tau = RC = 50$ ps, where $R = Z_{TL}$ is the 50 Ω impedance of the TL and $C = 1$ pF. This is the time available to a photon to interact with the junction before it is reflected. Therefore, the number of photons in a time τ is calculated as

$$N_\gamma = \frac{P_{\mathrm{rf}}\tau}{\hbar\omega_{\mathrm{rf}}}. \tag{6.10}$$

In the resonant peaks, P_{rf} is the minimum detectable power at each given frequency. At 11.5 GHz, the corrected incident power of -98 dBm corresponds to 1.5×10^{-13} W, and translates into a photon flux of 20 photons/ns. The peaks measured with these low power values are clearly visible, so the CBJJ seems to be sensitive to one or few photons, while the number of levels in the well is greater. This happens because the continuous rf sent to the junction gives an enhancement effect on the switching process, even if $N_\gamma < N_{\mathrm{lev}}$, causing an effective increase of the temperature as can be seen in the first row of Eq. (6.9), where E_L is summed to $k_B T$.

6.4 Pulsed measurements

Here, measurements of the lifetime of the Josephson junction in the presence of microwaves are described. These allow again to obtain escape rates at different biases and rf excitations, but in a configuration that comes closer to sending a single photon. In fact, a series of rf current pulses with constant amplitude I_b and small duration Δt_{p} are applied, and during the time Δt_{p} the junction has a certain probability to switch.

6.4.1 Technical implementation

The electronics logic is very similar to the setups previously described, as the escape measurements, but now the rf signal generator has to be properly triggered. The arbitrary waveform generated by the Keysight 33500B to current-bias the junction is shown in yellow in Fig. 6.25, which gives an oscilloscope visualization of the signals involved during lifetime measurements. The waveform consists in a first ramp until the desired bias value is reached, after which the current is maintained constant. Then, the current is ramped down to some small negative value to make the junction return to the superconducting state, and the cycle repeats. A TTL signal is generated by the Keysight 33500B at the end of the current rump-up and triggers the signal generator Rohde&Schwarz SMA100B. The trigger is also sent to the acquisition board NI USB 6366 to start to count time. After 7 ms from the trigger, the Rohde&Schwarz sends an rf pulse modulated by a rectangular shape of the desired duration and height (green signal in Fig. 6.25). When the junction switches, its voltage raises (blue in the Figure) and from the voltage comparator another TTL is generated and acquired (red in the Figure); this constitutes an event.

As can be seen from the Fig. 6.25, the junction has three chances to switch: before the rf pulse, when the bias is sufficiently high to make the escape due to thermal or quantum fluctuations effective; during the pulse, for the effect of the applied microwaves; after the pulse, again caused by thermal or quantum fluctuations, but after some inefficiency effect occurred during the pulse application.

The collected lifetime values are defined as the time interval between the first TTL and the second TTL, i.e. the time at which the junction has switched measured starting from the end of the current ramp-up. It might happen that due to a small bias, the escape rate is very low and several ramps are required for an event to occur. To avoid infinite loops in the software, a timeout is set: if after 10 cycles no lifetime is collected, the process is stopped. As a result, the maximum measurable lifetime is limited to ten times the period of current cycles. Other informations are also written on a metadata file, useful for the data analysis, as the total number of current cycles, the number of cycles in which the junction has switched and the number of empty cycles (no event occurred at all).

6.4.2 Junction lifetime measurements

The aforementioned switching times are collected in histograms to give the junction lifetimes, useful to extract parameters characterizing the junction. Every run starts with the lifetime measurement in the absence of radiofrequency, giving a pure exponential behavior, shown in Fig. 6.26(left). The histogram is fit with the simple exponential

$$\Delta N(t) = \frac{N_0 \delta t}{\tau} e^{-t/\tau}, \tag{6.11}$$

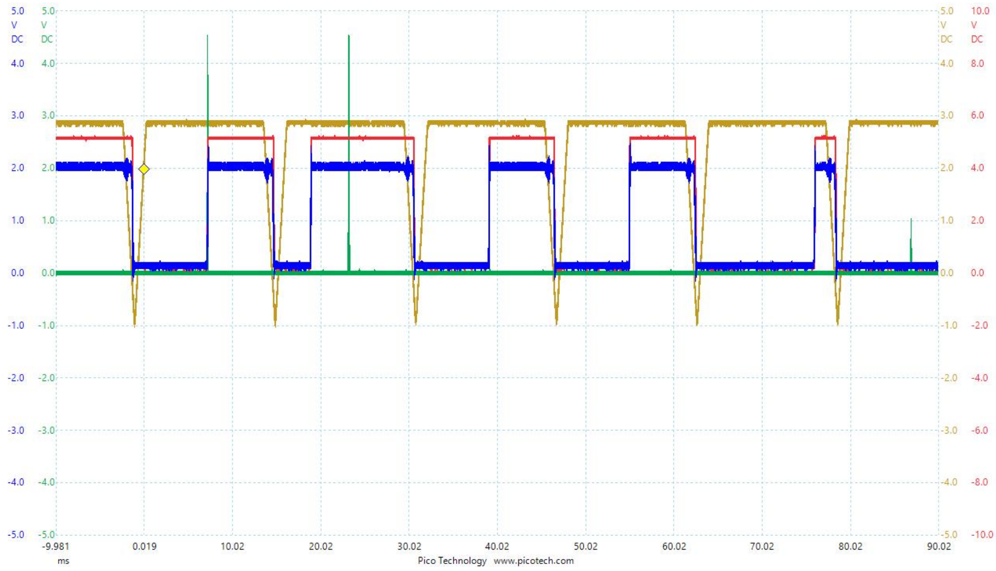

Figure 6.25: Signals involved in the pulsed measurements of the junction lifetime, visualized on a PicoScope digital oscilloscope. Yellow indicates the bias current arbitrary waveform, blue is the voltage across the junction, which undergoes a sudden change from zero to a finite value when the junction switches, red is the TTL signal accompanying the JJ voltage above a certain threshold, and green is the 10 ns rf pulse starting 7 ms after the current has reached its maximum value. The current ramps have repetition rate of 62.8 Hz. Note that the rf pulse is always present in all the cycles, but due to the oscilloscope slow samplings on this timescales it is not always visible on screen.

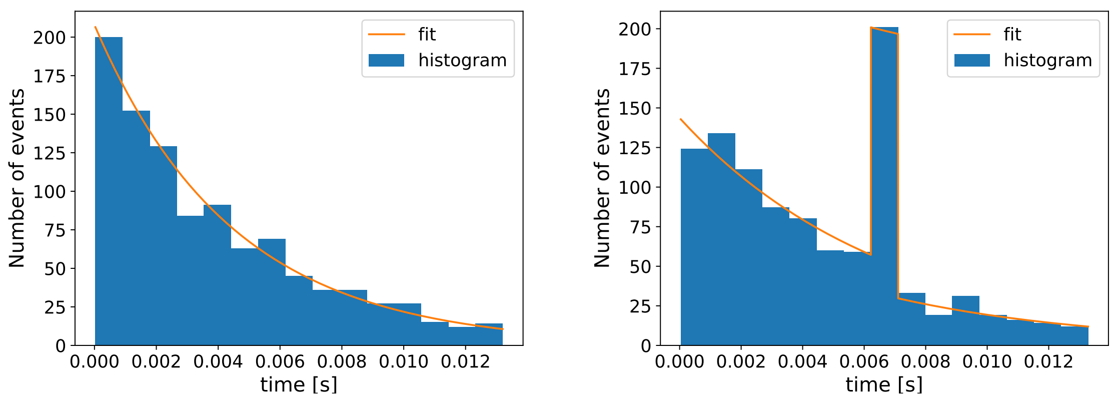

Figure 6.26: *Left*) Distribution of switching times in the absence of rf, fitted by the exponential (6.11). *Right*) Distribution of switching times in the presence of rf, fitted with the formula of Eq. (6.13).

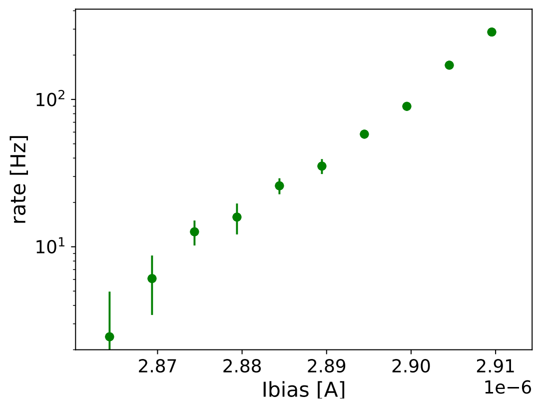

Figure 6.27: Thermal escape rate as a function of the bias current, obtained from the lifetime measurements.

where δt is the bin width and $N_0\delta t/\tau$ is the height of the first bin. From each of these plots, the escape rate without rf is obtained, $\Gamma = 1/\tau$, and this is repeated for each value of the current bias I_b. As a result, the dependence of $\Gamma(I)$ is extracted in the investigated bias range. An example of escape rate in the absence of rf from lifetime measurements is given in Fig. 6.27. Fitting this escape rate with a Kramers model (2.14), one can again obtain an estimation of the critical current I_c and escape temperature T_{esc}, while keeping the capacity fixed. Typical values are $I_c = (3.150 \pm 0.015)\ \mu$A and $T_{\text{esc}} = (180 \pm 15)$ mK, with $C = 1.6$ pF. The procedure is repeated for every run, having different I_b ranges, and Fig. 6.27 is only one example.

Subsequently, the lifetimes in the presence of microwaves are explored. A histogram is shown in Fig. 6.26(right), where the moment in which the rf pulse occurs is clearly visible. In our measurements, the rf pulse duration is always $\Delta t_{\text{p}} = 10$ ns and occurs 7 ms after the initial trigger. The rf bin is the most populated, since radiofrequency stimulates the switching of the junction, and the bin population after the rf pulse occurred is depleted with respect to the natural escape mechanism (plot on the left in Fig. 6.26).

To fit the lifetime in the presence of microwaves, we use the following formula:

$$\begin{aligned}\Delta N(t) = \frac{N_0\delta t}{\tau}\, e^{-t/\tau}\theta(t_{\text{rf}} - t) + \left(\frac{N_0\, e^{-t_{\text{rf}}/\tau}\delta t}{\tau} - N_{\text{rf}}\right) e^{-(t-t_{\text{rf}})/\tau}\theta(t - t_{\text{rf}}) \\ + N_{\text{rf}}\left[\theta(t - t_{\text{rf}}) - \theta(t - t_{\text{rf}} - \delta t)\right],\end{aligned} \tag{6.12}$$

or written in a more readable form:

$$\begin{aligned}\Delta N(t) = \frac{N_0\delta t}{\tau}\, e^{-t/\tau} - N_{\text{rf}}\, e^{-(t-t_{\text{rf}})/\tau}\theta(t - t_{\text{rf}}) \\ + N_{\text{rf}}\left[\theta(t - t_{\text{rf}}) - \theta(t - t_{\text{rf}} - \delta t)\right].\end{aligned} \tag{6.13}$$

In addition to the simple exponential behavior, here N_{rf} is the height of the rf bin, $t_{\text{rf}} = 7$ ms and the θs are Heaviside functions. The first contribution on the right hand side of Eq. (6.13) represents the unmodified escape behavior before the rf pulse is applied, the second term is the depleted escape behavior after the rf pulse, while the third term corresponds to the rf bin population. The extracted parameters will be used for the efficiency calculations at different stimulus conditions, as described in the next subsection.

Unfortunately, due to the high thermal noise level, we were not able to operate the junction in the same conditions as simulated in Sec. 5.1.4, where the bias values corresponded to having only 3 or 4 levels in the potential.

6.4.3 Switching efficiency

We chose to separately treat the regimes where I_b is high or low. In fact, since the background contribution is very different in the two regimes, efficiencies have to be calculated accordingly, using two different methods. In the low-bias case, indeed, the background events are completely absent and a fit to the lifetime histograms would not work.

Efficiency determination in the case of high bias currents

At high enough bias currents, the junction has a sufficiently high chance to switch, and the switching events are a combination of thermal escape and rf-stimulated escape, just like in the plot of Fig. 6.26 (right). In this case, the efficiency is calculated from the parameters extracted from the fit to the lifetimes in the presence of microwaves (equation (6.13)), namely:

$$\varepsilon = \frac{N_{\rm rf}\,\delta t}{\int_{t_{\rm rf}}^{\infty} \Delta N(t)\,\mathrm{d}t} = \frac{N_{\rm rf}\,\delta t}{N_0\,\delta t\, e^{-t_{\rm rf}/\tau}}\,. \tag{6.14}$$

The numerator is the number of events only due to radiofrequency, and is the height of the rf bin above the background level, while the denominator is the number of events that would have been present without the rf application, from $t_{\rm rf}$ to infinity.

In this regime, the efficiency has been studied as a function of the bias current, while keeping the stimulus condition fixed, and as a function of the pump power, with a particular value of frequency and I_b. Fig. 6.28 shows how the efficiency changes varying the bias current. Instead of I_b, we visualize the number of levels in the junction potential (on the upper x-axis) and the current-dependent plasma frequency (lower x-axis), given by Eq. (2.12). The number of levels in the potential well is given again by

$$N_{\rm lev} = \frac{\Delta U(I)}{\hbar\omega_p(I)}\,. \tag{6.15}$$

Inside the plots, informations about the pump frequency and number of photons reaching the junction are also included. The latter, i.e. the number of photons in a relaxation time τ,

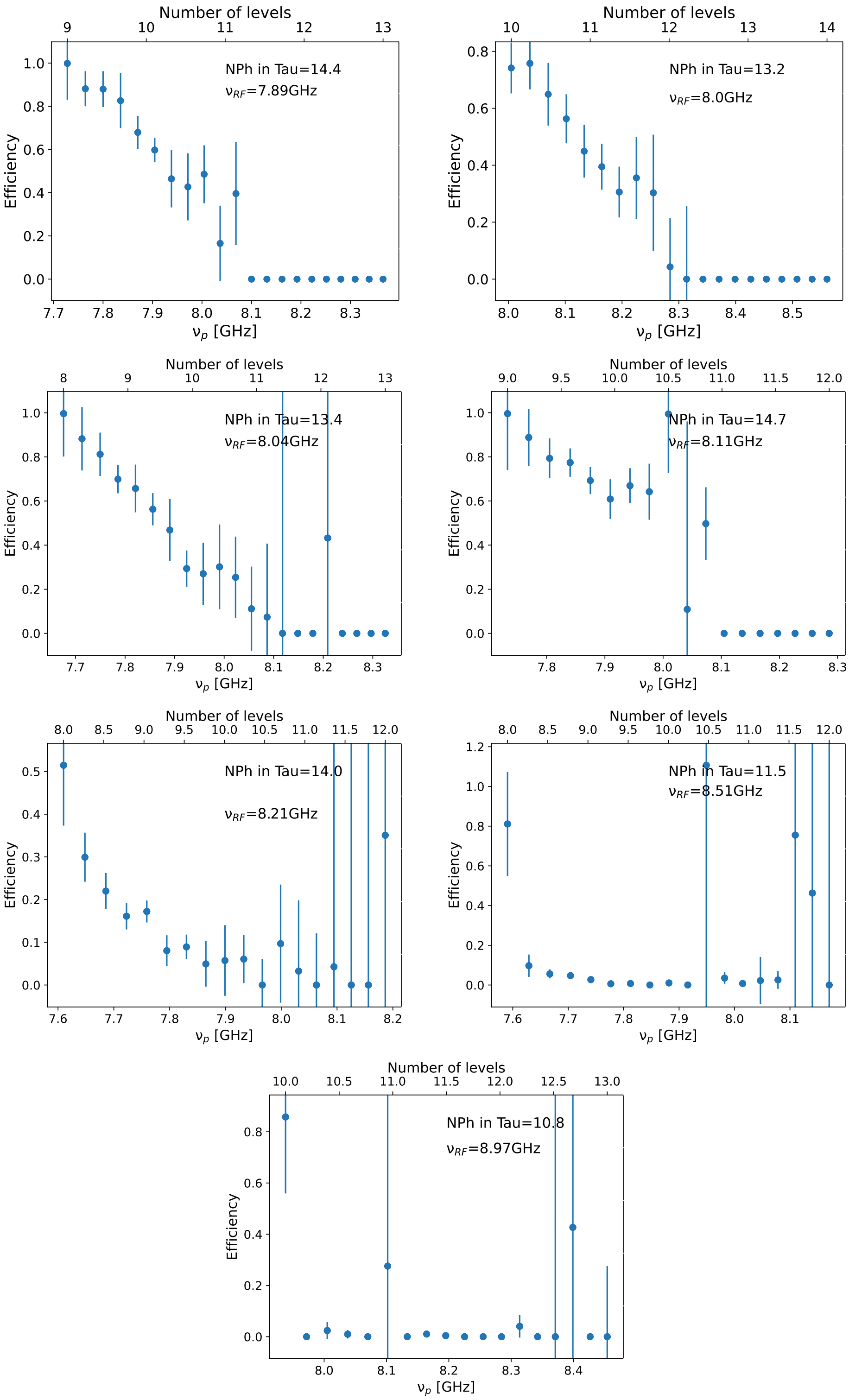

Figure 6.28: Efficiency as a function of the current bias I_b, indicated as number of levels in the potential (upper y-axis) or plasma frequency (lower x-axis). In the plots the rf frequency and the rf power, indicated as number of photons in τ, are also reported. More details in the text.

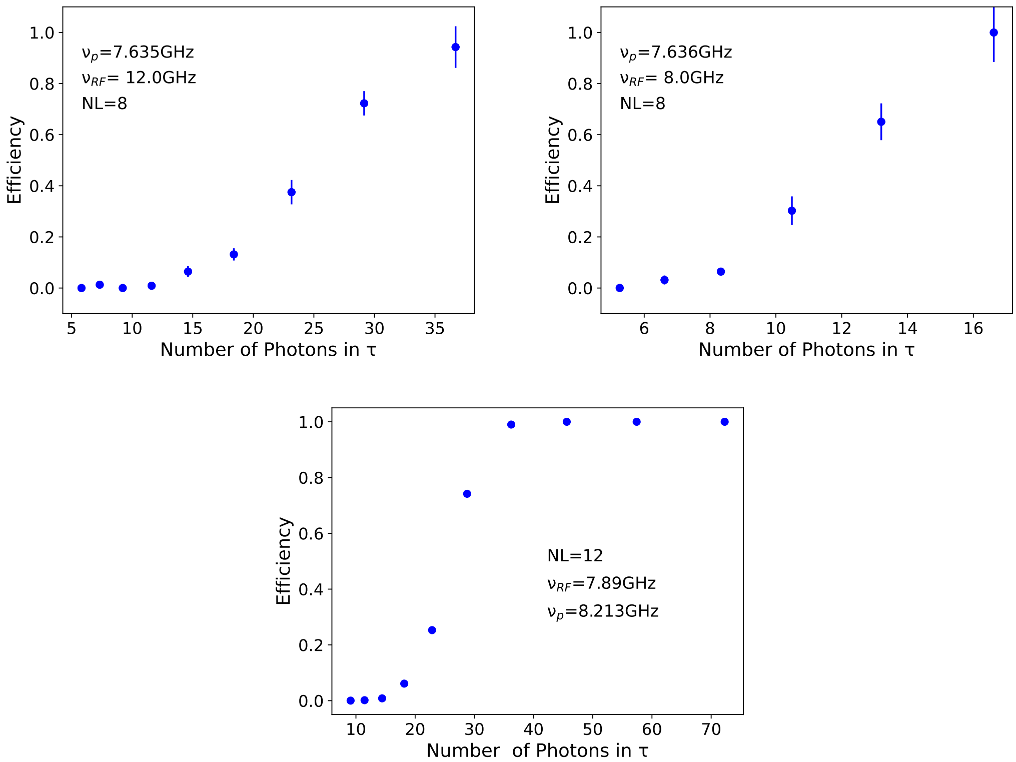

Figure 6.29: Efficiency as a function of the rf power, indicated as number of photons in τ (x-axis), at 12 GHz, 8 GHz and 7.89 GHz of pump frequency. The bias is slightly different in the lower graph, giving 12 energy levels instead of 8.

encompasses the information about the pump power, and is calculated as

$$N_\gamma = \frac{P_{\rm rf}\tau}{h\,\nu_{\rm rf}}, \tag{6.16}$$

where $\nu_{\rm rf}$ is the pump frequency and $P_{\rm rf}$ the rf power at the junction input. This is obtained by subtracting the rf line attenuation to the output power $P_{\rm gen}$ of the signal generator and converting from dBm units to Watt:

$$P_{\rm rf}\,[{\rm W}] = 10^{(P_{\rm gen}-Att.)/10} \times 10^{-3}\,{\rm W}\,. \tag{6.17}$$

Fig. 6.29 shows the efficiency as a function of the rf power, indicated again as a number of photons in τ (x-axis), at three different pump frequencies. In this case, the plasma frequency and the number of levels are fixed by the chosen bias current.

From these plots it is clear that, in the presence of pulsed rf, a very small number of photons, of the order of one or few, is not sufficient to make the junction switch. Though, this was expected from the simulations of Sec. 5.1.4 of the junction coupled to a 50 Ω transmission

Table 6.1: Values of N_γ, ν_p and N_{lev} and their uncertainties for the first six plots of Fig. 6.28, evaluated at $\varepsilon = 0.5$.

ν_{rf} (GHz)	N_γ	N_{lev} @ $\varepsilon = 0.5$	ν_p @ $\varepsilon = 0.5$ (GHz)
7.89	$14.4\pm^{3.8}_{7.3}$	10.4 ± 1.8	8.0 ± 1.7
8.00	$13.2\pm^{3.4}_{6.6}$	10.8 ± 1.9	8.0 ± 1.7
8.04	$13.4\pm^{3.5}_{6.7}$	9.6 ± 1.7	7.8 ± 1.6
8.11	$14.7\pm^{3.8}_{7.4}$	11.8 ± 2.0	8.1 ± 1.7
8.21	$14.0\pm^{3.6}_{7.1}$	8.0 ± 1.4	7.6 ± 1.6
8.51	$11.5\pm^{3.0}_{5.8}$	8.2 ± 1.4	7.6 ± 1.6

line, where a high intrinsic loss due to the TL is present. However, looking at Fig. 6.28 and Fig. 6.29 we can say that the junction is activated when $N_\gamma \approx N_{\text{lev}}$, result that was indeed expected from the simulations (Fig. 5.4). Note also that, in the plots of Fig. 6.28, when the barrier height is increased (increasing the number of levels) the efficiency drops to zero.

To motivate the claim that $N_\gamma \approx N_{\text{lev}}$, we have to consider that the values of N_γ, ν_p and N_{lev} possess significant uncertainties, since they depend on the value of the JJ capacity. In fact, while the critical current is known with good precision, some ambiguity is left to C, since the different measurements of the plasma frequency give somewhat different values. From the phase plot with zero bias (Fig. 6.15) we observe $\nu_{p0} \approx 12.3$ GHz, while a fit to the points of Fig. 6.24 with equation (2.12) would give about 15 GHz. Also, the JPA resonance is observed at a frequency near 12.1 GHz (Sec. 6.2.1). Fixing the critical current to $I_c = 3.15\ \mu$A, these values give the following range for the capacity:

$$C = (1.0 \div 1.6)\ \text{pF}\,. \tag{6.18}$$

This variability is used to give a rough estimate of the uncertainty on N_γ, ν_p and N_{lev}. Table 6.1 reports the values of these three quantities with their uncertainty for the plots of Fig. 6.28, evaluated when the efficiency is $\varepsilon = 0.5$ (apart from the last plot). The uncertainty on N_γ results from the combination of both the ambiguity on C and the uncertainty on the calibrated power P_{rf} of ± 1 dB. The central value of N_γ in the Table is calculated using $C =$ 1.6 pF.

As can be seen from the values of Table 6.1, the number of photons N_γ overlaps with N_{lev} within the errors.

Efficiency determination in the case of low bias currents

In the regime of low bias currents, the switching probability is very small and the lifetime histograms (Fig. 6.26) are empty, except for the rf bin. Therefore, in this case the efficiency is

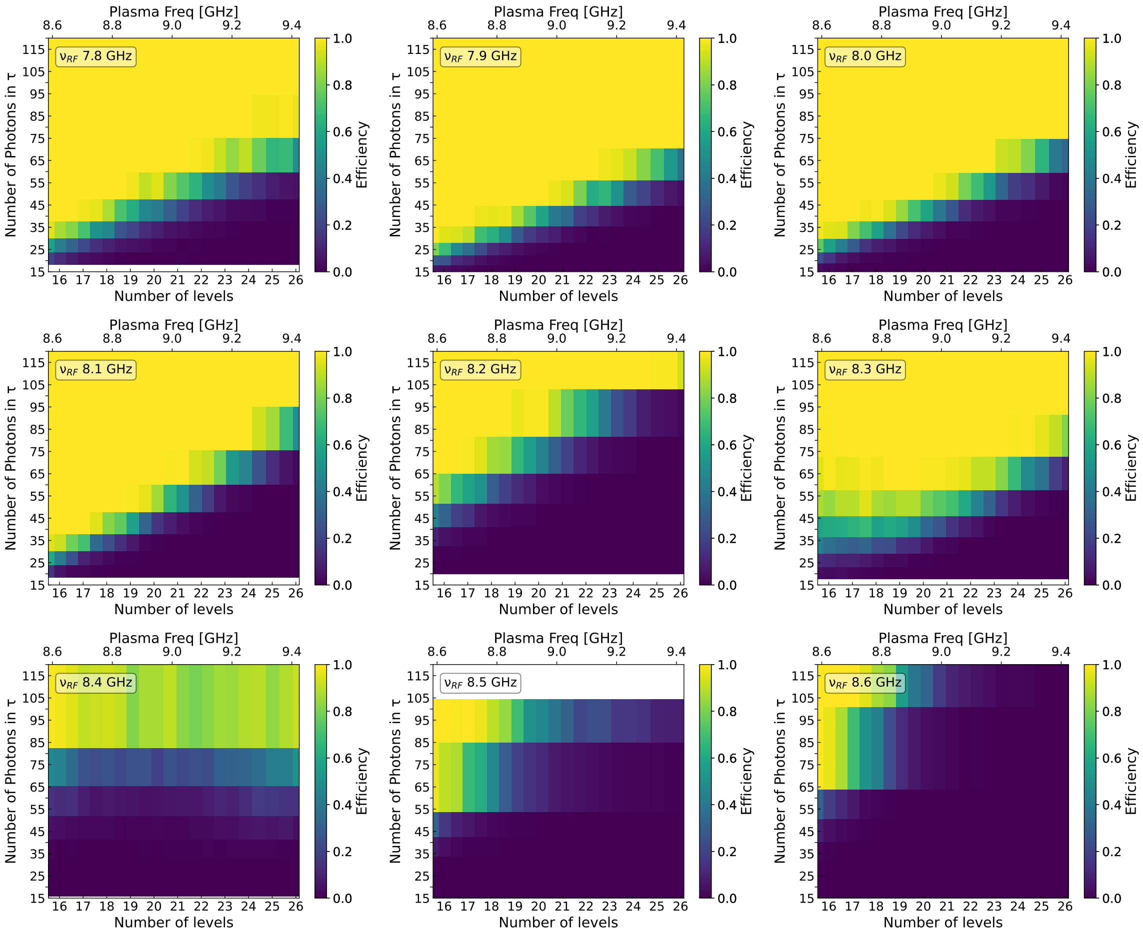

Figure 6.30: Efficiency behavior when varying I_b and P_{rf} simultaneously, at rf frequencies between 7.8 GHz and 8.6 GHz. The efficiency is coded in the colorbar, on the lower x-axis the number of levels (Eq. (6.15)) is reported and on the upper x-axis the plasma frequency is shown, while the y-axis is the number of photons in τ.

calculated as the number of switches N_{sw} normalized to the total number of trials, which also includes the number of current sweeps where we do not observe any event, N_{empty}. These numbers are taken from metadata collected in each run. The expression for the efficiency is then

$$\varepsilon = \frac{N_{sw}}{N_{sw} + N_{empty}} . \tag{6.19}$$

The colormaps of Fig. 6.30 show how the efficiency changes as a function of the bias current and the rf power, at ten different values of pump frequency. I_b gives again the number of levels in the potential (lower x-axis) and P_{rf} gives the number of photons in τ (y-axis).

For rf frequencies from 7.8 to 8.3 GHz, at the lowest values of N_{lev} the efficiencies pass from 0 to 1 when N_γ approximately matches N_{lev}. Though, when the junction barrier is increased (corresponding to increasing N_{lev}), the proportionality between the two quantities is somewhat lost. As an example, at ν_{rf} = 7.8 GHz, about 75 photons are required to have

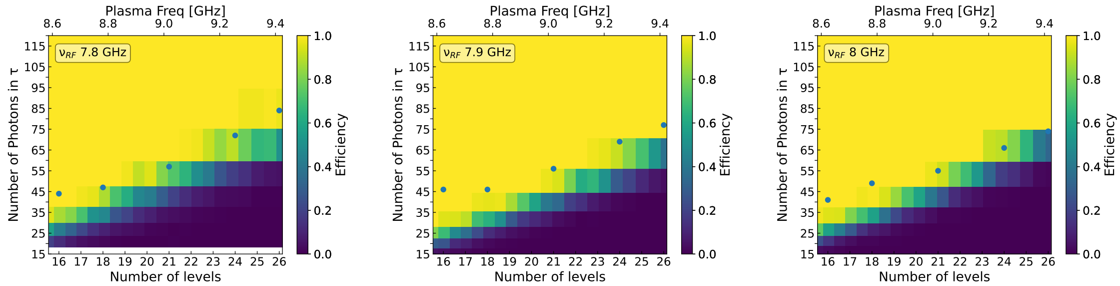

Figure 6.31: Simulations of the switching efficiencies at rf frequencies of 7.8, 7.9 and 8.0 GHz (blue dots), superimposed to the experimental plots of Fig. 6.30 at the same three frequencies.

$\varepsilon = 0.5$ with 25 levels. Then, at pump frequencies higher than 8.3 GHz, the junction seems to be less sensitive to the radiation. The behavior is not fully understood yet, and this region has to be further investigated.

To validate the results, simulations were performed in the same conditions of the data at pump frequencies of 7.8, 7.9 and 8.0 GHz. The current values at which the junction switches are simulated in the absence of noise, and the results are shown in Fig. 6.31 as blue dots. The simulations give a good agreement to the behavior of the experiment, since the points are positioned at about $\varepsilon = 0.5$. This means that the junction activation is following again the expected behavior $N_\gamma \approx N_{\text{lev}}$, at least until 8 GHz.

Switching efficiency dependence on rf pulsewidth

As a final test sending pulsed microwaves to the JJ, its response to different pulsewidths has been studied, keeping the frequency and the power fixed at $\nu_{\text{rf}} = 8$ GHz and $P_{\text{rf}} = -92.5$ dBm. The pulse duration has been changed from 10 ns to 1 μs and the lifetime measured, as usual. The switching probability as a function of the pulsewidth is reported in Fig. 6.32(left). The data points are efficiency values obtained from the fit to the time distributions, while the blue curve is a fit to the data. The model used to describe the behavior is

$$P = 1 - (1 - \epsilon)^{\Delta T/\tau}, \tag{6.20}$$

where ΔT is the pulse duration and ϵ is the switching probability in a relaxation time τ, left as a free parameter. The form of the probability P is obtained by discretizing the duration Δt in small intervals of time τ and assuming Poisson statistics for the switching events. Therefore, $(1 - \epsilon)$ is the probability that the junction does not switch to the normal state, and $\Delta T/\tau$ gives the number of independent trials within the rf pulsewidth.

For durations ΔT from 10 ns to 200 ns the curve gives a good agreement to the data, while from 200 ns to 1000 ns the data seem to define a second regime, since the model shows a small discrepancy with respect to the experimental points.

The motivation may reside in the fact that during the measurements, the experimental

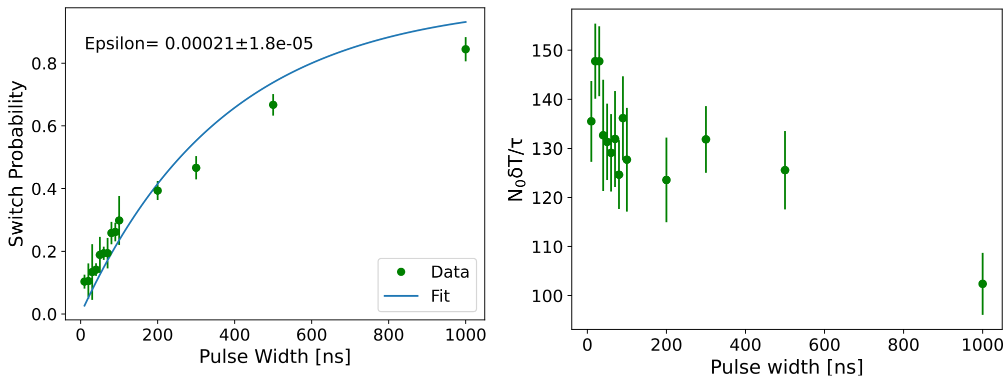

Figure 6.32: *Left*) Switching efficiency data calculated from the rf-stimulated lifetimes as a function of the pulsewidth (green points), and fit to the data (blue curve) with the model of Eq. (6.20). *Right*) Amplitude of the first bin of the lifetime distributions as a function of the rf pulsewidth.

conditions changed and the bias current reaching the junction decreased. In fact, Fig. 6.32 (right) shows the amplitude $N_0\delta t/\tau$ of the first bin of the lifetime distributions (see Eq. (6.13)), which seems to decrease going at large pulsewidths, meaning that the background in the lifetime histograms is reduced.

In conclusion, apart from experimental issues, the observed increase of the switching probability can be explained by invoking only Poisson statistics. Furthermore, we do not observe a raise in the effective temperature as in resonant activation measurements (Sec. 6.3), at least until pulsewidths of $\Delta T = 1\ \mu$s.

6.5 Summary and outlook

As a conclusion to this Chapter, we consider that we made a Josephson junction work as a photon detector, having observed a positive response to both continuous and pulsed microwaves. In the first case, one or few photons incoming within the decay time of the JJ were detected, thanks to an enhancement effect which raises the effective temperature. In the case of pulsed rf, we believe the junction is working as expected from simulations, switching when a number of photons approximately equal to the number of levels in the junction potential is absorbed, $N_\gamma \approx N_{\text{lev}}$. Moreover, we managed to exploit the nonlinear behavior of the JJ to make it work as a parametric amplifier, reaching a gain of almost 20 dB and a good noise performance, at the level of twice the standard quantum limit.

As compared to other radiation detectors, like bolometers, Josephson junctions have quite different performances. Whereas bolometers can in principle reach a better power sensitivity, but integrating energy for a long time, JJs are sensitive to lower energy values in a short time. Moreover, bolometers are subject to thermal noise, while JJs are threshold devices which in principle can operate without noise. Considering a noise equivalent power

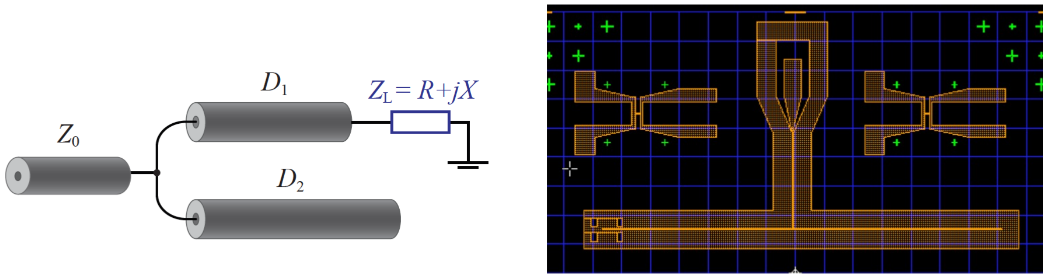

Figure 6.33: *Left*) Schematic of the stub tuner in the transmission line framework. *Right*) Design of our first stub tuner with coplanar waveguide technology.

of 10^{-19} W/$\sqrt{\text{Hz}}$ and integration times from microseconds to milliseconds, the characteristic energy sensitivities for bolometers are of the order of the zeptoJoule [134]. The record sensitivity of 1.1×10^{-21} J has been reached in a nanobolometer with a 1 μs microwave pulse at 8.4 GHz containing about 200 photons [135]. Being limited to 10 ns pulses, in our junction we reach about 10 zJ at 8 GHz, corresponding to about 3000 photons without noise. Since there is room for improvement, we expect to drop the sensitivity down to $10^{-23} - 10^{-22}$ J, showing that Josephson junctions are very promising devices on the way to reach the single photon sensitivity.

The comparison of the results with our simulations tells us that the latter are reliable. From what has been predicted and observed, it is obvious that a single-photon sensor is unfeasible when the junction is highly coupled to the transmission line, since the high damping rate caused by the 50 Ω of the latter would require a greater amount of photons than what is the requisite of single-photon detection. Clearly, an isolated junction practically does not exist, but a circuit to obtain a small coupling γ_{TL} and high relaxation time τ can be devised. A way to "decouple" the junction from the TL, as to consider it as isolated, is to design an impedance matching circuit, as the *stub tuner* [108].

A schematic of the stub tuner is given in Fig. 6.33(left), where the branch D_2 is an open transmission line and D_1 is terminated with a load Z_L, which in our case is a Josephson junction. At the node, the impedances of the two branches are summed as the parallel between the two. In a nonoptimized situation, reflections at the load input occur and propagating waves are reflected back to the TL with impedance Z_0, with subsequent loss of power. Building a matching circuit consists in tuning the length of D_1 and D_2 such that the total reactance at the load input is made null and the resistance is matched to the TL impedance Z_0. In the limit $\Re[Z_L] \gg Z_0$ (valid for a JJ), the sum of the length of the two branches is approximately $D_1 + D_2 \simeq \lambda_{\text{wg}}/2$, with λ_{wg} the wavelength in a waveguide. As a result of the impedance matching, an incoming wave is forced to oscillate back and forth between the two branches, as the reflection coefficient at the node towards Z_0 turns to be zero. The matched stub tuner thus behaves as a resonator, allowing the chance of a junction switch to enhance by a factor Q, the quality factor of the resonator. Typical values amount to a few hundreds, meaning

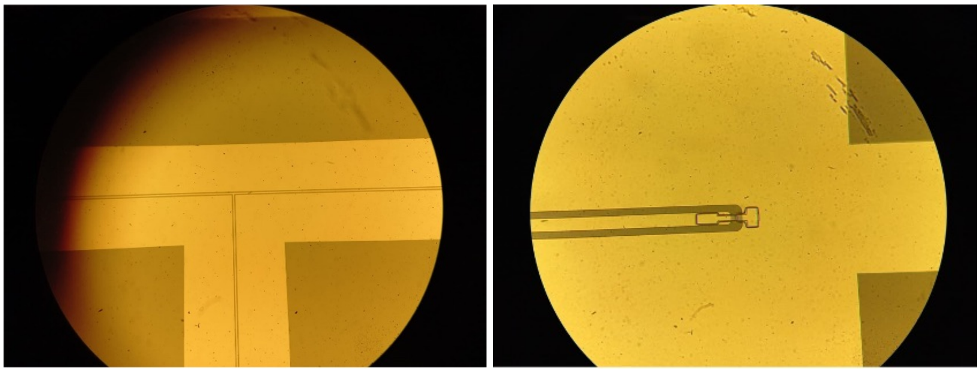

Figure 6.34: Microscope images of the fabricated stub tuner. *Left*) The ramification of the two branches. *Right*) One of the two branches terminated with a JJ.

that the decay time τ would effectively be enhanced by more than a factor 10^2. Furthermore, the intrinsic linewidth of the stub tuner, of the order of 10 MHz, would make it work as a bandpass filter, thus reducing the contribution of the Johnson noise to a small bandwidth.

We designed the first prototype of this device (Fig. 6.33 (right)), with a working frequency of about 8.4 GHz and an expected Q of about 400. It has been recently fabricated by IFN-CNR, as can be seen in Fig. 6.34. On the left the ramification of the two branches is framed, while the picture on the right shows the junction terminating one of the two branches. This is the next device to be tested, as to reach another milestone in the realization of a JJ-based photon detector.

CHAPTER 7

Conclusions

7.1 Obtained results

In Chap. 3, where the QUAX last results were shown, we demonstrated that an amplification technology involving Josephson junctions, namely Josephson parametric amplifiers, allows to reach the sensitivity down to the QCD band (Fig. 3.11), thanks to the noise at the standard quantum limit of 0.5 K at 10 GHz. In fact, the data taken with the haloscope at LNL allowed to put an exclusion limit on the axion-photon coupling of $g_{a\gamma\gamma} < 0.766 \times 10^{-13}$ GeV^{-1} at the 90% confidence level, for an axion mass of $m_a \simeq 43$ μeV. This was possible by measuring the power spectrum of an oxygen-free high conductivity copper resonant cavity with resonance frequency of about 10.4 GHz, put inside an 8.1 T magnetic field. The cavity was cooled down to a temperature of 200 mK, and the total noise of the system resulted in 1 K, including the 0.5 K from the JPA. The data were analyzed with a simple maximum likelihood procedure. The obtained result shows that QUAX has become competitive among other haloscope experiments in the galactic axion search.

In the immediate future QUAX will double its search potential with the new LNF haloscope. Chapter 4 is dedicated to the setup of all its pieces. We can rely on a new dry cryostat with a base temperature of $T \simeq 10$ mK, and we are currently testing a new magnet providing up to 9 T magnetic field. Moreover, a 246 mm-long copper resonant cavity at 8.5 GHz has been fabricated, showing a quality factor of about 13 000 at room temperature, with which the first data acquisition with the new haloscope will be performed.

Relatively to the SIMP project, we have taken the first steps towards the realization of a CBJJ-based single photon detector. In Chap. 5 we familiarized with the simulation framework to be able to predict how many photons are needed to make a Josephson junction to switch to its finite-voltage state. Thus, the simulations allow us to extract the right fabrication parameters to refine the detector design and choose a proper bias. Then, the first step in the characterization of a JJ detector was fabricating and testing a single junction. Thanks to escape measurements and comparing them with simulations, we were able to extrapolate from the escape rate data a point where the dark count is low ($\sim$1 mHz) and the bias is $I_b/I_c = 0.65$ (Fig. 5.15), which determines a good working point for a photon detector.

In Chapter 6 the next step was taken, the fabrication and testing of the simplest design of a photon detector based on JJs: a transmission line terminated with a single Josephson junction. The JJ was effectively operated as a photon detector, since its activation has been measured as a consequence of the irradiation with microwaves. Unfortunately, the thermal noise in the system was estimated to be as high as 180 mK, so that quantum escape could not be seen alone. Moreover, the high coupling to the transmission line inhibits the junction to switch with very few photons. However, a result expected from simulations was complied: the JJ switches when the number of incoming photons within a relaxation time τ approximately matches the number of levels in its potential well. Depending on the bias and the stimulus conditions, the sensitivity is at the level of few tens of photons.

7.2 Outlook

The goal of the QUAX collaboration by 2025 is to operate a scanning experiment with the two complementary haloscopes at LNL and LNF, although with different technologies and different frequency ranges. While the LNL apparatus is going to use resonant cavities made of movable dielectric cylinders [136], the LNF haloscope will exploit a multicavity scheme, as sketched in Fig. 7.1. In the Figure four cavities are represented, but up to seven are foreseen

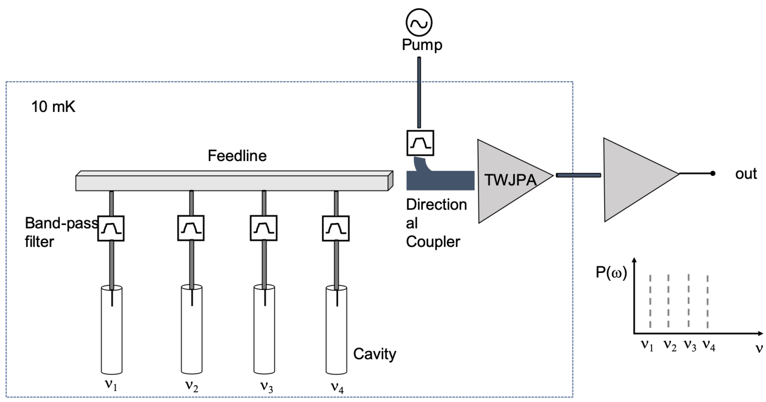

Figure 7.1: Sketch of the multicavity readout scheme foreseen in the LNF apparatus for the QUAX experiment. A traveling-wave Josephson parametric amplifier is represented as the preamplification stage.

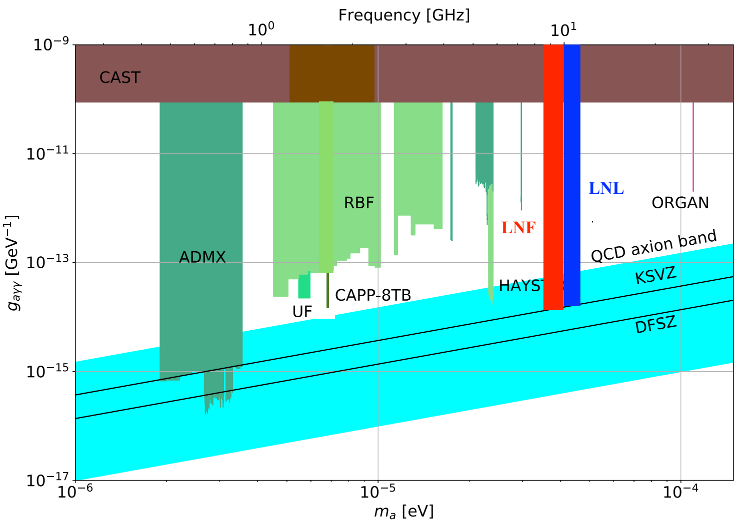

Figure 7.2: Expected physics reach for the QUAX-aγ with the LNF and LNL axion haloscopes by 2025.

in the final setup. These will be hybrid superconducting cavities to improve the quality factor, and the readout will be done at seven different frequencies simultaneously.

This requires a preamplification stage with a large bandwidth, at the level of few GigaHertz, obtainable with traveling-wave Josephson parametric amplifiers (TWJPAs). We already performed a preliminary test of a TWJPA fabricated by INRiM (Istituto Nazionale di Ricerca Metrologica), based on a coplanar waveguide composed of a long array of rf-SQUIDs [137].

The expected physics reach for the QUAX experiment by 2025 is reported in Fig. 7.2: the covered frequency range is from about 8.5 GHz to 11 GHz, corresponding to the axion mass window 34 μeV $-$ 44 μeV, with an expected sensitivity to the KSVZ line. The LNF apparatus will cover the region 8.5 GHz $-$ 10 GHz, while the LNL haloscope from 9.5 to 11 GHz. The optimization of the magnetic field together with the quantum-limited readout and superconductive cavities will allow the LNF haloscope to perform an axion search with a scan speed up to about 18 MHz per day.

Finally, to push the haloscope sensitivity down to the DFSZ axion model line, we need to go beyond quantum-limited devices in favor of a single-photon technology. As mentioned in Sec. 6.5, our next step in the immediate future is testing the performances of the first prototype of a stub tuner.

APPENDIX A

QUAX-$a\gamma$ analysis fit function

Here, a derivation of equation (3.13) is given using the transmission-line formalism. Consider the thermal power $P_1 = k_B T_1 \delta\nu$ reflected by a resonant cavity with frequency $\omega_0/2\pi$ and unloaded quality factor Q_0 at a temperature $T_c \neq T_1$. The total power at the input of an amplifier will be the sum of the reflected power and the power P_{out} emitted by the cavity itself. Considering a total power per unit bandwidth, this will be

$$P_{\text{out}}(\omega) = k_B T_1 |S_{11}(\omega)|^2 + P_{\text{out}}/\delta\nu\,, \tag{A.1}$$

where $S_{11}(\omega)$ is the reflection coefficient from the cavity. The expressions for $S_{11}(\omega)$ and P_{out} can be obtained considering the equivalent circuit of Fig. A.1, where the cavity is coupled to a transmission line of impedance Z_0 through a single port schematized as a transformer. The cavity is a parallel RLC circuit, where R is a noisy resistor at a temperature T_c described by a noise generator I_n in parallel to the resistor. The rms current is $I_{rms}^2 = 4k_B T_c \delta\nu/R$ from the Johnson-Nyquist theorem (see also Eq. (4.1)). The cavity impedance seen from the output

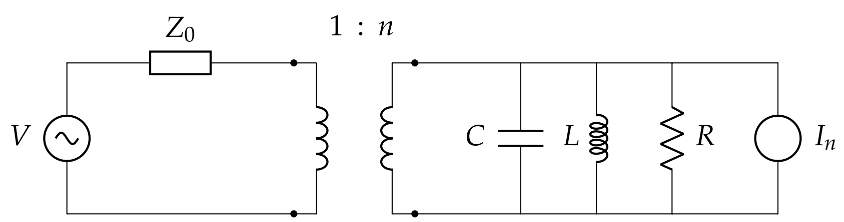

Figure A.1: Equivalent circuit of a resonant cavity, represented as a parallel RLC resonator, coupled to a transmission line where thermal noise is added.

port is $Z_1 = Z_{\text{cav}}/n^2$, while the output line impedance seen from the cavity is $Z_1' = Z_0 n^2$, where n is the winding ratio of the transformer, and the cavity impedance is

$$Z_{\text{cav}} = \frac{R}{1 + jQ_0\delta}, \tag{A.2}$$

with $\delta = \omega/\omega_0 - \omega_0/\omega$, $Q_0 = R/Z_c$ and $Z_c = \sqrt{L/C}$. If a voltage V_c is applied to the cavity, the power dissipated in the cavity is due to its resistance, thus being $P_c = |V_c|^2/(2R)$, while the power delivered to the transmission line is $P_{\text{out}} = |V_c|^2/(2Z_1')$. These are also useful to define a coupling coefficient as $k = P_{\text{out}}/P_c = R/Z_1' = R/(Z_0 n^2)$.

Now the reflection coefficient can be calculated thanks to all the definitions given above:

$$S_{11} \equiv \frac{Z_1 - Z_0}{Z_1 + Z_0} = \frac{Z_{\text{cav}}/n^2 - Z_0}{Z_{\text{cav}}/n^2 + Z_0} = \frac{kZ_0/(1 + jQ_0\delta) - Z_0}{kZ_0/(1 + jQ_0\delta) + Z_0} = \frac{k - 1 - jQ_0\delta}{k + 1 + jQ_0\delta}. \tag{A.3}$$

To compute the power P_{out} transmitted to the output port, suppose that the voltage V_c is given by the resistor's noise current generator, $V_c = Z_{\text{tot}} I_n$. The impedance has to be the parallel between the cavity impedance and the transmission line impedance seen from the cavity, so that:

$$\begin{aligned}
V_c = Z_{\text{tot}} I_n &= I_n \frac{1}{1/Z_1' + 1/R + j\omega C + 1/j\omega L} \\
&= I_n \frac{RZ_1'/(R + Z_1')}{1 + j[RZ_1'/(R + Z_1')]Z_c\delta} \\
&= I_n R \frac{1/(1+k)}{1 + jQ_0\delta/(1+k)} = I_n R \frac{1}{k + 1 + jQ_0\delta},
\end{aligned} \tag{A.4}$$

where in the second line the use of the definition $\omega_0 = 1/\sqrt{LC}$ has been made. With the definition of P_{out}, we have:

$$P_{\text{out}} = \frac{|V_c|^2}{2Z_1'} = \frac{1}{2Z_1'} I_n^2 R^2 \frac{1}{(k+1)^2 + (Q_0\delta)^2} = I_{rms}^2 R \frac{k}{(k+1)^2 + (Q_0\delta)^2}. \tag{A.5}$$

Here, the $1/2$ factor has been absorbed by the definition of the rms current, $I_{rms}^2 = (1/2) I_n^2$. Substituting I_{rms} in the equation finally gives

$$P_{\text{out}} = 4k_B T_c \delta\nu \frac{k}{(k+1)^2 + (Q_0\delta)^2}. \tag{A.6}$$

Inserting the expressions of $S_{11}(\omega)$ and P_{out} in equation (A.1) and defining the loaded quality factor as $Q_L = Q_0/(1+k)$, the total output power per unit bandwidth is

$$P_{\text{out}}(\omega) = k_B T_1 \frac{(k-1)^2 + (Q_0\delta)^2}{(k+1)^2 + (Q_0\delta)^2} + 4k_B T_c \frac{k}{(k+1)^2 + (Q_0\delta)^2}. \tag{A.7}$$

With some algebra, this expression can be changed into the following:

$$P_{\text{out}}(\omega) = k_B T_1 \frac{[(k-1)^2 + 4kT_c/T_1]/(k+1)^2 + (Q_L\delta)^2}{1+(Q_L\delta)^2}\,, \tag{A.8}$$

where the loaded quality factor appears instead of Q_0. Finally, assuming the coupling is $k=1$, the equation becomes

$$P_{\text{out}}(\omega) = k_B T_1 \frac{T_c/T_1 + (Q_L\delta)^2}{1+(Q_L\delta)^2}\,, \tag{A.9}$$

that at resonance gives $P_{\text{out}}(\omega_0) = k_B T_c$.

$P_{\text{out}}(\omega)$ is the expression of the power at the input of the amplification chain. The power measured at the output of the amplifiers must account for the noise added by the amplification chain. If the two amplifiers have noise temperatures T_{A1} and T_{A2}, then the noise power is

$$P_n = G_1 \times G_2(\omega)\,(P_{\text{out}}(\omega) + k_B T_{A1} + k_B T_{A2}/G_1)\,, \tag{A.10}$$

where T_{A2}/G_1 is the noise temperature of the second amplifier referred to the input of the first. In our setup, the preamplification stage is a JPA with gain $G_1 \sim 18$ dB assumed to be constant in the 2 MHz acquisition window, and $G_2(\omega)$ is the gain of the remaining amplification chain. If we consider the attenuation of the cables from the JPA to the HEMT, of about 3 dB, the net gain G_1 becomes ~ 15 dB. As in Table 3.1, the noise temperature of the JPA is $T_{A1} = 0.25$ K at 10 GHz (vacuum fluctuations will be included later), and from the HEMT we have $T_{A2} \sim 8$ K; therefore, the total noise temperature added by the amplifiers is

$$T_{A,tot} = T_{A1} + T_{A2}/G_1 = 0.25 + 8/10^{1.5} = 0.50\,\text{K}\,. \tag{A.11}$$

Inserting $T_{A,tot}$ in Eq. (A.10) gives

$$P_n = G_{\text{TOT}}(\omega) k_B T_1 \left(\frac{T_c/T_1 + (Q_L\delta)^2}{1+(Q_L\delta)^2} + \frac{T_{A,tot}}{T_1} \right)\,, \tag{A.12}$$

and written as the fit function in Sec. 3.2, it becomes

$$P_n = G_{\text{TOT}}(\omega) k_B\,(T_1 + T_{A,tot}) \left(\frac{T_1}{T_{A,tot}+T_1} \frac{T_c/T_1 + (Q_L\delta)^2}{1+(Q_L\delta)^2} + \frac{T_{A,tot}}{T_{A,tot}+T_1} \right)\,. \tag{A.13}$$

Actually, at low temperatures such that $k_B T \ll h\nu_c$, the Bose-Einstein statistics has to be taken into account. Thus, instead of the approximated expression $k_B T\delta\nu$, a noise power has to be written as

$$P = \left(\frac{h\nu}{e^{h\nu/k_B T} - 1} + \frac{h\nu}{2} \right) \delta\nu\,, \tag{A.14}$$

which includes also the contribution from vacuum fluctuations. Consequently, temperatures are modified as follows:

$$\tilde{T} = \frac{h\nu}{k_B}\left(\frac{1}{e^{h\nu/k_B T}-1} + \frac{1}{2}\right) . \tag{A.15}$$

Thus, in place of the temperatures T_1 and T_c, the effective temperatures $\tilde{T}_1$ and $\tilde{T}_c$ have to be used. Modifying Eq. (A.13) finally leads to the fit function (3.13):

$$P_n = G_{\text{TOT}}(\omega) k_B \left(\tilde{T}_1 + T_{A,tot}\right)\left(\frac{\tilde{T}_1}{T_{A,tot}+\tilde{T}_1}\frac{\tilde{T}_c/\tilde{T}_1 + (Q_L\delta)^2}{1+(Q_L\delta)^2} + \frac{T_{A,tot}}{T_{A,tot}+\tilde{T}_1}\right) . \tag{A.16}$$

It can be seen that when $T_{A,tot}$ is summed to $\tilde{T}_1$, the vacuum fluctuation term $h\nu/(2k_B) = 0.25$ K for a 10 GHz frequency is included to give the right amount of noise.

APPENDIX B

Motivation of the expressions for single-photon currents

Derivation of the factor 2 in the equation for the flux variable ϕ.

The equation of motion for the flux variable $\phi = \varphi(\phi_0/2\pi)$ in a TL terminated by a linearized JJ (5.18) has been written as

$$C_J\ddot{\phi} + \frac{\phi}{L_J} + \frac{1}{Z_{TL}}\dot{\phi} = 2\frac{1}{Z_{TL}}\dot{\phi}^{in} = 2I^{in}, \tag{B.1}$$

where I^{in} is an input current. The factor 2 can be derived from transmission line theory [108].

The equation of motion of the JJ in the RCSJ model is

$$C\ddot{\phi} + \frac{\dot{\phi}}{R} + I_c \sin 2\pi\phi/\phi_0 = I(0), \tag{B.2}$$

where $I(0)$ is the current in $x = 0$ at the end of the transmission line, where the JJ lies. $I(0)$ can be expressed in terms of the input current $I^+(0)$ and the total voltage on the TL $V(0)$, at $x = 0$, as the following:

$$\begin{aligned} V(0) &= V^+(0) + V^-(0)\,, \\ I(0) &= I^+(0) + I^-(0) = \left(V^+(0) - V^-(0)\right)/Z_{TL}\,, \end{aligned} \tag{B.3}$$

from which

$$I(0) = I^+(0) - \frac{1}{Z_{TL}}\left(V(0) - V^+(0)\right) = 2I^+(0) - \frac{V(0)}{Z_{TL}}\,. \tag{B.4}$$

Using the first Josephson relation, the total voltage can be written as $V(0) = \dot{\phi}$, then

$$I(0) = 2I^+(0) - \frac{\dot{\phi}}{Z_{TL}} . \tag{B.5}$$

Substituting in equation (B.2), this gives

$$C\ddot{\phi} + \left(\frac{1}{R} + \frac{1}{Z_{TL}} \right) \dot{\phi} + I_c \sin 2\pi\phi/\phi_0 = 2I^+(0), \tag{B.6}$$

and since in our case $Z_{TL} \ll R_J$, the JJ resistance in the parentheses can be neglected.

Derivation of the single-photon peak current.

The single-photon peak current (5.19) has been written as

$$I^2_{\text{peak}} = \frac{\hbar\omega_J}{Z_{TL}} \frac{2}{\sqrt{2\pi}\sigma_t} . \tag{B.7}$$

This can be understood by simple energetic arguments. The energy of a photon contained in a length Δx of the TL is

$$\hbar\omega_0 = \frac{1}{2} L_l I^2_{\text{peak}} \Delta x \, , \tag{B.8}$$

where L_l is the TL inductance per unit length, so that the right hand side of the equation is the energy deposited in an inductive lumped element of length Δx. For a photon with time duration $\sqrt{2\pi}\sigma_t$ (which is the length of a step function with equal area and height of a Gaussian with standard deviation σ_t), we can write

$$\Delta x = v_{\text{ph}} \sqrt{2\pi}\sigma_t \, , \tag{B.9}$$

v_{ph} being its phase velocity. It follows that

$$I^2_{\text{peak}} = \frac{2\hbar\omega_0}{L_l v_{\text{ph}} \sqrt{2\pi}\sigma_t} = \frac{\hbar\omega_0}{Z_0} \frac{2}{\sqrt{2\pi}\sigma_t} \, , \tag{B.10}$$

where in the second equality we have used the definition of the phase velocity for a propagating wave on a TL in terms of the inductance and capacity, $v_{\text{ph}} = 1/\sqrt{L_l C_l}$, and the definition of the TL impedance $Z_{TL} = \sqrt{L/C}$.

APPENDIX C

Rf lines calibration details

The diagram of the dedicated run exploited to perform calibration measurements is reported in Fig. 6.5. To fix the notation, we call the total S_{21} parameters by Mij, with i the line connected to the drive port of the VNA and j the line connected to the readout port. So for example $M12$ is the measured S_{21} entering from line 1 and coming out from port 2. The single line attenuations/gains are called $L1$, $L2$, $L3$ and $L5$, again measured as S_{21} parameters. The relations of all the possible combinations are

$$\begin{aligned}
M25 &= L2 + A + L5 \\
M15 &= L1 + A + L5 \\
M35 &= L3 + B + L5 \\
M13 &= L1 + A + L3 \\
M23 &= L2 + A + L3 \\
M12 &= L1 + B + L2\,,
\end{aligned} \tag{C.1}$$

where A is the direct coupling of the directional coupler and B refers to its "coupled" port. A and B must obey a unitarity relation; by specifications $B = -10$ dB, and then $A = -0.45$ dB. The system (C.1) contains 6 equations and 6 variables, but since A and B are not independent, this becomes a system with 5 linearly independent equations and 5 variables. Therefore, to solve the system, we assume $A = -0.45$ dB as known (and will verify the condition later by inspecting B). The equations are then solved by the following relations:

$$\begin{aligned}
A &= -0.45 \\
B &= 0.5\,(M12 + M35 - M25 - M13 + 2A) \\
L5 &= 0.25\,(3\,M25 + M35 - M12 + M13 - 2\,M23 - 2A) \\
L2 &= M25 - A - L5 \\
L1 &= M15 - A - L5 \\
L3 &= M13 - L1 - A\,.
\end{aligned} \tag{C.2}$$

Here, we consider the insertion loss of the switch to be known, and is already included in the definition of the lines $L1$ to $L5$.

Bibliography

[1] A. Rettaroli et al., Instruments **5** (2021) (cit. on pp. iv, 76).

[2] D. Alesini et al., Phys. Rev. D **103**, 102004 (2021) (cit. on pp. iv, 42, 47).

[3] C. Guarcello et al., Phys. Rev. Applied **16**, 054015 (2021) (cit. on p. iv).

[4] N. Aghanim et al., Astron. Astrophys. **641** (2020) (cit. on pp. 1, 18, 46).

[5] I. Irastorza and J. Redondo, Progress in Particle and Nuclear Physics **102**, 89–159 (2018) (cit. on pp. 2, 13, 14, 16–19, 21, 23, 24).

[6] C. A. Baker et al., Phys. Rev. Lett. **97**, 131801 (2006) (cit. on p. 2).

[7] J. M. Pendlebury et al., Phys. Rev. D **92**, 092003 (2015) (cit. on pp. 2, 8).

[8] R. D. Peccei and H. R. Quinn, Phys. Rev. Lett. **38**, 1440–1443 (1977) (cit. on pp. 2, 9).

[9] R. D. Peccei and H. R. Quinn, Phys. Rev. D **16**, 1791–1797 (1977) (cit. on pp. 2, 9).

[10] S. Weinberg, Phys. Rev. Lett. **40**, 223–226 (1978) (cit. on pp. 2, 9).

[11] F. Wilczek, Phys. Rev. Lett. **40**, 279–282 (1978) (cit. on pp. 2, 9).

[12] P. Sikivie, Phys. Rev. Lett. **51**, 1415–1417 (1983) (cit. on pp. 2, 22, 23, 54).

[13] S. Gleyzes et al., Nature **446**, 297–300 (2007) (cit. on p. 3).

[14] D. I. Schuster et al., Nature **445**, 515–518 (2007) (cit. on p. 3).

[15] B. Johnson et al., Nature Phys. **6**, 663–667 (2010) (cit. on p. 3).

[16] J.-C. Besse et al., Phys. Rev. X **8**, 021003 (2018) (cit. on p. 3).

[17] S. Kono et al., Nature Phys. **14**, 546–549 (2018) (cit. on p. 3).

[18] R. Lescanne et al., Phys. Rev. X **10**, 021038 (2020) (cit. on pp. 3, 83).

[19] K. Inomata et al., Nat. Commun. **7** (2016) (cit. on p. 3).

[20]Y.-F. Chen et al., Phys. Rev. Lett. **107**, 217401 (2011) (cit. on p. 3).

[21]L. S. Kuzmin et al., IEEE Trans. Appl. Supercond. **28**, 1–5 (2018) (cit. on pp. 3, 75, 76).

[22]A. D. Semenov, G. N. Gol'tsman, and R. Sobolewski, Supercond. Sci. Technol. **15** (2002) (cit. on p. 3).

[23]F. Paolucci et al., J. Appl. Phys. **128**, 194502 (2020) (cit. on p. 3).

[24]S. Komiyama, IEEE Journal of Selected Topics in Quantum Electronics **17**, 54–66 (2011) (cit. on p. 3).

[25]A. V. Dixit et al., Phys. Rev. Lett. **126**, 141302 (2021) (cit. on p. 3).

[26]P. A. Zyla et al., Prog. Theor. Exp. Phys. **2020** (2020) (cit. on pp. 5, 15, 16, 54).

[27]P. Collins, A. Martin, and E. Squires, *Particle physics and cosmology* (Wiley, 1989) (cit. on pp. 5, 6, 8).

[28]M. Srednicki, *Quantum field theory* (Cambridge University Press, 2007) (cit. on pp. 5, 6).

[29]F. Mandl and G. Shaw, *Quantum field theory* (Wiley, 2010) (cit. on p. 6).

[30]S. Weinberg, Phys. Rev. D **11**, 3583–3593 (1975) (cit. on p. 6).

[31]R. D. Peccei, J. Korean Phys. Soc. **29**, arXiv:hep-ph/9606475v1 (1996) (cit. on pp. 6–10).

[32]R. D. Peccei, Axions. Lecture Notes in Physics **741**, 3–17 (2008) (cit. on p. 6).

[33]G. 't Hooft, Phys. Rev. Lett. **37**, 8–11 (1976) (cit. on p. 7).

[34]G. 't Hooft, Phys. Rev. D **14**, 3432–3450 (1976) (cit. on p. 7).

[35]M. Pospelov and A. Ritz, Nucl. Phys. B **573**, 177–200 (2000) (cit. on p. 8).

[36]D. Budker et al., Phys. Rev. X **4**, 021030 (2014) (cit. on p. 10).

[37]W. A. Bardeen, R. D. Peccei, and T. Yanagida, Nucl. Phys. B **279**, 401–428 (1987) (cit. on p. 11).

[38]Y. Asano et al., Phys. Lett. B **107**, 159–162 (1981) (cit. on p. 11).

[39]J. E. Kim, Phys. Rev. Lett. **43**, 103–107 (1979) (cit. on p. 11).

[40]M. A. Shifman, A. I. Vainshtein, and V. I. Zakharov, Nucl. Phys. B **166**, 493–506 (1980) (cit. on p. 11).

[41]A. R. Zhitnitsky, Sov. J. Nucl. Phys. **31**, 260 (1980) (cit. on p. 11).

[42]M. Dine, W. Fischler, and M. Srednicki, Phys. Lett. B **104**, 199–202 (1981) (cit. on p. 11).

[43]B. M. Brubaker, *First results from the haystac axion search*, PhD thesis, arXiv:1801.00835v1 (Yale University, 2018) (cit. on pp. 12, 46).

[44]H. Primakoff, Phys. Rev. **81**, 899–899 (1951) (cit. on p. 12).

[45]M. Srednicki, Nucl. Phys. B **260**, 689–700 (1985) (cit. on p. 13).

[46]C. O'Hare, *Cajohare/axionlimits: axionlimits*, version v1.0, July 2020 (cit. on pp. 14, 21).

[47]G. G. Raffelt, Axions. Lecture Notes in Physics **741** (2008) (cit. on p. 15).

[48]L. Di Luzio, F. Mescia, and E. Nardi, Phys. Rev. Lett. **118**, 031801 (2017) (cit. on p. 15).

[49]J. Jaeckel and A. Ringwald, Annual Review of Nuclear and Particle Science **60**, 405–437 (2010) (cit. on pp. 16, 22).

[50]P. Sikivie, "Axions", in *Particle dark matter: observations, models and searches*, edited by G. Bertone (Cambridge University Press, Cambridge, England, 2010) (cit. on pp. 17, 18).

[51]D. J. E. Marsh, Physics Reports **643**, 1–79 (2016) (cit. on pp. 18, 19).

[52]J. I. Read, J. Phys. G: Nucl. Part. Phys. **41**, 063101 (2014) (cit. on p. 19).

[53]B. M. Brubaker et al., Phys. Rev. D **96**, 123008 (2017) (cit. on pp. 19, 57).

[54]M. S. Turner, Phys. Rev. D **42**, 3572–3575 (1990) (cit. on pp. 19, 20, 52, 54).

[55]K. Ehret et al., Phys. Lett. B **689**, 149–155 (2010) (cit. on p. 22).

[56]P. Pugnat et al., Phys. Rev. D **78**, 092003 (2008) (cit. on p. 22).

[57]M. Diaz Ortiz et al., *Design of the alps ii optical system*, arXiv:2009.14294, 2021 (cit. on p. 22).

[58]P. Sikivie, Phys. Rev. D **32**, 2988–2991 (1985) (cit. on pp. 22, 23, 46, 54).

[59]L. Krauss et al., Phys. Rev. Lett. **55**, 1797–1800 (1985) (cit. on p. 22).

[60]N. Du et al., Phys. Rev. Lett. **120**, 151301 (2018) (cit. on pp. 23, 57).

[61]T. Braine et al., Phys. Rev. Lett. **124**, 101303 (2020) (cit. on p. 23).

[62]K. M. Backes et al., Nature **590**, 238 (2021) (cit. on p. 23).

[63]A. Á. Melcón et al., J. Cosmol. Astropart. P. **2018**, 040–040 (2018) (cit. on p. 23).

[64]J. L. Ouellet et al., Phys. Rev. D **99**, 052012 (2019) (cit. on pp. 23, 57).

[65]B. T. McAllister et al., Phys. Dark Universe **18**, 67–72 (2017) (cit. on p. 23).

[66]J. Choi et al., Nucl. Instrum. Methods Phys. Res. A **1013**, 165667 (2021) (cit. on p. 23).

[67]J. Jeong et al., Phys. Rev. Lett. **125**, 221302 (2020) (cit. on p. 23).

[68]*BRASS: Broadband Radiometric Axion SearcheS*, `https://www.physik.uni-hamburg.de/en/iexp/gruppe-horns/forschung/brass.html` (cit. on p. 23).

[69]A. Caldwell et al., Phys. Rev. Lett. **118**, 091801 (2017) (cit. on p. 23).

[70]P. Brun et al., Eur. Phys. J. C **79** (2019) `10.1140/epjc/s10052-019-6683-x` (cit. on p. 23).

[71]V. Anastassopoulos et al., Nature Phys. **13**, 584–590 (2017) (cit. on p. 24).

[72]E. Armengaud et al., Journal of Instrumentation **9**, T05002–T05002 (2014) (cit. on p. 24).

[73]A. Abeln et al., J. High Energ. Phys. **2021** (2021) (cit. on p. 24).

[74]B. D. Josephson, Phys. Lett. **1**, 251–253 (1962) (cit. on p. 25).

[75]B. D. Josephson, Adv. Phys. **14**, 419–451 (1965) (cit. on p. 25).

[76]R. P. Feynman, *Lectures on physics*, Vol. 3 (Addison-Wesley, 1965) (cit. on p. 25).

[77]V. Ambegaokar and A. Baratoff, Phys. Rev. Lett. **10**, 486–489 (1963) (cit. on p. 26).

[78]C. P. J. Poole et al., *Superconductivity*, Third ed. (Elsevier Inc., 2014) (cit. on pp. 27, 30, 32).

[79]M. Tinkham, *Introduction to superconductivity*, Second ed. (McGraw-Hill, Inc., 1996) (cit. on pp. 31, 34).

[80]S. Schmidlin, *Physics and technology of small josephson junctions*, PhD thesis (Royal Holloway, University of London, 2013) (cit. on p. 31).

[81]L. Longobardi et al., Phys. Rev. Lett. **109**, 050601 (2012) (cit. on pp. 33, 36, 83).

[82]H. A. Kramers, Physica **7**, 284–304 (1940) (cit. on p. 34).

[83]M. Büttiker, E. P. Harris, and R. Landauer, Phys. Rev. B **28**, 1268–1275 (1983) (cit. on p. 34).

[84]T. A. Fulton and L. N. Dunkleberger, Phys. Rev. B **9**, 4760–4768 (1974) (cit. on pp. 34, 36).

[85]A. O. Caldeira and A. J. Leggett, Ann. Phys. **149**, 374–456 (1983) (cit. on p. 35).

[86]D. Massarotti et al., Low Temperature Physics **38**, 263–272 (2012) (cit. on pp. 35, 83).

[87]J. M. Martinis, M. H. Devoret, and J. Clarke, Phys. Rev. Lett. **55**, 1543–1546 (1985) (cit. on pp. 35, 77, 83, 84).

[88]J. M. Kivioja et al., Phys. Rev. Lett. **94**, 247002 (2005) (cit. on pp. 36, 83, 84).

[89]J. C. Fenton and P. A. Warburton, Phys. Rev. B **78**, 054526 (2008) (cit. on pp. 37, 83, 84).

[90]A. Roy and M. Devoret, Phys. Rev. B **98**, 045405 (2018) (cit. on p. 39).

[91]R. Barbieri et al., Physics Letters B **226**, 357–360 (1989) (cit. on p. 42).

[92]R. Barbieri et al., Phys. Dark Universe **15**, 135–141 (2017) (cit. on pp. 42, 44).

[93]C. Kittel, *Introduction to solid state physics*, 8th edition (Wiley, 2004) (cit. on p. 44).

[94]F. Bloch, Phys. Rev. **70**, 460–474 (1946) (cit. on p. 44).

[95]N. Bloembergen and R. V. Pound, Phys. Rev. **95**, 8–12 (1954) (cit. on p. 44).

[96]S. Bloom, J. of Appl. Phys. **28**, 800–805 (1957) (cit. on p. 44).

[97]N. Crescini, *Towards the development of the ferromagnetic axion haloscope*, PhD thesis (University of Padua, 2019) (cit. on p. 44).

[98]N. Crescini et al., Eur. Phys. J. C **78** (2018) (cit. on pp. 44, 45).

[99]N. Crescini et al., Phys. Rev. Lett. **124**, 171801 (2020) (cit. on pp. 44, 45).

[100]G. Flower et al., Phys. Dark Universe **25**, 100306 (2019) (cit. on p. 45).

[101] *ANSYS HFSS software*, `https://www.ansys.com/products/electronics/ansys-hfss` (cit. on pp. 47, 72).

[102] N. Roch et al., Phys. Rev. Lett. **108**, 147701 (2012) (cit. on p. 49).

[103] R. H. Dicke, Rev. Sci. Instrum. **17**, 268–275 (1946) (cit. on pp. 54, 59, 75).

[104] G. Cowan et al., *Power-constrained limits*, arXiv:1105.3166v1, 2011 (cit. on p. 56).

[105] J. W. Foster, N. L. Rodd, and B. R. Safdi, Phys. Rev. D **97**, 123006 (2018) (cit. on p. 57).

[106] J. B. Johnson, Phys. Rev. **32**, 97–109 (1928) (cit. on p. 58).

[107] H. Nyquist, Phys. Rev. **32**, 110–113 (1928) (cit. on p. 58).

[108] D. M. Pozar, *Microwave engineering* (Wiley, 2012) (cit. on pp. 59, 69, 126, 135).

[109] C. E. Shannon, Proceedings of the IRE **37**, 10–21 (1949) (cit. on p. 60).

[110] H. A. Haus and J. A. Mullen, Phys. Rev. **128**, 2407–2413 (1962) (cit. on pp. 61, 75).

[111] C. M. Caves, Phys. Rev. D **26**, 1817–1839 (1982) (cit. on pp. 61, 75).

[112] G. Ventura and L. Risegari, *The art of cryogenics* (Elsevier, 2008) (cit. on pp. 62–64).

[113] G. K. White and P. J. Meeson, *Experimental techniques in low-temperature physics*, 4th edition (Oxford University Press, 2002) (cit. on p. 62).

[114] O. V. Lounasmaa, *Experimental principles and methods below 1 k* (Academic Press: London and New York, 1974) (cit. on p. 63).

[115] F. Pobell, *Matter and methods at low temperatures*, Third edition (Springer, 2007) (cit. on p. 67).

[116] D. Di Gioacchino et al., IEEE Trans. Appl. Supercon. **29**, 1–5 (2019) (cit. on p. 74).

[117] D. Alesini et al., Phys. Rev. D **99**, 101101 (2019) (cit. on p. 74).

[118] S. K. Lamoreaux et al., Phys. Rev. D **88**, 035020 (2013) (cit. on p. 75).

[119] D. Alesini et al., J. Low Temp. Phys. **199**, 348–354 (2020) (cit. on p. 76).

[120] A. Barone and G. Paternò, *Physics and applications of the josephson effect* (Wiley, 1982) (cit. on pp. 76, 87, 103).

[121] S. Kogan, *Electronic noise and fluctuations in solids* (Cambridge University Press, 1996) (cit. on p. 77).

[122] M. Schöndorf et al., Quantum Science and Technology **3**, 024009 (2018) (cit. on pp. 77, 83).

[123] M. H. Devoret, J. M. Martinis, and J. Clarke, Phys. Rev. Lett. **55**, 1908–1911 (1985) (cit. on p. 77).

[124] A. Piedjou Komnang et al., Chaos, Solitons & Fractals, 110496 (2020) (cit. on p. 77).

[125] E. Ben-Jacob and D. J. Bergman, Phys. Rev. A **29**, 2021–2028 (1984) (cit. on p. 79).

[126]B. Yurke and J. S. Denker, Phys. Rev. A **29**, 1419–1437 (1984) (cit. on p. 80).

[127]J. M. Kivioja et al., New J. Phys. **7**, 179–179 (2005) (cit. on pp. 83, 84, 88).

[128]M.-H. Bae et al., Phys. Rev. B **79**, 104509 (2009) (cit. on pp. 83, 84).

[129]H. F. Yu et al., Phys. Rev. Lett. **107**, 067004 (2011) (cit. on pp. 83, 84).

[130]M. G. Castellano et al., Journal of Applied Physics **86**, 6405–6411 (1999) (cit. on pp. 83, 84).

[131]Y. Yoon et al., J. Low Temp. Phys. **163**, 164–169 (2011) (cit. on pp. 83, 84).

[132]J. M. Martinis, M. H. Devoret, and J. Clarke, Phys. Rev. B **35**, 4682–4698 (1987) (cit. on p. 89).

[133]M. H. Devoret et al., Phys. Rev. Lett. **53**, 1260–1263 (1984) (cit. on p. 114).

[134]F. Paolucci et al., Journal of Applied Physics **128**, 194502 (2020) (cit. on p. 126).

[135]J. Govenius et al., Phys. Rev. Lett. **117**, 030802 (2016) (cit. on p. 126).

[136]D. Alesini et al., Nucl. Instrum. Methods Phys. Res. A **985**, 164641 (2021) (cit. on p. 129).

[137]L. Fasolo et al., *Bimodal approach for noise figures of merit evaluation in quantum-limited josephson traveling wave parametric amplifiers*, arXiv:2109.14924, 2021 (cit. on p. 130).